High-frequency acousto-optics in semiconductor and metal nanostructures

Dissertation

presented to the Faculty of Physics of the
TU Dortmund University, Germany,
in partial fulfillment of the requirements
for the degree of

Doktor rer. nat.

by
Christian Brüggemann

technische universität
dortmund

Dortmund, April 2013

Accepted by the Faculty of Physics of the TU Dortmund University, Germany

Day of the oral examination: 29th May 2013

Examination board:
Prof. Dr. Manfred Bayer
Prof. Dr. Metin Tolan
Prof. Dr. Frithjof Anders
Dr. Alex Greilich

Contents

Part I

Introduction

Modern telecommunication has been influenced to a large extend by the innovation of optical data transmission. The pioneering work in the development of fibre optics by *Charles K. Kao* was one of the milestones, ensueing in the award of the 2009 Nobel Prize in Physics [1]. Opto-electronic devices provide the link between electronic circuits and optical fibres. They are usually based on vertical-cavity-surface-emitting-lasers (VCSEL) and nowadays operate at 10 GB/s [2]. However, the increasing demand of broadband internet services and cloud computing applications requires a transition to 100 GB/s [3]. The intermediate approach is to combine several VCSELs, each operating at a different wavelength [4]. A long-term approach, though, is targeting for single high-speed lasers, which demands lower lasing thresholds to reduce the current. One way is to follow the idea of *Dingle* and *Henry* [5]: to reduce the dimensionality of the gain medium for lower lasing thresholds. This concept is already applied in VCSELs today, which commonly use quantum wells as the gain medium [1D confinement]. A step further is to use quantum dots [3D confinement], where the singularity in the density of states may dramatically reduce the lasing threshold [2]. A demanding task in this regard is to achieve resonance between the electronic transitions involved in laser operation and the resonator mode. In some cases it may be even impossible by the fabrication process.

Like for telecommunication, optical data transfer may as well be the future for microprocessors. The down-scaling of electronic circuits generates a challenge for intra-chip interconnect technology, because the scaling of electronic interconnects cannot compete with the exponentially growing transistor count [6]. Structure sizes of a few 10 nm in today's circuits result in an undesireable increase in wire resistance, which in turn leads to an increase in the data transmission delay and also increase the cross-talk between individual interconnects.
An implementation of optical communication technology based on fibre optics, however, is unfeasible, due to the diffraction limited size on the order of an optical wavelength [$\lambda \sim 1$ μm]. Surface plasmon polaritons (SPP), bound oscillations of electrons and light at metal-dielectric interfaces, are suggested to overcome the obstacle of the diffraction limit [7]. Pioneered by the demonstration of subwavelength waveguiding [8] and nanofocusing [9] at optical frequencies, a vast effort in research of nanophotonics based on SPPs, termed "plasmonics", was raised. Plasmonics offers the capacity of photonics and the miniaturization of electronics. Numerous concepts for plasmon waveguiding with confinement to less than a tenth of λ, suitable for intra-chip data transmission, have been suggested and partly proved [10].
Among waveguides, there are several other elements necessary to realize plasmonic circuits, such as switches, modulators and couplers. Thus, there is a need for active elements, able to modulate the transmitted field phase and/or amplitude [10].

In this work, it will be demonstrated that coherent phonons are suitable to address some of the remaining tasks in realizing efficient high-speed lasers for opto-electronic devices and "active plasmonics" in order to realize plasmonic circuits. In particular, the hybrid nature of photonic/phononic superstructures will be exploited.
Picosecond acoustics, a technique to generate coherent phonon wavepackages with frequencies in the THz range, will be reviewed in chapter 1 of this part I. In chapter

2, the experimental methods and setups, used to obtain the results presented in this thesis, will be introduced. Part II of this thesis will feature results gathered for the application of coherent phonons to a quantum dot microcavity laser. Up to 200 fold increase of the laser emission intensity due to quantum dot shaking will be demonstrated, as well as harmonic emission modulation at 17 GHz due to phonon filtering in the same device. In Part III, it will be shown that coherent phonons are suitable to modulate a SPP resonance in a gold grating at sub-THz frequencies, exploiting the hybrid photonic/phononic nature of the periodic gold structure. Furthermore, it will be demonstrated that coherent phonons are also useful for probing the electromagnetic far-field inside samples with plasmonic structures built on them, which is challanging using standard optical techniques.
Further details of part II and III will be given in the respective preambles.

1

Picosecond acoustics

Many problems in solid state physics can be approximated to a good degree by assuming that the atomic cores of a crystal lattice are static. One particular example is the calculation of the electronic band structure in crystals. Using the *Born-Oppenheimer* approximation, the dynamics of electrons and the atomic cores are separated due to their different kinetic energies. Also, a periodic potential associated with the atomic cores on a static bravais lattice is assumed [e.g. [11]].

This approximation, however, only applies to a certain extent. Ultimately, *Heisenberg*'s uncertainty relation $\Delta x \Delta p \geq h/2$ results in the fact that the average momentum of the lattice atoms has to be greater than zero, even at a temperature of zero Kelvin. A number of solid state properties can only be explained, if lattice vibrations are taken into account, e.g., thermal expansion, or propagation of sound [12].

Even results, which are approximated to a good degree by a static lattice, might receive perturbative corrections, if the lattice vibrations are strong enough. For example, the first order corrections for the separation of electron and atomic core kinetics is of the order $(m_e/M)^{\frac{1}{4}} \sim 10^{-1} - 10^{-2}$ [m_e: electron mass, M: core mass], which implies that corrections of the electronic bandstructure need to be considered for strong lattice vibrations [11, 13]. This particular example is subject of a more detailed discussion in chapter 4 and following.

Lattice vibrations in the quantum mechanical picture are treated as a bosonic quasiparticle, called "phonon". In the context of this work, ultrashort coherent phonon wavepackages, i.e., picosecond strain pulses, are of particular interest. They will be utilized to perturb the lattice of semiconductor and metal nanostructures in order to manipulate their coupled systems on picosecond timescales.

This chapter is structured as follows. It starts with a review of the phonon concept in section 1.1. In section 1.2, elasticity, the limiting case of long wavelengths, where the lattice-structure can be treated as a continuum, will be discussed. Subsequently, this concept will be used to explain the excitation process of picosecond strain pulses by femtosecond laser pulses in sec. 1.3. The propagation of such pulses and the role of anharmonicity will be covered in section 1.4.

1.1 Phonons

A system of N atoms with mass M on a *Bravais* lattice in d dimensions, which are coupled by an effective potential $U_{eff}(\boldsymbol{R}_1, \dots, \boldsymbol{R}_N)$, is investigated. Their individual location $\boldsymbol{R}_j$ is displaced by $\boldsymbol{u}_i$ from their equilibrium position $\boldsymbol{R}_j^{\boldsymbol{0}}$

$$\boldsymbol{R}_j = (R_{j1}, ...R_{jd}) = \boldsymbol{R}_j^0 + \boldsymbol{u}_j. \tag{1.1}$$

In this case the lattice Hamiltonian H_{lat} has the form [11]

$$H_{lat} = \sum_{j=1}^{N} \frac{\boldsymbol{P}_j^2}{2M} + U_{eff}(\boldsymbol{R}_1, ..., \boldsymbol{R}_N), \tag{1.2}$$

where $\boldsymbol{P}_j$ is the momentum of atom j. If only small displacements $\boldsymbol{u}_j$ are considered, one can write U_{eff} as a *Taylor* expansion

$$U_{eff} = U(\boldsymbol{R^0}) + \sum_{j,\alpha} \left. \frac{\partial U}{\partial R_{j\alpha}} \right|_{\boldsymbol{R^0}} u_{j\alpha} + \frac{1}{2} \sum_{j,k,\alpha,\beta} \left. \frac{\partial U}{\partial^2 R_{j\alpha} \partial R_{k\beta}} \right|_{\boldsymbol{R^0}} u_{j\alpha} u_{k\beta} + \dots \tag{1.3}$$

The sum over j, k runs over all lattice atoms and α, β over all dimensions. The first term in Eq. 1.3 is a constant and resembles the inner energy of the crystal in equilibrium. The second term describes the effective force, which has to be 0 at the equilibrium position $\boldsymbol{R^0}$, so that in lowest order expansion one has to consider only the quadratic term. This is the so-called harmonic approximation with the harmonic potential

$$U_{harm} = \frac{1}{2} \sum_{j,k,\alpha,\beta} \left. \frac{\partial U}{\partial^2 R_{j\alpha} \partial R_{k\beta}} \right|_{\boldsymbol{R^0}} u_{j\alpha} u_{k\beta} = \frac{1}{2} \sum_{j,k,\alpha,\beta} \Phi_{j\alpha k\beta} u_{j\alpha} u_{k\beta}. \tag{1.4}$$

$\Phi_{j\alpha k\beta}$ is a real, symmetric and positiv definite $dN \times dN$ matrix and, thus, can be diagonalized. This leads to a system of dN uncoupled harmonic oscillators [11]. These oscillators have discrete energies and are quantum mechanically described by a bosonic quasi-particle, called "phonon". If the view is expanded to a system with r atoms per unit cell, one has to solve dNr equations of motion. They have the form

$$M_\mu \frac{\partial^2}{\partial t^2} u_{j\mu\alpha} = \sum_{k,\mu',\beta} \Phi_{j\mu\alpha k\mu'\beta} u_{k\mu'\beta}, \tag{1.5}$$

where the index $\mu = (1, \dots, r)$ refers to the μ-th atom in the unit cell. The solutions of Eq. 1.5 have the form of travelling waves

$$\boldsymbol{u}_{j\mu}^{(l)} = \frac{1}{\sqrt{M_\mu}} \boldsymbol{e}_\mu^{(l)} \exp\left[i(\boldsymbol{q}\boldsymbol{R}_j - \omega^{(l)}(\boldsymbol{q})t + \varphi)\right], \tag{1.6}$$

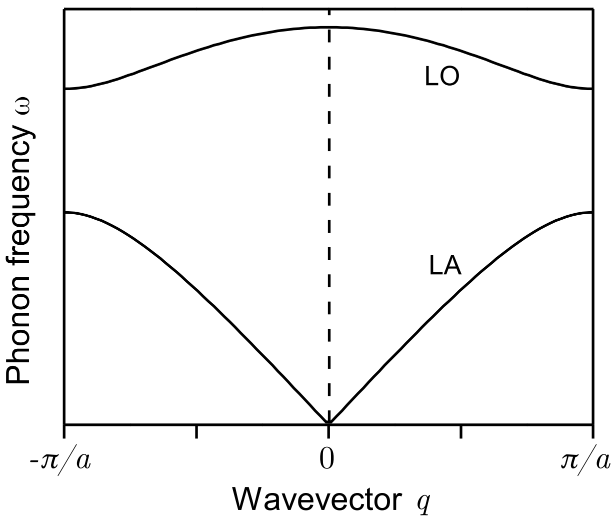

Figure 1-1: Typical phonon dispersion for a 1D lattice (d=1) with a basis of r=2 atoms. There are two solutions $\omega^{(l)}(q)$: one longitudinal acoustic (LA) and one longitudinal optical (LO) branch. The LA dispersion is linear for $q \approx 0$.

where φ is a phase factor [11]. The vectors $\boldsymbol{e}_\mu^{(l)}$ in Eq. 1.6 describe the direction of polarization. The index l runs from 1 to dr, because the translation symmetry of the *Bravais* lattice allows only dr different solutions of the angular frequency $\omega(\boldsymbol{q})$ for any of the N wavevectors $\boldsymbol{q}$ in the first *Brillouin* zone. There are d solutions $\omega(\boldsymbol{q})$ for which the atoms in the unit cell are oscillating in phase. They are regarded as acoustic phonons, and their dispersion decays linearly to zero for small $\boldsymbol{q}$. The remaining $d(r-1)$ solutions are called optical phonons [12]. Those solutions with $\boldsymbol{e}_\mu^{(l)} \| \boldsymbol{q}$ are called longitudinal phonons, while other solutions are called transverse phonons. An example of a phonon dispersion for a one-dimensional lattice with $r = 2$ atoms per unit cell is plotted in Fig. 1-1.

The total phonon contribution to the lattice energy is given by the sum

$$E_{harm} = \sum_{l,\boldsymbol{q}} \hbar\omega^{(l)}(\boldsymbol{q}) \left(n^{(l)}(\boldsymbol{q}) + \frac{1}{2} \right). \tag{1.7}$$

In thermal equilibrium, the occupation $n^{(l)}(\boldsymbol{q})$ of each energy state is desribed by *Bose-Einstein* statistics and the phonon phases φ are distributed randomly [11]. Non-equilibrium phonons, however, may have a fixed phase relationship and are called coherent phonons. Their ability to interfere with each other makes them particularly interesting for achieving strong perturbations.

In the next section, the limit of long phonon wavelengths will be discussed, for which the lattice transitions into a continuum. They can be described by the theory of elasticity. The main goal there is to introduce the stress tensor σ and, in particular, its relation to the strain η.

1.2 Limit of long wavelengths: elasticity

In the following it is assumed that the phonon wavelength is much larger than the lattice constants, so that the lattice can be treated as a continuum. Within this continuum, however, it is considered that a particle at $\boldsymbol{R}_j$ only feels the force of displacements $u_{j'\alpha'}$ of points $\boldsymbol{R}_{j'}$ in its direct proximity. Moreover, only acoustic phonons shall be taken into account, hence, the theoretical treatment can be restricted to just one atom per unit cell.

Over distances of a few lattice constants, there is only a small variation in $\boldsymbol{u}_j$. Therefore, $u_{j'\alpha'}$ can be written in a *Taylor* expansion:

$$\begin{aligned} u_{j'\alpha'} = u_{\alpha'}(\boldsymbol{R}_{j'}) =& u_{\alpha'}(\boldsymbol{R}_j) + \sum_{\beta} \frac{\partial u_{\alpha'}(\boldsymbol{R}_j)}{\partial x_\beta}(R_{j'\beta} - R_{j\beta}) \\ &+ \sum_{\beta,\beta'} \frac{\partial^2 u_{\alpha'}(\boldsymbol{R}_j)}{\partial x_\beta \partial x_{\beta'}}(R_{j'\beta} - R_{j\beta})(R_{j'\beta'} - R_{j\beta'}) + \ldots . \end{aligned} \tag{1.8}$$

This expansion is put into Eq. 1.5. When the transition to a continuous displacement field $\boldsymbol{u}(\boldsymbol{r}, t)$ is made and the mass density $\rho_m = M/V_{UC}$ is used [V_{UC}: unit cell volume], the following wave equation can be deduced [11]:

$$\rho_m \frac{\partial^2}{\partial t^2} u_\alpha(\boldsymbol{r}, t) = \sum_{\alpha',\beta\beta'} C_{\alpha\beta\alpha'\beta'} \frac{\partial^2}{\partial x_\beta \partial x_{\beta'}} u_{\alpha'}(\boldsymbol{r}, t). \tag{1.9}$$

The tensor $C_{\alpha\beta\alpha'\beta'}$ depends on the sum over the harmonic tensors $\Phi_{j\alpha j'\alpha'}$ of the harmonic potential and is called the elastic tensor.

From a different point of view, the acceleration of an infinitesimal volume ΔV within the continuous medium is proportional to the resulting force, which can be written as an integral over this volume [11, 14]:

$$\rho_m \int_{\Delta V} \frac{\partial^2}{\partial t^2} \boldsymbol{u}(\boldsymbol{r}, t) dV = \int_{\Delta V} \boldsymbol{F} dV. \tag{1.10}$$

In principle, there are two different types of forces: volume forces like gravity, and inner body forces, which act on the surface of the infinitesimal volume ΔV through the surfaces of surrounding volumes. Volume forces shall be neglected in the following treatment. The surface forces are composed of normal and shear components so that the components F_α can be written as the divergence of a 2nd order tensor $\sigma_{\alpha\beta}$ [14], which leads to the equations of motion for each dimension α in the form

$$\rho_m \frac{\partial^2}{\partial t^2} u_\alpha(\boldsymbol{r}, t) = \sum_{\beta} \frac{\partial}{\partial x_\beta} \sigma_{\alpha\beta}. \tag{1.11}$$

Here, $\sigma_{\alpha\beta}$ is the stress tensor. Equation 1.11 is equal to Eq. 1.9, if a linear relation between stress $\sigma_{\alpha\beta}$ and strain $\eta_{\alpha'\beta'}$ is assumed, commonly known as *Hook*'s law [11]

$$\eta_{\alpha'\beta'} = \frac{1}{2}\left(\frac{\partial u_{\alpha'}}{\partial x_{\beta'}} + \frac{\partial u_{\beta'}}{\partial x_{\alpha'}}\right), \tag{1.12}$$

$$\sigma_{\alpha\beta} = C_{\alpha\beta\alpha'\beta'} \cdot \eta_{\alpha'\beta'}. \tag{1.13}$$

From Eq. 1.13 it is obvious that the elastic tensor $C_{\alpha\beta\alpha'\beta'}$ is a measure for the resistivity of the material to be deformed by applied stress.
The stress-strain relationship 1.13 can be simplified, if an isotropic medium is assumed, for which the elastic properties do not depend on the material orientation. This assumption is valid, e.g., for metals. In this case the elastic tensor $C_{\alpha\beta\alpha'\beta'}$ has to be invariant against rotation [15]. This leads to a more simple stress-strain relationship [14], given by

$$\sigma_{\alpha\beta} = \sum_{\alpha'} \frac{Y}{(1+\nu)}\left(\eta_{\alpha\beta} + \frac{\nu}{1-2\nu}\eta_{\alpha'\alpha'}\delta_{\alpha\beta}\right), \tag{1.14}$$

where $\delta_{\alpha\beta}$ is the *Kronecker*-δ. The stress-strain relationship 1.14 now only depends on two scalar material constants, Y and ν. Here, Y is *Young*'s modulus and ν is the *Poisson* ratio.
In the next section the excitation mechanism of picosecond strain pulses is introduced, which is based on the application of optically induced thermal stress.

1.3 Optically induced picosecond strain pulses

In this section, the optically induced excitation mechanism of picosecond strain pulses is reviewed [16]. A thin metal film of thickness d acts as the opto-acoustic transducer, which is, in the experiments presented here, deposited on a semiconductor or dielectric substrate, as sketched in Fig. 1-2. A short light pulse with a duration $< 1\,\mathrm{ps}$ and with energy Q illuminates an area A of the metal film and is absorbed within a penetration depth $\zeta \ll d$, much smaller than the film thickness.
For simplicity, the normal of the metal film plane lies in the z-direction. The deposited energy $W_a(z)$ of the light pulse per unit volume has the following distribution

$$W_a(z) = (1-R)\frac{Q}{A\zeta}\exp\left[-\frac{z}{\zeta}\right], \tag{1.15}$$

where R is the optical reflectivity of the metal. In the following it is assumed that the energy is immediately transferred to the lattice and results in a temperature rise $\Delta T(z) = W_a(z)/c_V$, where c_V is the specific heat per unit volume. In general, this results in additional thermal stress that has to be added to the expression of the stress tensor, Eq. 1.13 [15]:

$$\sigma_{\alpha\beta} = C_{\alpha\beta\alpha'\beta'} \cdot \eta_{\alpha'\beta'} + a_{\alpha\beta}\Delta T, \tag{1.16}$$

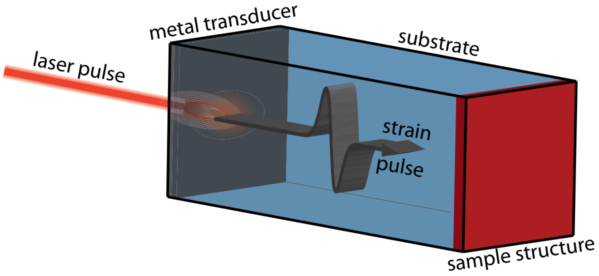

Figure 1-2: Scheme of the picosecond acoustics technique. A femtosecond laser pulse is incident on the metal transducer film, resulting in thermal stress. Thereby, a picosecond strain pulse is injected into the substrate, propagating at the speed of sound.

where $a_{\alpha\beta}$ is a 2nd-order tensor containing the thermoelastic moduli. However, as stated in the previous section 1.2, metals can be treated as elastically isotropic and the simplified stress-strain relation Eq. 1.14 may be used. Moreover, since the linear dimension of A is much bigger than ζ, the only motion is parallel to z, so that the only non-zero stress [strain] component is σ_{33} [η_{33}]. In this case, Eq. 1.16 can be reduced to [16]

$$\sigma_{33} = 3B\frac{(1-\nu)}{(1+\nu)}\eta_{33} - 3Ba\Delta T(z), \tag{1.17}$$

where a is the linear expansion coefficient and $B = Y/(3-3\nu)$ is the bulk modulus. The equation of motion 1.11, that has to be solved, reads:

$$\rho_m\frac{\partial^2 u_3}{\partial t^2} = \frac{\partial \sigma_{33}}{\partial z}. \tag{1.18}$$

Due to the simple one-dimensional form of Eq. 1.18, the indices of u, η and σ will be omitted in the following discussion.

When solving Eq. 1.18, the initial condition $\sigma(z, t = 0) = 0$ and the boundary conditions for $\sigma(z = 0, t)$ need to be obeyed. The solution $\eta(z, t)$ consists of two parts. The first part describes a thermal expansion that is localized near the boundary, at $z = 0$. It is time independent because, so far, instantaneous energy transfer and negligible damping or heat flow are assumed. This part is uninteresting for the current studies. The second part has the form:

$$\begin{aligned}\eta(z,t) &= -(1-R)\frac{Qa}{A\zeta c_V}\frac{(1+\nu)}{(1-\nu)}\exp\left[-|z-vt|/\zeta\right]\cdot\mathrm{sgn}[z-vt]\\ &= \eta_0\exp\left[-|z-vt|/\zeta\right]\cdot\mathrm{sgn}[z-vt].\end{aligned} \tag{1.19}$$

It describes a bipolar strain pulse with amplitude η_0 that is propagating in the z-direction at the longitudinal speed of sound [16]

$$v = \sqrt{3\frac{(1-\nu)}{(1+\nu)}\frac{B}{\rho_m}}. \tag{1.20}$$

In the quantum mechanical description it corresponds to a coherent phonon wavepackage. The pulse width is of the order $\sim 2\zeta$.

The assumption of an instantaneous energy transfer from the electron to the lattice system, however, is not necessarily valid. The electron-phonon coupling in metals is not strong enough to neglect electron diffusion over a distance $z_e > \zeta$ into the metal, before the energy is transferred to the lattice. A common way to take this into account is the two-temperature model, which assumes independent equilibrium temperatures T_e and T_p for the electron and lattice system, respectively. Directly after the optical excitation $T_e \gg T_p$, followed by a transfer from the electron to the lattice system [17, 18].
When both systems are in thermal equilibrium, the temperature T_p continues to vary due to thermal diffusion. If $1 \gg D/z_e v$ is not fulfilled [D: thermal diffusion constant], thermal diffusion plays an important role before the strain pulse leaves the heated area and cannot be neglected [16, 19]. For most metals $D/z_e v \sim 1$, so that thermal diffusion has to be considered.
Nevertheless, the applied principles described while developing Eq. 1.19 are sufficiently accurate to understand the main characteristics. Electron and thermal diffusion mainly result in lateral smoothing and stretching of the strain pulse shape $\eta(z, t)$.

Once the strain pulse propagates away from the open surface and reaches the interface between the metal transducer and the substrate, it will be partially reflected due to the impedance mismatch of the two materials. The acoustic amplitude reflection coefficient is

$$r_a = \frac{\rho_s v_s - \rho_m v}{\rho_s v_s + \rho_m v}, \tag{1.21}$$

where the subscripts s and m refer to the substrate and metal, respectively [19]. The transmission coefficient is given by $t_a = 1 - r_a$. The backtravelling pulse will be reflected again at the open surface, which leads to a ringing tail of the strain pulse that is propagating into the substrate. A typical temporal dependence of $\eta(z_s, t)$ at the interface between metal transducer and substrate [z_s=0], which takes into account all above mentioned effects, is shown in Fig. 1-3(a). Here, the optical excitation energy density is $W = 10\,\mathrm{mJ/cm^2}$ [20]. The parameter z_s describes a propagation distance into the substrate.

In the next section, the role of anharmonicity and dispersion for the temporal evolution of $\eta(z_s, t)$ after propagation distances $z_s \sim 10\ \mu\mathrm{m}$ will be discussed. It will turn out that the harmonic approximation is not valid anymore for strain amplitudes $\eta_0 \sim 10^{-3}$ and higher.

1.4 Strain pulse propagation: the role of anharmonicity

In the experiment, it is possible to optically excite strain pulses with amplitudes as high as $\eta_0 \sim 10^{-3}$. For such high amplitudes the harmonic approximation of the effective potential U_{eff} in Eq. 1.3 is no longer sufficient and anharmonic terms need to be included [21]. In the long wavelength limit, this can be taken into acount by expanding the elastic tensor $C_{\alpha\beta\alpha'\beta'}$ to include third-order terms in the wave equation 1.9. The

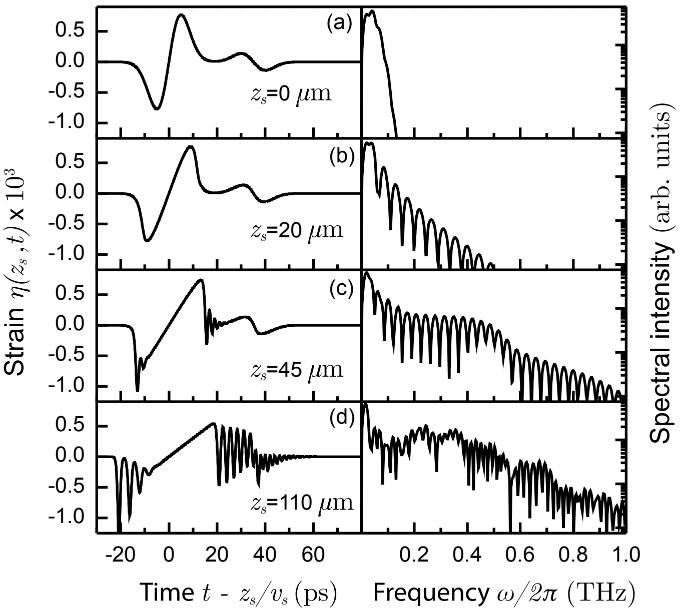

Figure 1-3: Left panel: temporal evolution of $\eta(z_s, t)$ after a propagation distance z_s into GaAs substrate. Right panel: spectral intensity of the corresponding strain pulse. (a) Strain profile, as it enters into the substrate, after optical excitation with excitation energy density $W = 10\,\mathrm{mJ/cm^2}$. (b)/(c) Formation of an N-shaped shockwave due to non-linear propagation at $z_s = 20$ µm/40 µm. (d) Acoustic solitons at the leading edge, due to balancing between anharmonic and dispersive effects, at $z_s = 110$ µm. [20]

geometrical conditions of the experiments performed in this work permit to consider only longitudinal waves in high-symmetry directions, e.g., (100) in GaAs. In this case one can apply the anharmonic expansion to Eq. 1.9 in the form

$$\rho_s \frac{\partial^2}{\partial t^2} u = \left(C_2 + C_3 \frac{\partial}{\partial z} u \right) \frac{\partial^2}{\partial z^2} u, \tag{1.22}$$

where C_2 and C_3 are combinations of 2nd and 3rd order elastic constants [21].
For phonon frequencies ∼0.1-1.0 THz, one also has to account for a non-linear dispersion $\omega(q)$ which results in a frequency dependent sound velocity v_s [20]. Accordingly, the following expansion is used:

$$\omega = v_s q - \gamma q^3 + \ldots, \tag{1.23}$$

where γ is a constant. Equation 1.22 needs to be extended, so that it yields Eq. 1.23 for small amplitudes. If it is written for strain $\eta = \frac{\partial}{\partial z} u$ instead of the displacement, the non-linear wave equation of the form

$$\rho_s \frac{\partial^2}{\partial t^2} \eta = C_2 \frac{\partial^2}{\partial z^2} \eta + C_3 \frac{\partial}{\partial z} \left(\eta \frac{\partial}{\partial z} \eta \right) + 2 \rho_s v_s \gamma \frac{\partial^4}{\partial z^4} \eta \tag{1.24}$$

can be derived [21]. If Eq. 1.24 is used to describe the evolution of a strain pulse $\eta(z, t)$ as shown in Fig. 1-3(a), the original shape will no longer be conserved, as it would for the linear wave equation. Instead, it will be distorted during its propagation.
Initially, the distortion arises from an amplitude dependence of the sound velocity v_s. The compressive parts will propagate faster and the tensile parts slower, which leads to the formation of an N-shaped shockwave front [Figs. 1-3(b) and (c)]. The steepening of the leading edge of the shockwave goes hand in hand with an increase of high-frequency components, as can be seen from the corresponding spectral intensities

in Fig. 1-3. These high-frequency components, however, are slowed down due to dispersion. This results in the formation of special solutions of the *Korteveg de Vries* form, called acoustic solitons [22, 23, 21]. For solitons, anharmonicity and dispersion are balanced and form a stable wavepackage that travels at a fixed sound velocity $> v_s$ at the leading edge of the strain pulse, see Fig. 1-3(d).
The pulse duration of just $\sim$ 1 ps and a resulting extension of $\sim$ 1 nm in typical semiconductors and dielectrtics makes picosecond strain pulses a very promising tool for the investigation and manipulation of nanostructures at sub-terahertz frequencies, as already demonstrated by a number of works, e.g., [24, 25, 26, 27, 28].

In part II of this work, picosecond strain pulses are used to shift the electronic energy levels in semiconductor quantum dots by about 10 meV, on timescales faster than their thermal emission dynamics. Hereby, a detuning with respect to a cavity mode of similar magnitude can be compensated to feed the quantum dot emission into the cavity mode.

In part III, a coherent phonon wavepackage will be utilized to modulate a surface plasmon resonance, as well as to probe the electromagnetic far-field inside a sample with a periodic metal grating on top.

2

Experimental methods

In this chapter, the experimental methods, used to obtain the results presented in this thesis, are introduced. Strain induced dynamics of various sample systems is investigated. Picosecond strain pulses correspond to coherent phonon wavepackages, where the phonon frequencies may reach the THz range. The induced dynamics can contain similar frequency components, which demands time-resolved detection schemes with picosecond time resolution.

In part II, the effect of picosecond strain pulses on the emission dynamics of a quantum dot microcavity laser are investigated. Depending on the regime of emission, the characteristic time scales for emission may vary from $\sim$ ns down to $\sim$ 10 ps, which have to be detected in real time. Such a time-resolution in real-time measurements can be achieved with a streak camera. The experimental setup, used for the time-resolved detection of emission is introduced in section 2.1.

In part III, the dynamics of surface plasmon polaritons due to the perturbance by coherent phonons are studied. The effect is detected by measuring the changes in the reflected intensity of an optical probe pulse with an energy close to a surface plasmon or waveguiding mode. To resolve the dynamics, a pump-probe technique is applied. In section 2.2, the experimental setup for pump-probe measurements of the differential reflectivity is introduced.

An outline of each experiment is also given in the respective chapters in part II and III, so that the reader may skip this chapter, if technical details are of minor importance.

2.1 Time-resolved detection of emission

A sketch of the experimental setup is plotted in Fig. 2-1. It is basically build out of four essential elements: the laser systems [black boxes], a helium bath cryostat

[blue circle], the optical setup, and synchronisation/detection electronics [gray boxes]. Optical pathways are sketched in color, while electronic wire connections are illustrated in black.
The excitation of strain pulses by picosecond acoustics requires femtosecond laser pulses with high energy per pulse to reach excitation energy densities of about 1 mJ/cm^2 on the metal transducer, see chapter 1. To achieve this with moderate focussing to spot sizes with linear dimensions of 100 µm, the energy per pulse has to be $\sim$ 1 µJ. For this purpose, a regenerative amplifier builds the core of the experimental setup [Coherent, RegA 9000]. The RegA is seeded by a Ti:Sapphire laser [Coherent, Vitesse], providing 150 fs pulses with a central wavelength of $\lambda = 800$ nm at a repetition rate of 80 MHz. Seed pulses with $\sim$ nJ energy per pulse are amplified by the regenerative amplifier to an energy of $\sim \mu J$ per pulse, at the cost of a lower repetition rate of only 100 kHz. The energy is provided by a 12 W Nd:YVO$_4$ continuous wave (CW) laser [Coherent, Verdi V12], which pumps a Ti:Sapphire crystal inside the regenerative amplifier.

The main part of the RegA output is used for the strain excitation on the backside of the sample (S), referred to as pump pulse. Selectively, a part of the RegA output can be split off by a beam splitter (BS) to be used as the pulsed option (*i*) for the optical excitation of quantum dot microcavity laser emission. In this case, the split off pulse is travelling an extra path length, corresponding to a delay time t_S that is needed for the strain pulse to propagate through the sample substrate and to reach the center of the

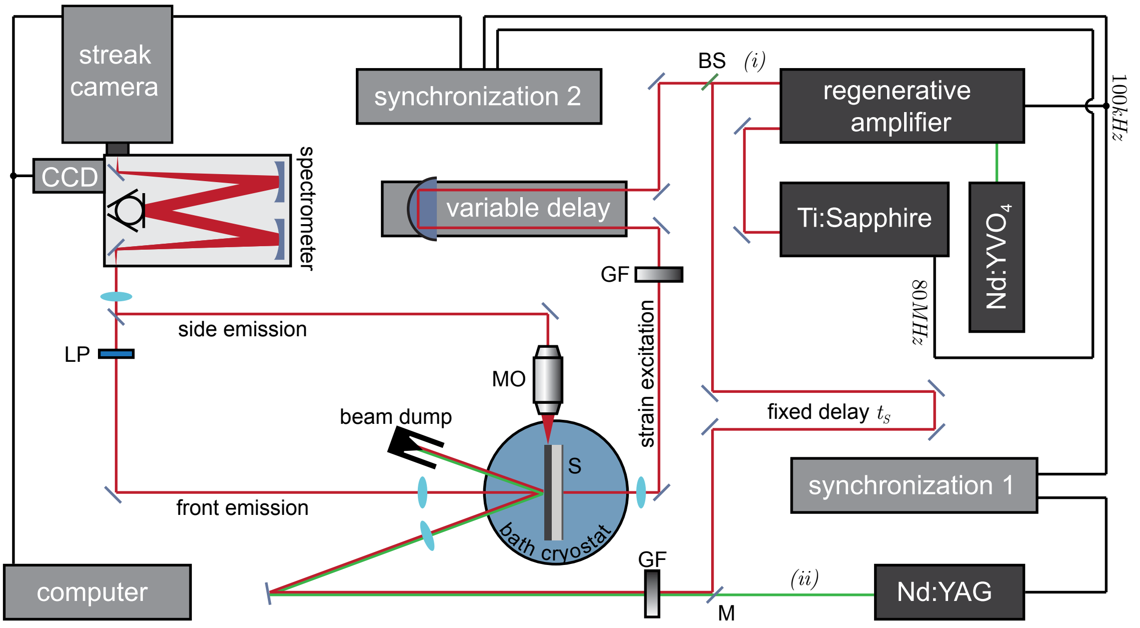

Figure 2-1: Time-resolved emission spectroscopy setup to detect strain induced changes in the emission intensity of a quantum dot microcavity laser. Two light sources for the optical excitation of laser emission are available, a pulsed regenerative amplifier system (*i*) and a Q-switched, frequency doubled Nd:YAG "quasi-CW" laser (*ii*). Side and front emission can be resolved in energy and time by the combination of a spectrometer and a streak-camera with a resolution of 0.12 meV and 30 ps, respectively.

microcavity laser. An additional, remote controlled, mechanical delay line [Aerotech, ATS-125] is positioned in the optical path of the strain excitation, which allows to vary the time separation $t_0 - t_S$ between the pulsed optical excitation of emission and strain pulse arrival at the cavity center. To ensure spatial overlap between the strain pulse and the optically active region of the microcavity laser, the pump pulse is defocused to a spotsize of about 100 µm, while the optical pulse, that excites the laser emission is focused to a spot size of about 35 µm.
Option (*ii*) for the optical excitation of quantum dot microcavity emission, by removing the mirror M, is a Q-switched, frequency-doubled Nd:YAG laser [SpectraPhysics, BL6S 532Q], emitting pulses at a central wavelength of 532 nm. The nominal pulse duration is $<$ 10 ns, but it was measured to be 23 ns, using this streak camera setup. In any case, it is about an order of magnitude longer than all characteristic time constants of the quantum dot microcavity emission, so that option (*ii*) may be called "quasi-CW". The Q-switch of the quasi-CW laser can be controlled externally, by a pulse generator [Quantum Composers, 9520 series], sketched as "synchronization 1" in Fig. 2-1. The pulse generator is triggered by the 100kHz clock of the regenerative amplifier and, thereby, the strain and emission excitations are synchronized.
The excitation intensity can be varied by a gradient grayfilter (GF) and is measured with a powermeter [Coherent, FieldMax II], using a semiconductor powerhead [Coherent, OP-2-VIS].

To suppress phonon and carrier scattering, the sample (S) is mounted in the variable temperature insert (VTI) of a helium bath cryostat. Two different cryostats have been used. When the microcavity laser emission to the front is collected by an achromatic lens [focus length of 15 cm], a cryostat with active temperature stabilization [Oxford, Spectromag] is used. The sample is exposed to helium vapor at $T = (10 \pm 0.1)$ K. In another configuration, the quantum dot emission is recorded from the side of the

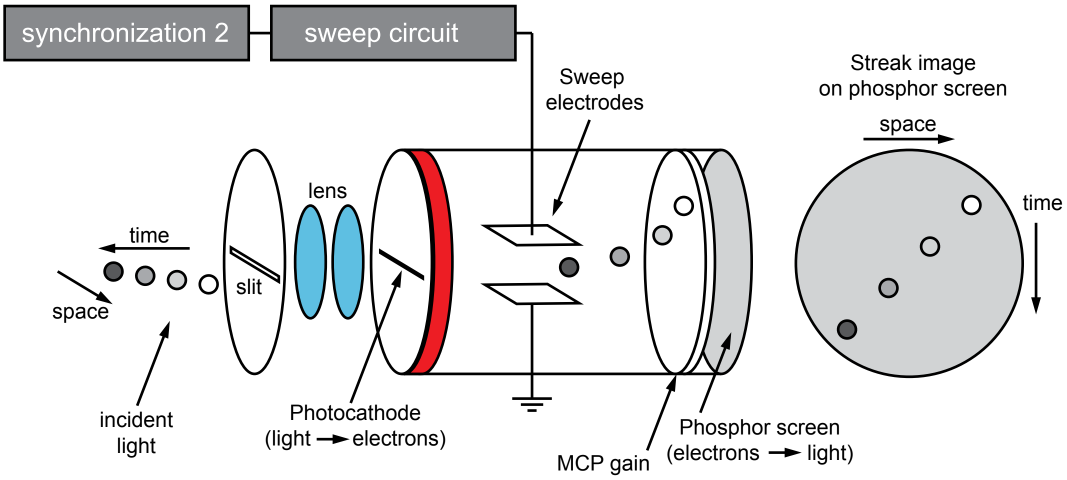

Figure 2-2: Operation principle of the streak camera. Incident light is converted into electrons in a photocathode. A time-dependent voltage, applied to the sweep electrodes in the streak tube is deflecting the electrons vertically. This generates a time resolution $<$ 50 ps on the vertical axis of a phosphor screen, which transfers the electrons back into light.

structure, where there is no optical confinement. Due to the small thickness of the microcavity structure of just a few µm, the emission to the side is collected by a 10x microscope objective [MO] with a nominal spatial resolution of 1.1 µm [Mitutoyo, Plan Apo NIR] . The microscope objective has a working distance of 33.5 mm, so that a cryostat with a smaller VTI is used [CryoVac, Spektro]. This cryostat does not have an active temperature stabilization, resulting in a temperature stability of ±0.5 K.

The collected emission is focused on the vertical entrance slit of a spetrometer with $0.5m$ focal length and a 600 grooves/mm diffraction grating [Acton, Spectra Pro 2500i]. Using the front exit with a mounted charge-coupled device (CCD) camera [Princeton Instruments, Pixis], time-integrated emission intensity spectra $I(E)$ with a spectral resolution of 0.12 meV can be recorded.
Alternatively, using the side exit of the spectrometer, the energy-resolved emission is focused on the horizontal entrance slit of a streak camera [Hamamatsu, C5680] to resolve it in time. A scheme with the operating principle of the streak camera is plotted in Fig. 2-2. The incoming light is imaged on an InGaAs photocathode [Hamamatsu, S-1], which transforms light into a stream of electrons and is sensitive up into the near infrared. The train of electrons is sweeped vertically by a sweep electrode, which is operated by a slow single-sweep unit [Hamamatsu, M5677] with a nominal temporal resolution of $<$ 50 ps. A microchannel plate (MCP) is multiplying the number of electrons before they hit a phosphor screen that turns electrons back into light. After this procedure the emission is vertically resolved in time and horizontally resolved in space or energy, by use of a spectrometer. The temporally- and spectrally resolved emission intensity $I(t, E)$ is finally detected by a CCD camera [Hamamatsu, Orca-ER].
The sweeping unit and, thereby, the monitored time window has to be synchronized with the laser system [synchronization 2 in Fig. 2-1 and 2-2]. The synchronization electronics consist of a pulse generator [Stanford Research Systems, DG-535] for the timing, triggered by the 100 kHz clock of the regenerative amplifier. To minimize the electronic jitter, the output of the pulse generator is stabilized by the 80 MHz clock of the Ti:Sapphire oscillator, using the streak trigger unit [Hamamatsu, C4547-02]. Finally, the signal $I(t, E)$ has a time resolution of 25 ps.

To be able to detect also weak emission, when the quantum dot microcavity laser is operated in the spontaneous emission regime, the spectrometer can be replaced by a longpass filter (LP), suppressing bulk emission and scattered excitation laser light with energy $>$ 1.37 eV. The detection sensitivity can, thereby, be improved by an order of magnitude, at the cost of energy resolution.

2.2 Pump-probe detection of differential reflectivity

The effect of picosecond strain pulses on the intensity of a reflected probe pulse with energy close to a surface plasmon or waveguiding mode shall be investigated. A draft of the experimental setup is plotted in Fig. 2-3. It contains two alternative light sources [black boxes, (i) and (ii)], and two alternative detection schemes to measure either reflectivity spectra $R(\lambda)$ or time-resolved reflected intensity $I(t)$ [orange boxes]. Optical pathways are sketched in red, while electronic wire connections are shown by black lines. To resolve the incidence angle θ, the sample (S) is mounted on a goniometer, with the option to cool it down to $T = 10\,\mathrm{K}$ in a helium bath cryostat [Oxford, Spectromag].

To characterize the plasmonic grating sample, angle- and polarization-resolved reflectivity spectra $R(\lambda)$ are measured, using light-source option (i). White light from a high stability tungsten-halogen light-source [Spectral products, ASB-W-030] is incident on the sample under various angles θ. Before hitting the sample, the light is linearly polarized by the combination of a waveplate ($\lambda/2$) and a *Glan-Thompson* prism (GTP), mounted in rotation holders to vary the polarization orientation. The specularly reflected light is focused on the entrance slit of a spectrometer with $0.5m$ focal length and a 600 grooves/mm diffraction grating [Acton, Spectra Pro 2500i]. A CCD camera [Princeton Instruments, Pixis] is recording reflectivity spectra $R(\lambda)$ with a resolution of 0.08 nm.

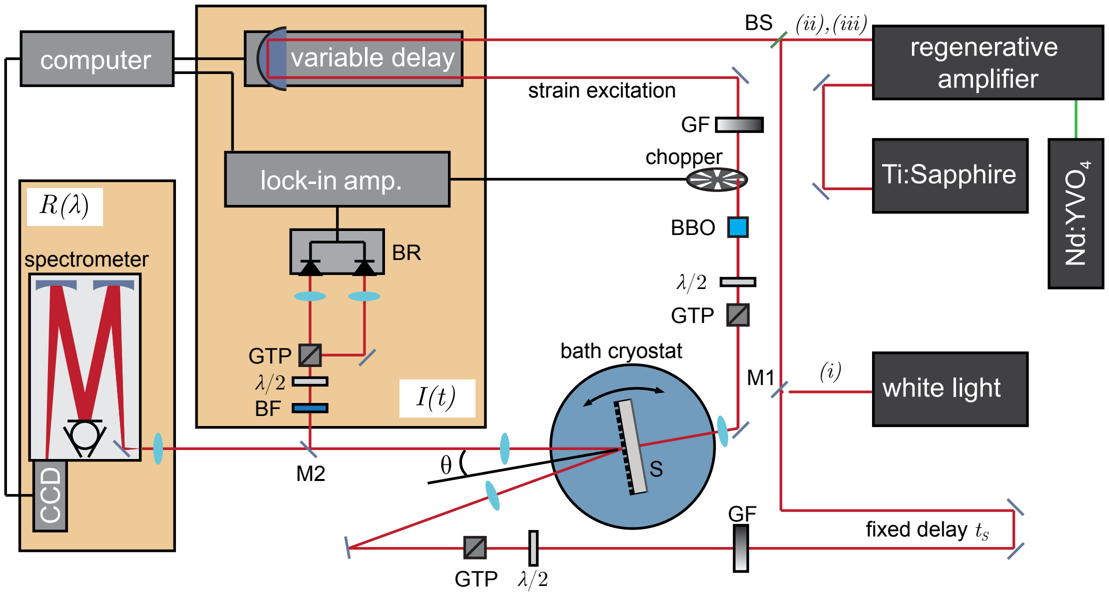

Figure 2-3: Experimental setup to characterize and manipulate surface plasmons in a metal grating sample, by coherent phonons. Two different types of light sources are available for the detection; a white light source (i), and regenerative amplifier systems (ii),(iii). The sample is mounted on a goniometer and, optionally, in a cryostat. The specularly reflected probe light can be analyzed spectrally [scheme $R(\lambda)$] or time-resolved [scheme $I(t)$].

The light source options (*ii*) and (*iii*) are regenerative amplifier systems. The optical pulses of system (ii) have a spectral width of $\Delta\lambda = 15$ nm at a repetition rate of 100 kHz [Coherent, RegA 9000]. The RegA is pumped by the second harmonic of a 12 W Nd:YVO$_4$ laser [Coherent, Verdi V12] and seeded by a Ti:Sapphire laser that provides 150fs pulses [Coherent, Vitesse]. The alternative amplifier option (*iii*) provides pulses with a spectral width of $\Delta\lambda = 50$ nm at a repetition rate of 5 kHz [Spectra Physics, Spitfire-Pro]. It is seeded by a Ti:Sapphire laser with < 100 fs pulses [Spectra Physics, Tsunami Broadband fs] and pumped by a 4W Nd:YVO$_4$ laser [Spectra Physics, Millennia]. Both amplifier systems operate at a central wavelength of $\lambda = 800$ nm and provide optical pulses with an energy per pulse of $\sim$ µJ.

For measurements of the strain-induced dynamics, the main part of the regenerative amplifier output is used for the strain pulse excitation on the backside of the sample [pump pulse]. The sample substrate is transparent for $\lambda = 800$ nm. To prevent pump light from entering the detection channel, the pump pulse is frequency doubled in a beta barium borate crystal (BBO), before it hits the opto-acoustic transducer, so that it can be filtered. Further, it is linearly polarized by a combination of a waveplate ($\lambda/2$) and *Glan-Thompson* prism (GTP), with a polarization orientation perpendicular to the probe light.
A part of the regenerative amplifier output is split off by a beam splitter (BS) and is used as an optical probe pulse. The optical path length of the probe pulse is longer than for the pump pulse, corresponding to a delay of t_S, the time which the strain pulse needs to propagate through the sample substrate. To verify the spectral overlap with a surface plasmon or waveguiding mode, the reflected probe pulse spectrum can be recorded in the $R(\lambda)$ detection scheme.
In the other detection scheme, the strain-induced changes in the reflected intensity $I(t)$ of the probe pulse are detected by a balanced photoreceiver (BR) with two silicon photodiodes [New Focus, Nirvana Model 2007]. The signal $I(t)$ is resolved in time by a pump-probe technique. For each measurement the difference in optical path length between pump and probe pulse is varied, by a remote controlled mechanical delay line [Aerotech, ATS-125], in steps of $\delta l = 0.5$ mm, corresponding to a time resolution of about $2c\delta l \approx 3.3$ ps.
Scattered pump light is filtered by a blue filter. The output voltage of the BR is proportional to the intensity difference in both channels. If one channel is closed, the output is directly propotional to $I(t)$. For a better signal-to-noise ratio, the pump pulse is modulated by a mechanical chopper [Stanford Research Systems, Model SR540 Chopper] with a frequency of $f_{chop} = 1600$ Hz, linked to a lock-in amplifier [Signal Recovery, Model 7225]. The BR signal is sent to the lock-in amplifier, whose output is proportional to the differential reflected intensity $\Delta I(t) = I(t) - I_0$, with and without strain pulse perturbation. When measuring $\Delta I(t)/I_0$ with a single photodiode, signal amplitudes of 5.0×10^{-6} can be resolved.
Surface plasmons can only be excited by incident light, linearly polarized parallel to the lattice vector of the gold grating [*p*-polarization, see chapter 8]. For the perpendicular polarization [*s*-polarization], the signal $I(t)$ contains no plasmonic contribution. A further increase in the signal-to-noise ratio can, therefore, be achieved by choosing the polarization plane of the incident pulse in such a way that p- and s-polarization

components are equal in magnitude. A GTP is splitting the reflected probe pulse into two components with perpendicular polarizations, before they are focused on the two photodiodes of the BR. The unperturbed intensity in both channels can be balanced by a $\lambda/2$ before the GTP. Thereby, the s- and p-polarization components are separated, so that the BR measures their difference. By this method, signal amplitudes $\Delta I(t)/I_0$ of 1.5×10^{-6} can be resolved.

Part II

Shaking quantum dot lasers

The technological advancements in recent years made it possible to fabricate high quality optical semiconductor resonators on the micrometer scale, using atomically precise epitaxy and high-resolution lithographic patterning [29]. The modified light-matter interaction for a semiconductor light-emitter, placed into such resonators, has led to a number of spectacular demonstrations. Outstanding examples are the enhanced spontaneous emission of quantum dots in micropillars [30], the strong coupling regime for a quantum well [31] and a quantum dot [32, 33] in a microcavity, the realization of efficient single-photon [34] and entangled-photon [35, 36, 37] sources based on quantum dot resonators, and the demonstration of condensation phenomena for polaritons in quantum well cavities [38, 39, 40, 41]. The necessary requirement in all these demonstrations is that the electronic transition involved in light generation is in resonance with the optical cavity mode.

Fulfillment of the resonance condition can often be achieved by the fabrication process, but it may be a demanding task. An example is a single quantum dot inside a resonator. In other cases it is impossible to achieve resonance by the fabrication process alone. A particular example is the microlaser under study in this work. Here, an ensemble of self-assembled quantum dots placed at the center of a planar bragg microcavity is investigated. The inhomogeneous broadening of the ensemble is much bigger than the cavity mode linewidth, so that the resonance condition is fulfilled only for a small dot fraction.

One might tune the electronic transition energy to compensate the detuning with respect to the cavity mode. This, for example, is possible by applying electric [42] or magnetic fields [43] and by varying the sample temperature [32, 33]. These methods, however, suffer from negative side effects. For example, high electric fields may lead to carrier tunneling out of the nanostructure, magnetic field-induced shifts are typically small, and a temperature increase leads to advanced carrier scattering.
In this work, an alternative, non-detrimental method is used. It is based on the application of picosecond strain pulses, excited by the picosecond acoustics technique [16], introduced in chapter 1. When hitting the quantum dots, the strain pulse induces energy shifts in the order of $\sim 10\,\mathrm{meV}$ within picoseconds [27].

In the following, a brief recap of the theory describing laser operation in a quantum dot microcavity will be given in chapter 3. In chapter 4, using the deformation potential formalism, the interaction of the strain pulse with the electronic system will be described. The quantum dot microcavity laser under study will be characterized in chapter 5. In chapter 6, laser mode feeding by shaking off-resonant quantum dots will be demonstrated, by dynamically inducing resonance with the optical mode for a much larger quantum dot fraction. As a result the lasing threshold can be crossed and the output intensity is enhanced by more than two orders of magnitude. Finally, in chapter 7, it will be shown that the microcavity structure itself acts as a phonon filter, so that individual frequency components of the strain pulse arrive at the quantum dot layer with a delay. Such delayed phonons are used to harmonically modulate the laser emission intensity at a frequency of 17 GHz, if the device is operated in the lasing regime.

3

Semiconductor quantum dot microcavity lasers

In this chapter, a theory, able to describe laser operation in semiconductor microcavities, shall be recaped. The chapter starts with an introduction of light-matter interaction in section 3.1, where the focus will be on the most simple case; a system of two-level atoms. In section 3.2 the laser rate equations will be derived by expanding to a four-level system and coupling it to a resonator. In particular, the importance of popluation inversion to reach positive gain and allow laser operation will be explained. In the subsequent section 3.3, the gain of semiconductor quantum dots will be examined and similarities to the previous model system will be highlighted. Finally, in section 3.4, planar *Bragg* microcavities will be introduced as the resonator of choice, pointing out their strengths. In the end, a particular limitation will be pointed out, which will be important in the following chapters, where this limitation shall be overcome, or even be exploited.

If not explicitely stated otherwise, the information presented in section 3.1 and 3.2 have been exclusively taken from Ref.[44].

3.1 Light-matter interaction

The investigation of light-matter interaction shall be started with the most simple case of an electron in a two level atom. It can be described by the wavefunction $\psi_a(t) = a_1(t)\,|1\rangle + a_2(t)\,|2\rangle$ that has to solve the time dependent *Schrödinger* equation:

$$\frac{\partial}{\partial t}\psi_a(t) = H_{int}\psi_a(t), \qquad H_{int} = H_0 + V_{ext}(\boldsymbol{x}, t), \tag{3.1}$$

where H_0 is the Hamiltonian of the bound electron, and $V_{ext} = -e\boldsymbol{x}\boldsymbol{E}(t)$ describes the interaction of an external field $\boldsymbol{E}(t)$ with the electronic dipole of the electron. The electronic dipole approximation, which states that the field amplitude $\boldsymbol{E}(t)$ does not change over atomic distances, has already been applied. In this case $\boldsymbol{E}(t)$ has the form:

$$\boldsymbol{E}(t) = \boldsymbol{\varepsilon} E_0(t) e^{-i\omega t} + c.c., \tag{3.2}$$

where ω is the photon frequency and $\boldsymbol{\varepsilon}$ is the unity vector, which defines the field polarisation. If ω is close to the frequency ω_0, associated with the energy separation $\hbar\omega_0$ between the atomic levels $|1\rangle$ and $|2\rangle$ [see Fig. 3-1(a)], i.e. if the external field is close to resonance, one may introduce new probability amplitudes $c_1(t) = a_1(t)$ and $c_2(t) = a_2(t)e^{i\omega t}$. Moreover, in case of optical frequencies $\omega \approx 10^{15}$/s, $E_0(t)$ is varying much slower than $e^{-i\omega t}$ and one may apply the rotating wave approximation, neglecting all fast oscillation terms $\propto e^{2i\omega t}$, due to averaging. In this case Eq. 3.1 reduces to the following coupled equations:

$$\begin{aligned} i\frac{\partial}{\partial t}c_1(t) &= -\frac{1}{2}\chi^* c_2(t), \\ i\frac{\partial}{\partial t}c_2(t) &= (\omega - \omega_0)c_2(t) - \frac{1}{2}\chi c_1(t). \end{aligned} \tag{3.3}$$

Here, $\chi = e\langle 2|\,\boldsymbol{x}\,|1\rangle\,\boldsymbol{\varepsilon}E_0(t)/\hbar$ is the exchange energy in frequency units.

Up to now, only the interaction of a single two level atom with an external field has been described. To account for macroscopic effects that involve many atoms and to include quasi-random relaxation processes like collisions, it is beneficial to use the density matrix formalism. The density matrix ρ is a 2×2 matrix with the following

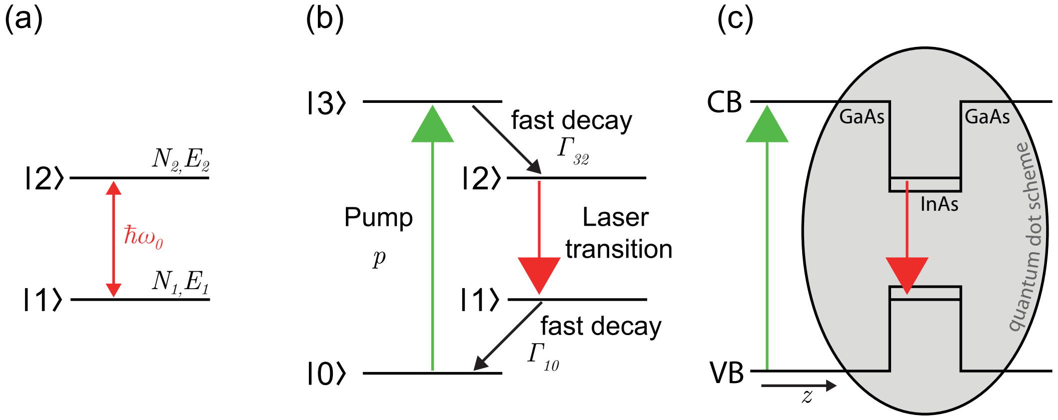

Figure 3-1: (a) Two-level system with populations $N_{1,2}$, Energies $E_{1,2}$ and energy separation $\hbar\omega_0$. (b) Expansion to a four-level system to reach population inversion for the laser transition $|2\rangle \rightarrow |1\rangle$, by pumping $|0\rangle \rightarrow |3\rangle$ at the rate p. (c) Sketch of the energy level scheme of a semiconductor quantum dot. The pumping occurs from the valence band (VB) into the conduction band (CB) of the surrounding material, while the quantum dot ground state decay is used as the laser transition.

entries:

$$\begin{aligned} \rho_{11} &= |c_1(t)|^2 \qquad & \rho_{12} &= c_1(t)c_2^*(t) \\ \rho_{21} &= c_2(t)c_1^*(t) \qquad & \rho_{22} &= |c_2(t)|^2. \end{aligned} \tag{3.4}$$

The elements ρ_{11}, ρ_{22} describe the population probabilities, while ρ_{12}, ρ_{21} describe the polarisation. Substituting these into Eq. 3.3 leads to the *von Neumann* equation, describing the dynamics of the system:

$$i\hbar\frac{\partial}{\partial t}\rho = [H_{int}, \rho]\,. \tag{3.5}$$

3.2 Rate equations

Quasi-random relaxation processes result in dephasing at a total rate of

$$\beta = \gamma_c + \frac{1}{2}(\Gamma_1 + \Gamma_2 + A_{21}), \tag{3.6}$$

where γ_c describes the dephasing rate due to elastic collisions, A_{21} is the relaxation rate due to spontaneous emission, and Γ_1,Γ_2 are scattering rates out of state $|1\rangle$ and $|2\rangle$. In many cases γ_c is the dominant term, because the chance for collisions is high and it is not restricted to the energy $\hbar\omega_0$. Furthermore, if one is only interested in times $t \gg \beta^{-1}$, the adiabatic approximation may be applied. This means: $\frac{\partial}{\partial t}\rho_{12} \approx 0$, $\frac{\partial}{\partial t}\rho_{21} \approx 0$ and one may express ρ_{12}, ρ_{21} in Eq. 3.5 in terms of ρ_{11} and ρ_{22}. Combining these assumptions leads to the following set of coupled equations for the dynamics, which only depend on the population probabilities:

$$\begin{aligned} \frac{\partial}{\partial t}\rho_{11} &= -\Gamma_1\rho_{11} + A_{21}\rho_{22} + \frac{1}{2}\frac{|\chi|^2\beta}{(\omega-\omega_0)^2+\beta^2}(\rho_{22}-\rho_{11}) \\ \frac{\partial}{\partial t}\rho_{22} &= -(\Gamma_2 + A_{21})\rho_{22} - \frac{1}{2}\frac{|\chi|^2\beta}{(\omega-\omega_0)^2+\beta^2}(\rho_{22}-\rho_{11}). \end{aligned} \tag{3.7}$$

Averaging over all polarisation directions, identifying the Intensity $I = c\varepsilon_0|E_0|^2/2$ and the atomic cross section $\sigma(\omega) = BS(\omega)\hbar\omega/c$ [B: Einstein-coefficient for stimulated absorption and emission; $S(\omega)$: spectral line profile] leads to the rate equations for the populations $N_1 = N\rho_{11}$ and $N_2 = N\rho_{22}$ of a system with N two level atoms per unit volume:

$$\begin{aligned} \frac{\partial}{\partial t}N_1 &= -\Gamma_1 N_1 + A_{21}N_2 + \frac{\sigma I}{\hbar\omega}(N_2 - N_1) \\ \frac{\partial}{\partial t}N_2 &= -\Gamma_2 N_2 - A_{21}N_2 - \frac{\sigma I}{\hbar\omega}(N_2 - N_1). \end{aligned} \tag{3.8}$$

The last term in Eqs. 3.8 describes the stimulated processes. The magnitude is identical for absorption and emission, which means the maximum reachable population inversion in the two level system due to stimulated processes is $N_2 = N_1$.

The external field has to be described by *Maxwell*'s equations. Thus, it has to satisfy

$$\nabla^2 \boldsymbol{E} - \frac{1}{c^2}\frac{\partial^2}{\partial t^2}\boldsymbol{E} = \frac{1}{\varepsilon_0 c^2}\frac{\partial^2}{\partial t^2}\boldsymbol{P}, \tag{3.9}$$

where $\boldsymbol{P}$ is the microscopic polarisation. To include the propagation through the homogeneous medium in z-direction, Eq. 3.2 is expanded to the form:

$$\boldsymbol{E}(z,t) = \boldsymbol{\varepsilon} E_0(z,t) e^{-i\omega(t-z/c)}. \tag{3.10}$$

For slowly varying amplitudes, as assumed before, the right hand side of Eq. 3.9 can be approximated by

$$\frac{\partial^2}{\partial t^2}\boldsymbol{P} = -2N\omega^2 e \left\langle 1 \right| \boldsymbol{x} \left| 2 \right\rangle \rho_{21} e^{-i\omega(t-z/c)}. \tag{3.11}$$

Still, only times $t \gg \beta^{-1}$ are considered, where the adiabatic approximation is applied, to express ρ_{21} in terms of the population probabilities. Finally, the intensity I is of interest, so that the field is replaced by $I = c\varepsilon_0 |E_0|^2/2$. If these assumptions are combined in Eq. 3.9, the rate equation for the intensity I can be derived:

$$\frac{1}{c}\frac{\partial}{\partial t}I + \frac{\partial}{\partial z}I = \sigma(\omega)(N_2 - N_1)I = g(\omega)I, \tag{3.12}$$

where

$$g(\omega) = \frac{\hbar\omega}{c}BS(\omega)(N_2 - N_1) \tag{3.13}$$

is the gain coefficient.

For a positive gain coefficient, a positive population inversion $(N_2 - N_1)$ is required. However, in a two level system, it is impossible to get $N_2 > N_1$, because stimulated absorption and emission are equal in magnitude [Eq. 3.8]. One possible way to overcome this is to switch to a four-level scheme, as shown in Fig. 3-1(b). One keeps $\left|1\right\rangle \rightarrow \left|2\right\rangle$ as the transition for laser operation, but pumps $\left|0\right\rangle \rightarrow \left|3\right\rangle$, at a rate p.

In order for this scheme to work, the decay rates Γ_{32} and Γ_{10} have to be high. If Γ_{32} is considered to be much higher than any other rate, the approximation $N_3 = 0$ may be used. Under these circumstances, Eq. 3.8 may be expanded to:

$$\begin{aligned}
\frac{\partial}{\partial t}N_0 &= -pN_0 + \Gamma_{10}N_1 \\
\frac{\partial}{\partial t}N_1 &= -(\Gamma_1 + \Gamma_{10})N_1 + A_{21}N_2 + \frac{\sigma I}{\hbar\omega}(N_2 - N_1) \\
\frac{\partial}{\partial t}N_2 &= pN_0 - \Gamma_2 N_2 - A_{21}N_2 - \frac{\sigma I}{\hbar\omega}(N_2 - N_1).
\end{aligned} \tag{3.14}$$

For stationary conditions, the populations fulfill $N_0 + N_1 + N_2 = N = const$, and in case of $\Gamma_{10} \gg A_{21}, p$ one can reach $N_1 \approx 0$.

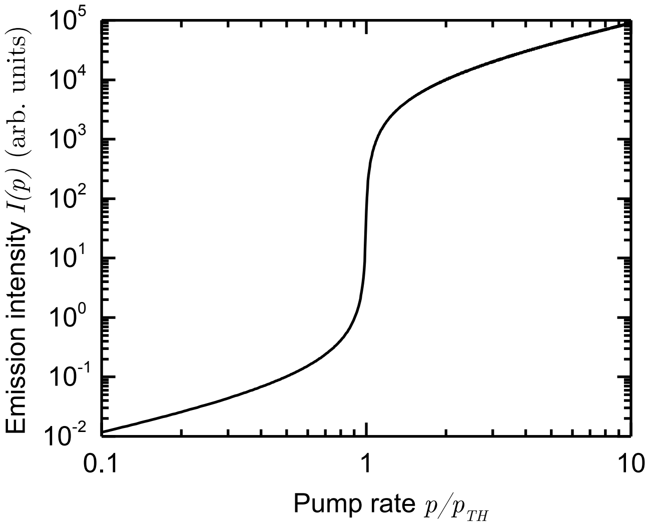

Figure 3-2: Characteristic input-output behaviour of the laser emission intensity $I(p)$. At the threshold pumping rate p_{TH}, the emission is channeled into the laser mode, leading to a jump in I.

In a laser, the medium is placed inside a resonator with a cavity mode $E_C = \hbar\omega_C$, consisting of mirrors with reflectivity r_1 and r_2 at the two ends, respectively. Considering the gain cell fills up the whole length L of the resonator, and taking a look at the stationary solution ($\frac{\partial}{\partial t}I = 0$), one obtains the following condition for the threshold, at which the intensity is increased after one roundtrip:

$$r_1 r_2 \exp\left[2Lg\right] = 1. \tag{3.15}$$

In order to account for the losses through the mirrors, the rate equation for the intensity has to be modified . Therefore, the loss rate $-\frac{c}{2L}(1 - r_1 r_2)I$ has to be added on the right side of Eq. 3.12. The stationary solutions for $I(p)$ in dependence of the pump-rate p show a characteristic jump, when p reaches a value p_{th}, such that the threshold condition 3.15 is fulfilled [Fig. 3-2]. This jump in intensity is a result of the fact that the stimulated emission that becomes dominant for $p > p_{th}$ is channeled into the laser mode, while the spontanous emission that is dominant below threshold may also emit into other modes. For lasers, where a big fraction of the spontaneous emission is already emitted into the laser mode, the jump in $I(p)$ is less pronounced and may even vanish (thresholdless laser) [45, 46]. However, these kinds of lasers are not the subject of discussion here.

3.3 Semiconductor quantum dot gain

In semiconductors (SCs), one is no longer dealing with transitions between atomic energy states, but with interband transitions between conduction- and valence-band states. In case of indirect bandgap SCs, these transitions additionally involve momentum transfer, e.g. by phonon scattering [47]. In the following the discussion is focussing on direct bandgap SCs, such as GaAs and InAs, where the band-extrema of the conduction- and valence-band appear at the same point in momentum-space.

In SC nanostructures, a SC with a larger bandgap [e.g. GaAs], referred to as the barrier, is confining a SC with a smaller bandgap [e.g. InAs] in at least one dimension, within an extension of less than the charge carrier *de Broglie* wavelength [48]. A one dimensional sketch is shown in Fig. 3-1 (c). This leads to a quantization of the electron and hole energies in the confined direction. In SC quantum dots (QDs), the confinement appears in all three dimensions. Due to the 3D confinement their energy structure is similar to that of hydrogen, which is why they are sometimes referred to as artificial atoms [49]. Following this analogy, the energy levels in QDs are categorized in *s*-,*p*-,*d*-,... shells, according to their angular momentum ($l = 0, 1, 2, \dots$). The lowest allowed electron energy state and the highest allowed hole energy state build the QD ground state (*s*-shell).

The four-level scheme is a good approximation for lasers containing QDs as the gain medium. The off-resonant pumping creates carriers in the barrier material [similar to the higher energy transition $|0\rangle \rightarrow |3\rangle$]. Subsequently, the created electrons and holes relax into the QD ground state with energy E_{QD} [similar to the transition $|1\rangle \rightarrow |2\rangle$], which acts as the laser transition. Population inversion now depends on the occupation probability of the QD ground state by electrons and holes, described by fermi functions $f_{c,v}$.

In self-organized QD ensembles, the ground state energy E_{QD} varies between individual QDs, due to size and shape variations, resulting in an inhomogeneous broadening. Further, one has to take into account that QDs make up only a limited part of the total recombination volume, so that the normalized density of states per unit volume has the form [50]:

$$D(E_{QD}) = \frac{2}{V_{QD}} \frac{1}{\Delta E_{QD}\sqrt{2\pi}} \exp\left[-\frac{(E_{QD} - E_{QD,0})^2}{2\Delta E_{QD}^2}\right], \tag{3.16}$$

where V_{QD} is the average QD volume, and ΔE_{QD}, $E_{QD,0}$ are the width and maximum of the gaussian QD energy distribution, respectively. Finally, this leads to the QD gain function [50]

$$g_{QD}(E) = C\frac{1}{E}\int_{\infty}^{\infty} |M_b|^2 |M_{env}|^2 D(E') \left[f_c(E', E_{fc}) - f_v(E', E_{fv})\right] S_{QD}(E', E) dE', \tag{3.17}$$

wherein

$$S_{QD}(E_{QD}, E) = \frac{1}{\pi} \frac{\hbar\beta}{(E_{QD} - E)^2 + (\hbar\beta)}. \tag{3.18}$$

Here, $E = \hbar\omega$ is the photon energy, C is a constant, and M_b, M_{env} are the *Bloch*-matrix element and electron-hole wave function overlap, respecively, which are not

exactly known. Even though the specific form of $g_{QD}(E)$ is more complex than Eq. 3.13, the main characteristic is the same. It is still proportional to the number of excited QDs, i.e. the QD ground state population.
The homogeneous broadening S_{QD} is usually spectrally narrow compared to D and, thus, the gain spectrum is dominated by the inhomogeneous broadening of the density of states.

3.4 Planar semiconductor Bragg microcavities

Planar *Bragg* reflector microcavities (MCs) are excellent candidates for laser resonators, due to their small size and high quality factors. Their mirrors are built out of multilayers of pairs of semiconductors or dielectrics with alternating refractive indices n_1 and n_2. Their thickness is such that the optical path in each layer is the quarter of the target cavity wavelength λ_C, similar to the *Bragg* condition in X-ray analysis, which gives them the name distributed *Bragg* reflector (DBR).
The periodic structuring of n results in the formation of photonic stop-bands, centered around λ_C [51]. Propagating photons with wavelength lying in the stop-band, decay within the structure, resulting in a reflectivity close to 1, depending on the number of layer pairs and the refractive index contrast n_1/n_2. This is analogous to the formation of energy gaps in the bandstructure of electrons in a periodic crystal lattice. Due to this analogy such periodic structures are also referred to as 1D photonic crystals. The

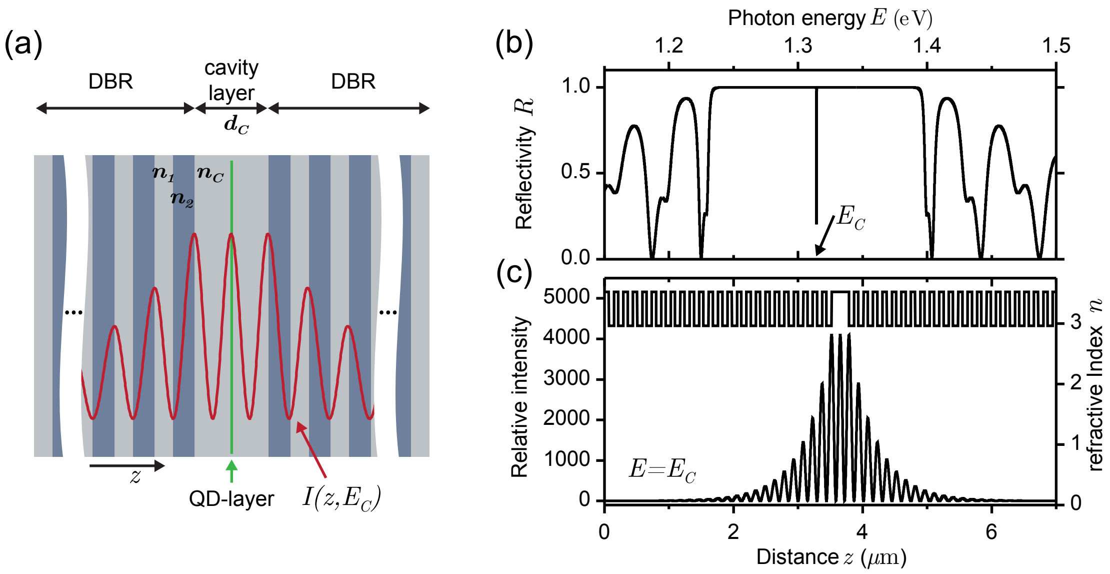

Figure 3-3: (a) Sketch of the layer structure of a planar bragg microcavity with a sheet of quantum dots in the center (green dotted line), where the cavity mode intensity field (red line) has a maximum. (b) Reflectivity spectrum $R(E)$ of an AlAs/GaAs microcavity with 27.5 (23) doublelayers in the bottom (top) distributed bragg reflector and $d_C = 268\,\text{nm}$ GaAs cavity-layer thickness. (c) Confined field intensity distribution of the cavity mode E_C in the same structure.

spectral width of the stop-band depends on the refractive index contrast n_1/n_2.
In a MC, two DBRs are sandwiching a cavity layer of thickness

$$d_C = j\frac{\lambda_C}{2n_C}, \quad (j = 1, 2, 3, ...) \tag{3.19}$$

as sketched in Fig. 3-3(a), where n_C is the refractive index of the cavity layer material. The cavity layer may be interpreted as a defect layer which breaks the periodic symmetry of a regular DBR structure [51]. This leads to localized photonic modes at such a defect, resulting in a distinct minimum in the reflectivity of the structure at the cavity mode energy $E_C = hc/\lambda_C$.
The *Maxwell* equations of multilayered dielectric structures may be conveniently solved using a transfer matrix formalism [52]. Thereby, it is possible to calculate the reflectivity spectrum $R(E)$ of a MC. An example is shown in Fig. 3-3(b), for a MC with a GaAs cavity layer of $\lambda_C/2$ optical thickness and 23 (27.5) AlAs/GaAs doublelayers at the top (bottom), and where the light is normal incident from the top. The stop-band extends over an energy range of $\sim 150\,\text{meV}$ and the cavity mode appears as a dip in the center at $E_C = 1.315\,\text{eV}$.
Due to the limited number of doublelayers, the reflectivity of the DBRs is less than unity and photons may escape after a certain lifetime τ. The limited lifetime leads to a broadening ΔE_C of the cavity mode. A measure for this is the quality factor

$$Q = \frac{E_C}{\Delta E_C}. \tag{3.20}$$

The field distribution of the cavity mode can be calculated, using the same transfer matrix formalism. It has the form of standing waves, like Fabry-Pérot modes that, however, penetrate into the DBR structure. The intensity profile $I(z, E_C)$ of the above mentioned structure is plotted in Fig. 3-3(c). To optimize the light-matter coupling, the gain medium has to be placed at an antinode of the field distribution. For example, a layer of InAs QDs may be placed at the center of a $\lambda_C/2$ cavity layer, as sketched in Fig. 3-3(a). The small gain volume in such a QD MC laser is compensated by the high Q factors >1000, which results in an increased interaction time with photons, before these escape the structure. On the other hand, small gain volumes require less pumping to invert the population and, therefore, lead to low lasing thresholds p_{th}.
One limiting factor that remains is the inhomogeneous linewidth ΔE_{QD} of a QD ensemble, which is usually much bigger than the linewidth ΔE_C of the MC. Consequently, only a small fraction of QDs can directly contribute to laser operation. A solution might be to dynamically shift the QD transition energies E_{QD}, such that a larger fraction of the gain spectrum is temporarily in resonance with the cavity mode. The overall laser emission intensity should be enhanced, if the modulation occurs faster than the thermal emission dynamics. A possible tool to shift the QD transition energies E_{QD} is strain. The underlying physics is explained in the following chapter 4.

4

Deformation potential

As was mentioned briefly in chapter 1, when calculating the electronic bandstructure in crystals, usually the *Born-Oppenheimer* approximation is applied, which allows to separate the electron and lattice motion, due to their difference in kinetic energy. However, the lowest order corrections to the complete separation of electron and lattice dynamics are only of the order $(m_e/M)^{1/4} \sim 10^{-1}$ to 10^{-2} [11]. Lattice vibrations, therefore, may lead to perturbative corrections of the electron energy levels, if they are strong enough. The *Schrödinger* equation, which describes the electron dynamics when lattice vibrations are present is given by [13]:

$$\left(H_e^0 + H_e'\right)\psi_e = i\hbar\frac{\partial}{\partial t}\psi_e, \tag{4.1}$$

where H_e^0 is the unperturbed electron Hamiltonian, and $H_e' = V(\boldsymbol{r}) - V_0(\boldsymbol{r})$ describes the variation of the unperturbed, periodic potential $V_0(\boldsymbol{r})$ due to a lattice displacement field $\boldsymbol{u}(\boldsymbol{r},t)$. Here, the treatment is restricted to sufficiently small phonon wavevectors $\boldsymbol{q}$, so that the displacement $\boldsymbol{u}(\boldsymbol{r},t)$ only varies slowly in space. In this case H_e' can be expanded with respect to $\boldsymbol{u}$ and its spatial derivative [13]. Only the linear terms shall be considered:

$$H_e' = \sum_\alpha u_\alpha V_\alpha' + \sum_{\alpha,\beta}\frac{1}{2}\frac{\partial u_\alpha}{\partial x_\beta}V_{\alpha\beta}'. \tag{4.2}$$

Here, $V_\alpha' = -\partial V_0/\partial x_\alpha$. The tensor $V_{\alpha\beta}'$ can be split into a symmetric and anti-symmetric part. The anti-symmetric part describes the variation of the potential due to a rotation of the crystal and can be neglected in first order. The symmetric part $V_{\alpha\beta}$ fulfills $V_{\alpha\beta} = V_{\beta\alpha}$, so that Eq. 4.2 becomes [13]:

$$H_e' = -\sum_\alpha u_\alpha\frac{\partial V_0}{\partial x_\alpha} + \sum_{\alpha,\beta}\eta_{\alpha\beta}V_{\alpha\beta}, \tag{4.3}$$

where $\eta_{\alpha\beta} = \frac{1}{2}(\partial u_\alpha/\partial x_\beta + \partial u_\beta/\partial x_\alpha)$ is the strain tensor, which was introduced earlier in Eq. 1.13. The *Schrödinger* equation 4.1 can be solved using H_e' in the form of Eq. 4.3, expanding the wavefunction ψ_e in a series of unperturbed functions $\psi_{n,\boldsymbol{k}_0}$ at an extremum $\boldsymbol{k}_0$ in momentum space [13, 53]. This way one is able to deduce the effect of a lattice deformation on the electronic band energies in the linear approximation for $\boldsymbol{k}$ in the vicinity of $\boldsymbol{k}_0$.

In the context of this work, it is sufficient to examine the effect of uniaxial strain $\eta_{33} = \eta$ in the (001)-direction of a crystal with zinc blende structure (e.g. GaAs, InAs). Of particular importance is the effect on the bandgap E_g at $\boldsymbol{k} = 0$. In the linear approximation, the involved conduction- and valence-band energies vary linearly with strain [54]. As a result, the bandgap energy change ΔE_g can be written as

$$\Delta E_g = a_d \eta. \tag{4.4}$$

The constant a_d is called deformation potential and usually has values $\sim -10\,\text{eV}$ for most semiconductors [55]. Picosecond strain pulses $\eta(z,t)$, as introduced in section 1.3, usually have amplitudes in the order $\eta_0 \sim 10^{-3}$, so that the electronic transition energies can be shifted by $\sim 10\,\text{meV}$ within picoseconds. The potential of this method has already been demonstrated in earlier works, targeting quantum well excitons (e.g. [26, 27, 28, 56, 57, 58]).

In this work, the same technique is applied to semiconductor quantum dots in order to shift the electronic transition energies E_{QD} and compensate initial detunings $E_C - E_{QD}$ in a microcavity laser. In the next chapter, the investigated microcavity laser will be introduced and characterized.

5

Quantum dot microcavity sample characteristics

The semiconductor (SC) laser under study consists of a planar microcavity (MC) grown by molecular beam epitaxy on a (001)-oriented GaAs substrate [see section 3.4 for an introduction to microcavities]. At the center of the cavity layer, where the electromagnetic field of the MC has an antinode, a layer of $\mathrm{In}_{0.3}\mathrm{Ga}_{0.7}\mathrm{As}$ quantum dots (QDs) has been placed as the gain medium [QD density $\sim 10^{10}\,\mathrm{cm}^{-2}$]. The QDs have been grown using the *Stranski-Krastanov* method [59]. Inherent to this method is a variation in size, shape and composition of the individual QDs in the ensemble, which translates into an inhomogeneous broadening of the electron transition energies E_{QD}. The optical field inside the MC is confined only perpendicular to the cavity plane, which means that the QD light emission to the side is unperturbed. The red curve in Fig. 5-1(a) shows the normalized photoluminescence spectrum, recorded from the cleaved edge of the sample at a temperature of $T = 10\,\mathrm{K}$ [section 2.1 for experimental details]. The off-resonant optical excitation was quasi-stationary at an energy of $E_{exc} = 2.33\,\mathrm{eV}$, with an excitation power density of $P = 10\,\mathrm{kW/cm}^2$, well below the lasing threshold P_{th}[1]. The spectrum corresponds to the QD ground state emission, centered at $E_{QD,0} = 1.351\,\mathrm{eV}$, with a spectral width of $\Delta E_{QD} = 11\,\mathrm{meV}$.

The distributed *Bragg* reflector (DBR) mirrors, sandwiching the cavity layer, are composed of alternating layers of AlAs and GaAs, each with $\lambda_C/4$ optical thickness, where λ_C is the MC resonance wavelength. In order to have a directional laser emission towards the surface side of the MC, the top DBR contains slightly less double-layers (23) than the bottom DBR (27.5), resulting in a slightly lower reflectivity of the top DBR mirror [51, 60]. The cavity layer is made out of GaAs and has an optical thickness

---

[1] Details about the lasing characteristics and particularly the lasing threshold will be provided later in this section.

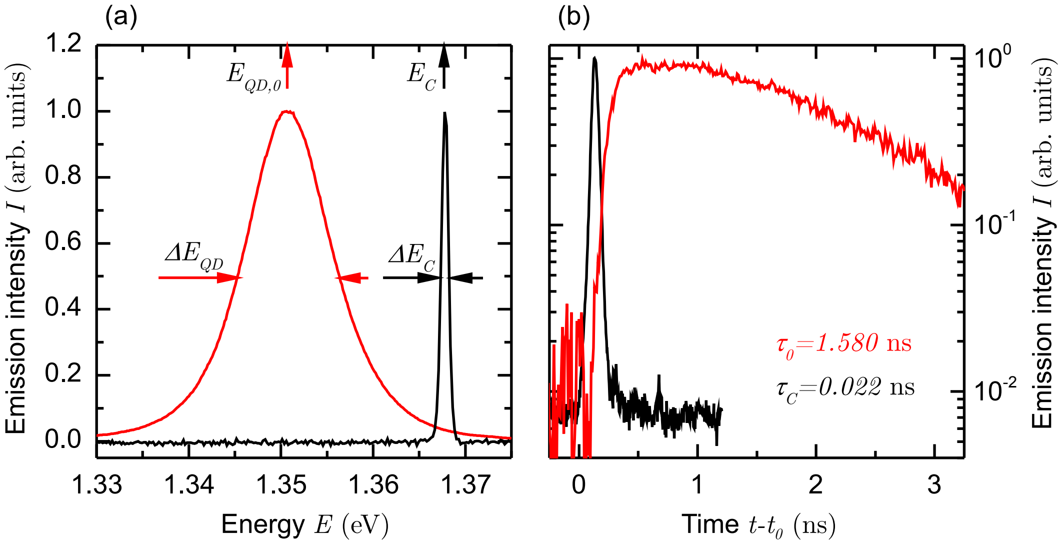

Figure 5-1: (a) Spectrum of the cavity mode emission at $E_C = 1.367\,\text{eV}$ with a full width at half maximum of $\Delta E_C = 1.2\,\text{meV}$ [black]. The quantum dot emission without cavity confinement was detected from the cleaved edge of the structure at a central energy of $E_{QD,0} = 1.351\,\text{eV}$ and with a width of $\Delta E_{QD} = 11\,\text{meV}$. (b) The quantum dot emission at $E = E_{QD,0}$ decays with a time constant of $\tau_0 = 1.580\,\text{ns}$. The cavity emission, when exciting above the lasing threshold, is dominated by stimulated emission and decays in just $\tau_C = 22\,\text{ps}$.

of λ_C. However, to ensure the tuneability of the fundamental cavity mode energy E_C, the cavity layer has a slight wedge, due to stopping the wafer rotation during the growth process. By changing the position on the sample, E_C can be varied from $E_C = 1.32 - 1.37\text{eV}$. The light emission to the front is concentrated in the cavity mode. The black curve in Fig. 5-1(a) shows the emission recorded from the front, in this case centered at $E_C = 1.367\text{eV}$, with a spectral width of $\Delta E_C = 1.2\text{meV}$, much smaller than the energy distribution ΔE_{QD} of the QD ensemble. Consequently, even if considering that QDs detuned by a few meV can couple to the cavity mode[61, 62, 63, 64, 65], it is only a small fraction of the total number of QDs, limiting the laser efficiency.

The dynamics of the cavity mode [QD] emission have been detected from the front [side], using a streak-camera with a temporal resolution of 25 ps [see section 2.1 for experimental details]. For the optical excitation, a pulsed laser with 150 fs pulse duration at $E_{exc} = 1.55$ eV was used. The excitation energy density $W = 70\ \mu\text{J/cm}^2$ was far above the lasing threshold. Under these conditions, the emission into the cavity mode is dominated by stimulated emission [chapter 3]. The recorded emission dynamics is plotted as the black curve in Fig. 5-1(b) and shows the decay with a timeconstant of just $\tau_C = 22$ ps [resolution limited]. As shown in Fig. 5-1(b), by the red curve, the emission of off-resonant QDs to the side decays in $\tau_0 = 1.580\text{ns}$ and does not contribute to lasing.

As discussed in section 3.2, the threshold excitation power density P_{th} depends on the material gain. Due to the high mode volume, the Purcell enhancement of the spontanous emission can be neglected in planar MCs [29, 66]. Further, the relative

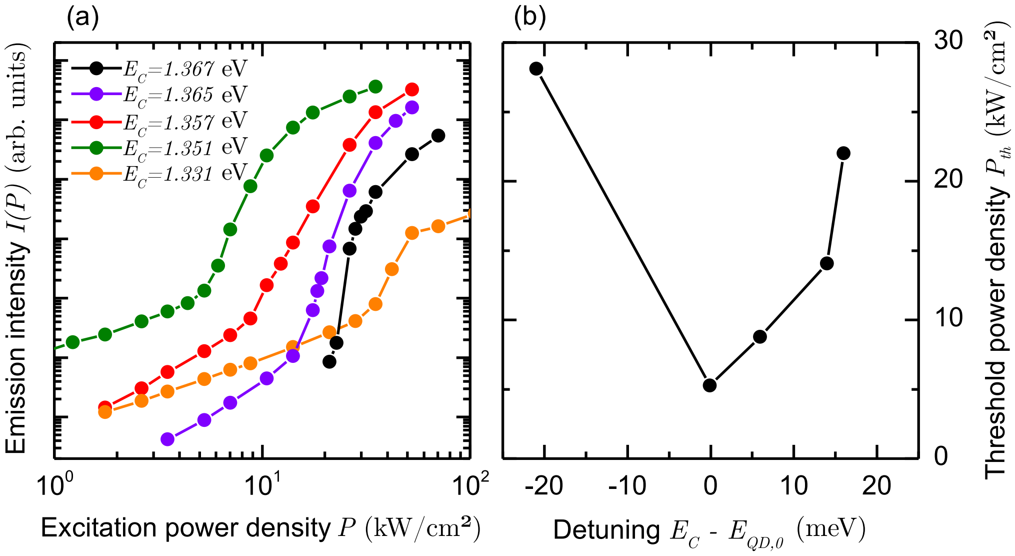

Figure 5-2: (a) Double-logarithmic input-output plots for stationary excitation with power density P, recorded for several different cavity mode energies E_C. (b) Lasing threshold power density P_{th}, associated with the first kink in the input-output plot, against the detuning $E_C - E_{QD,0}$ between cavity mode and QD central energy.

amount of spontaneous emission that is coupled into the cavity mode is negligible, so that the threshold P_{th} can be extracted from the excitation power density dependence of the cavity mode emission intensity $I(P)$ [input-output plot] [44, 45, 46]. Figure 5-2(a) shows this dependence for five different cavity mode energies E_C, recorded under quasi-stationary excitation [see section 2.1]. The threshold P_{th} is crossed at the first kink of $I(P)$, where the emission behaviour becomes non-linear. The dependence of P_{th} on the detuning is plotted in Fig. 5-2(b). The main observation here is that P_{th} is minimal, when the detuning $E_C - E_{QD,0}$ is zero. This agrees well with the fact that the QD gain spectrum $g_{QD}(E)$ has a maximum at $E_{QD,0}$, due to the density of states distribution $D(E)$ [Eq. 3.16,3.17]. Simply put, the threshold is lower the higher the number of resonant QDs.

Another remarkable observation is that the slope of $I(P)$, in the regime of spontanous emission, depends on detuning. For negative and zero detuning, the slope is identical, but for positive detunings, the slope becomes steeper. A possible interpretation might be based on the energy structure of QDs. As was stated in section 3.3, due to the electronic confinement, the energy of QDs is quantized [49]. The energy separation between s-shell and p-shell states is of the order $\sim$ 20 meV [measured in samples with similar QDs]. Due to the inhomogeneous broadening, there can be an overlap of s- and p-states, which are contributing to the positively detuned cavity mode emission. This might possibly explain the increased slope of $I(P)$.
There are, however, no p-shell features observerd in the recorded emission spectrum, even at pumping above the laser threshold. The reason might be that, for pump power densities $P < P_{th}$, the ground state occupation is not yet restricted by *Pauli*-blocking. For pumping above the threshold, the decay into the cavity mode might be so efficient,

due to stimulated emission, that *Pauli*-blocking remains unimportant.
Multi-exciton complexes may be another reason for the non-linear P dependence of I, in the spontaneous emission regime [67]. However, multi-exciton binding energies are small compared to the inhomogenous broadening ΔE_{QD} of the QD ensemble. Consequently, their influence on the spontaneous emission should appear on the negative energy wing of the distribution as well. Therefore, higher energy shells most likely play a more important role to describe the detuning dependence of $I(P)$ in the regime of spontaneous emission.

6

Laser mode feeding by shaking off-resonant quantum dots in a planar microcavity

In the previous section it was shown that the investigated microcavity laser suffers from an inefficient coupling of the spectrally broad quantum dot ensemble into the spectrally narrow cavity mode. It is desirable to increase the number of quantum dots which contribute to the laser emission and, thereby, improve the efficiency of the microlaser. One way is to achieve this dynamically, by shifting the transition energies of the QDs on timescales faster than the thermal emission dynamics. Lattice deformations result in shifts of the electronic transition energys [section 4] and strain pulses $\eta(t)$, generated by picosecond acoustics methods, may compensate energy detunings in the order of $\sim 10\,\mathrm{meV}$ within picoseconds (e.g. [26, 27, 28, 56, 57, 58]). In this chapter it will be shown that picosecond strain pulses are a prospective tool to dynamically increase the number of resonant QDs. Thereby, the emission output of the investigated microlaser is increased up to 50 times under stationary optical excitation, and by more than two orders of magnitude under pulsed excitation, if the cavity mode is detuned by $E_C - E_{QD,0} = 16\,\mathrm{meV}$. An analogy to this effect is the increased flow rate through a sieve, when giving it a shake.

6.1 Experimental conditions

The strongest effect of such dynamic modulation is expected to appear for a maximum increase of the gain and strong non-linear emission characteristics around the threshold P_{th}. The biggest increase of gain for the investigated microlaser is achieved when changing from a cavity detuning on the wings of the QD energy distribution towards zero detuning, as shown by the reduction of the lasing threshold P_{th} in Fig. 5-2(b).

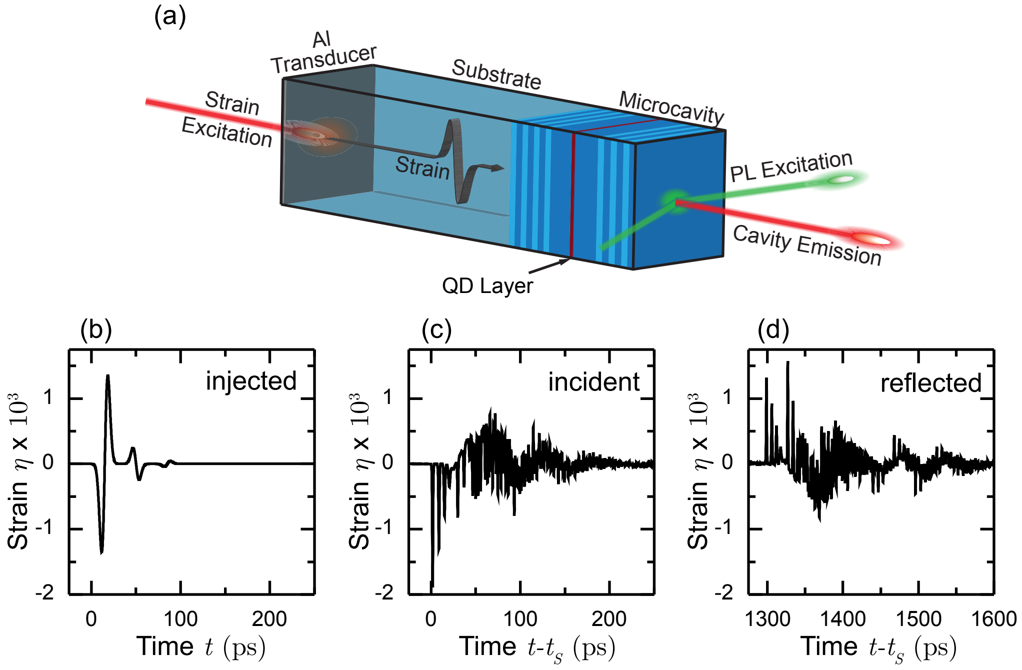

Figure 6-1: (a) Scheme of the shaking experiment. A strain pulse is optically excited at an Al transducer on the sample backside. The strain pulse propagates through the substrate and modulates the cavity emission, when it moves through the QD layer at the center of the cavity. (b)-(d) Calculated temporal dependence of the strain pulse $\eta(t)$ as it is injected into the substrate (b), when it hits the QD layer at t_S for the first time and once it has been reflected at the sample top with a π phase-shift and moves through the QD layer a second time (d).

Furthermore, the strongest increase in the emission intensity when crossing the lasing threshold is observed when the cavity is positively detuned, as shown in Fig. 5-2(a), by the black curve. As demonstrated in earlier works, the achievable energy shift by a strain pulse is in the order $\sim 10\,\mathrm{meV}$ [27], for typical semiconductor nanostructures. For the above mentioned reasons, the position on the sample is chosen such that the detuning is $E_C - E_0 = 16\,\mathrm{meV}$, for maximum intensity modulation. Subsequently, a detuning on the opposite side of the QD distribution, with $E_0 - E_C = -20\,\mathrm{meV}$, is investigated. In that case, only QD ground state emission is involved and an interpretation of the results is easier.

The scheme of the experiment is shown in Fig. 6-1(a), while details of the setup are explained in section 2.1. All experiments have been carried out at cryogenic temperatures [$T = 10$ K]. At the backside of the sample, a picosecond strain pulse is generated, using the established technique of picosecond acoustics [section 1]. For an excitation energy density of $W = 13\,\mathrm{mJ/cm^2}$,[1] the injected strain pulse $\eta(t)$ shows a temporal dependence as plotted in Fig. 6-1(b). The strain amplitudes are so high that elastic non-linearities become important during the propagation through the substrate

---

[1] The excitation energy density $W = 13\,\mathrm{mJ/cm^2}$ has been kept constant for all experiments in this chapter

[21]. Furthermore, during the propagation through the layered structure of the MC, multiple reflections modify the shape of the strain pulse. When it reaches the QD layer for the first time at t_S the temporal dependence $\eta(t)$ looks like shown in Fig. 6-1(c). Subsequently, the strain pulse propagates through the top DBR, is reflected at the MC open surface with a π phase shift and reaches the QD layer for a second time, about 1.3 ns later [see Fig. 6-1(d)].

In the next section, at first the effect of shaking on the emission intensity $I(t)$, when the cavity mode is positively detuned by $E_C - E_{QD,0} = 16\,\mathrm{meV}$, will be investigated. In section 6.3, the same experiment will be performed, for a detuning on the opposite side of the QD energy distribution, at $E_C - E_{QD,0} = -20\,\mathrm{meV}$.

6.2 Shaking at positive detuning

In this section, the results of the shaking experiment, at a detuning of $E_C - E_{QD,0} = 16\,\mathrm{meV}$, will be presented. The effect of the strain pulse perturbation on the emission intensity $I(t)$ is studied in the time domain. At first, the microlaser is optically excited under quasi-stationary conditions, at $E_{exc} = 2.33\,\mathrm{eV}$. Thereafter, the effect for pulsed optical excitation with $E_{exc} = 1.55\,\mathrm{eV}$ will be presented.

Figure 6-2(a) shows the emission intensity $I(t)/I_0$ over a time interval of 1.8 ns for an excitation power density $P = 0.9P_{th}$, normalized to the value I_0 of stationary emission without shaking. Two intensity peaks, separated by 1.3 ns, are clearly observed. The time separation equals the separation between incident and reflected strain pulse

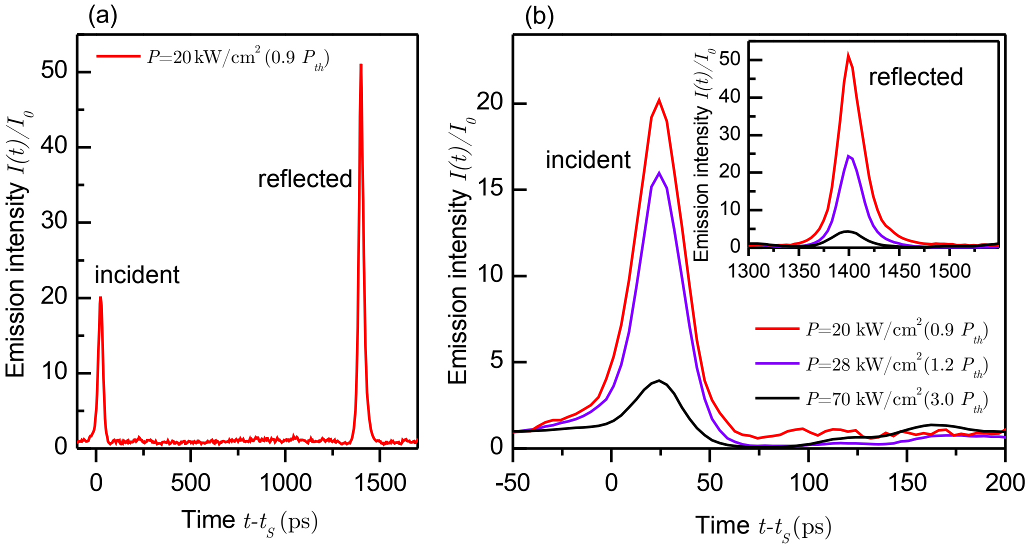

Figure 6-2: (a) Normalized change of cavity mode emission intensity $I(t)/I_0$ due to the incident and reflected strain pulses. Stationary optical excitation conditions just below the lasing threshold [$P = 0.9P_{th}$]. (b) More detailed look at the emission change $I(t)/I_0$ due to the incident strain pulse [Inset: reflected strain pulse], recorded for different optical excitation densities P, below and above the threshold P_{th}.

[Fig. 6-1(c),(d)], which indicates that they are indeed responsible for the modulation. Each peak has a duration of just a few 10 picoseconds. The first one amounts to an emission intensity increase by a factor of 20, while the reflected pulse increases the emission intensity even 50 times.
In the inset of Fig. 6-2(b) a more detailed plot is shown for the incident and reflected pulse, using various excitation power densities P. The strongest increase is observed for excitation densities slightly below the lasing threshold, but even for operation well above the threshold, at $P = 3.0P_{th}$, the intensity is still increased several times.
Above the lasing threshold, not only an increase of emission is observed, but also a decrease up to total quenching in the time interval from $t - t_S = 50 - 100\,\text{ps}$. But still, when integrating over the duration of each pulse a net intensity increase is observed. The origin of the quenching will be discussed later.

If the optical excitation of the microlaser is changed to be pulsed, the effects become even stronger. However, the time separation $t_S - t_0$ between microlaser excitation at t_0 and the strain pulse arrival time at the QD layer t_S is an additional parameter that has to be taken into consideration. As can be seen in Fig. 6-3, this separation has a significant influence on the emission dynamics of the microlaser. The energy density per pulse $W = 1.1W_{th}$, used in this example, is above the lasing threshold of $W_{th} = 5.2\ \mu\text{J/cm}^2$ [see Fig. 6-4(a)]. The black curves in Fig. 6-3 show the emission dynamics without any strain pulse perturbation. The emission intensity $I(t)$ reaches its maximum I_0 around 100 ps after the optical excitation, followed by a rapid decay with a timeconstant of τ_c, governed by the lasing kinetics [Fig. 5-1(b)]. The red curves show the time dependence of $I(t)/I_0$ with applied strain pulse, for two different

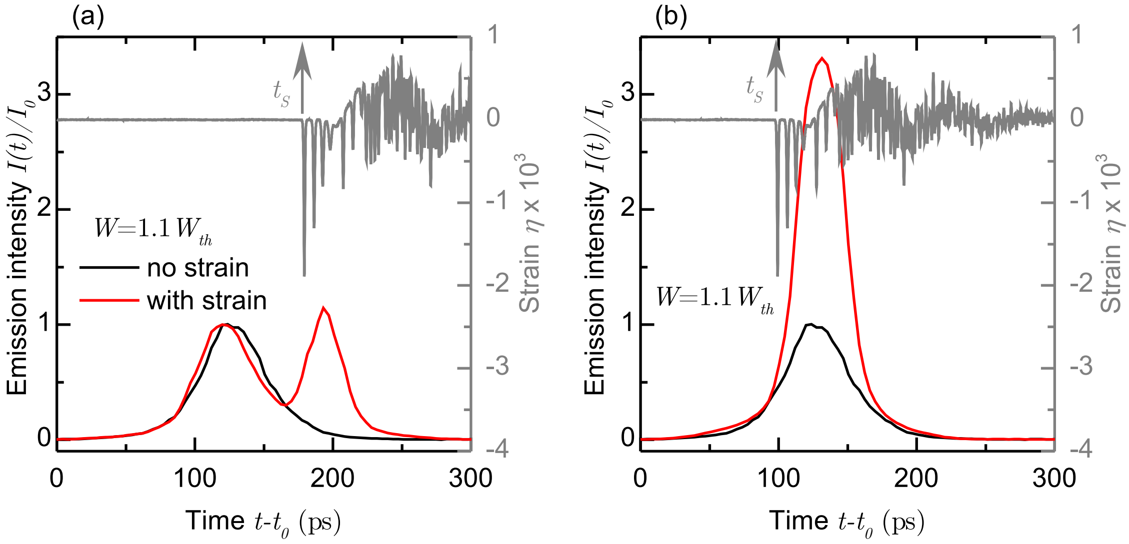

Figure 6-3: Change of cavity mode emission intensity $I(t)/I_0$ after pulsed optical excitation with an energy density $W = 1.1W_{th}$. The black curve shows the unperturbed emission after excitation at t_0. The red curves shows the emission intensity changes for two different arrival times t_S of the incident strain pulse [grey trace] at the quantum dot layer. (a) $t_S - t_0 = 180\text{ps}$, (b) $t_S - t_0 = 100\ \text{ps}$.

values of $t_S - t_0$ in (a) and (b), respectively. Figure 6-3(a) shows the case where the strain pulse arrives when the emission is already decaying [$t_S - t_0 = 180\,\mathrm{ps}$]. For this timing, $I(t)/I_0$ increases again for the time interval when the strain pulse has mainly compressive components [grey trace in Fig. 6-3]. The maximum increase is achieved when $t_0 - t_S$ is chosen in such a way that the compressive strain pulse front is moving through the QD layer while the unperturbed emission would reach its maximum. This is the case for $t_S - t_0 = 100\,\mathrm{ps}$, as shown in Fig. 6-3(b).
The latter case shall be investigated further, depending on the excitation energy density W. As for stationary excitation, the strength of the effect is maximal when exciting just at the threshold W_{th}. For excitation above the threshold, at $W = 1.1W_{th}$, the intensity $I(t)/I_0$ is increased already a few times, as seen in Fig. 6-3(b). However, when exciting at $W = 1.0W_{th}$, the intensity is increased by more than two orders of magnitude [Fig. 6-4(b)]! If the increase is compared with the non-linear jump of $I(W)$ in the input-output plot when crossing W_{th} [see Fig. 6-4(a)], the strain induced intensity increase has a similar magnitude. This indicates that by shaking the device during optical excitation at $W = W_{th}$, the microlaser can be dynamically switched from spontaneous to lasing emission.

To give a qualitative explanation for the observed emission modulation $I(t)/I_0$, for quasi-stationary and also pulsed optical excitation, one has to discuss three different excitation regimes.
(i) $P \ll P_{th}$: In the regime of spontaneous emission, the cavity emission intensity is directly proportional to the number of excited QDs [Eq. 3.8]. The compressive part of the strain pulse $\eta(t)$ shifts the maximum of the QD energy distribution towards the

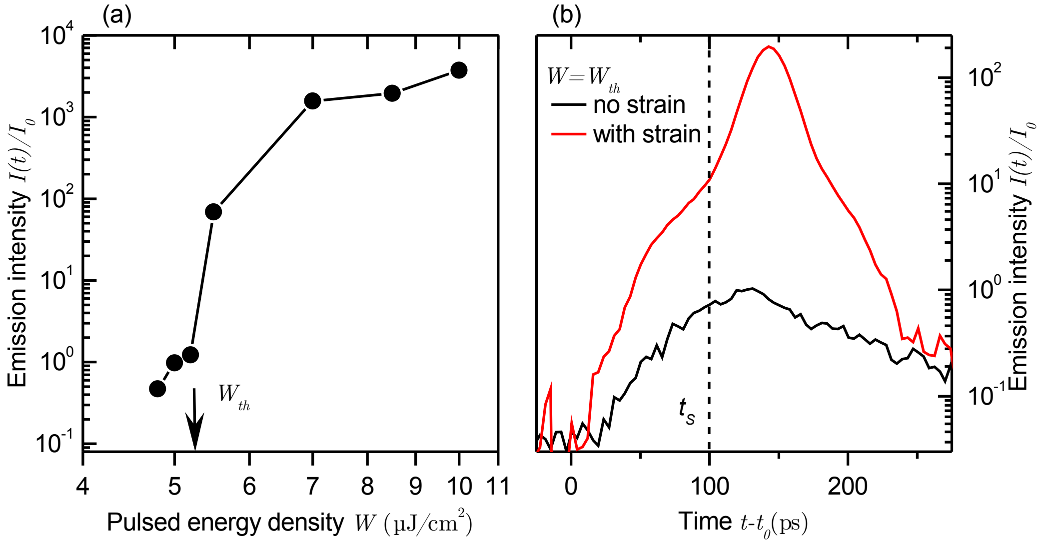

Figure 6-4: (a) Input-output plot $I(W)$ for pulsed optical excitation. (b) Cavity mode emission danymics $I(t)/I_0$, with [red] and without strain [black], when excited just at the lasing threshold $W = W_{th}$. The strain pulse moves through the QD layer at the time t_S, 100 ps after the optical excitation at t_0. Shaking results in an intensity increase of two orders of magnitude.

cavity mode, which temporarily increases the number of resonant QDs. The intensity increase $I(t)/I_0$ should be moderate, proportional to the increase of quasi-resonant QDs.
(ii) $P \approx P_{th}$: The excitation regime around the lasing threshold shows highly non-linear emission intensity behaviour. A shift of the quantum dot gain spectrum [Eq. 3.17] towards the cavity mode E_C temporarily results in a higher gain for the microlaser, which may be enough to dynamically exceed the lasing threshold [Eq. 3.15]. As a consequence, the emission intensity increases drastically, because quasi-resonant QDs are now dominantly emitting into the cavity mode due to stimulated emission, as seen in Figs. 6-2 and 6-4 for stationary and pulsed excitation, respectively.
(iii) $P > P_{th}$: In the lasing regime, the decay of resonant QDs is significantly faster compared to off-resonant QDs [Fig. 5-1(b)]. Consequently, the equilibrium population of resonant QDs is decreased, due to stimulated emission. In other words, the laser emission burns a spectral hole into the QD population, within the spectral width for which the emission can be fed into the cavity mode. The strain pulse $\eta(t)$ temporarily increases the number of QDs that can feed the laser mode, which broadens the width of the spectral hole and results in a higher emission intensity. As for the spontaneous emission regime, however, the emission increase directly depends on the number of quasi-resonant QDs and thus is only moderate.

The strain induced shift of the electronic transition energies in the QD ensemble is the dominant contribution to the emission modulation $I(t)/I_0$. Another contribution is the shift of the cavity mode energy E_C [68]. Interface displacements inside the DBR structure and a strain induced change of the refractive index n of the individual DBR layers, due to the photo-elastic effect, result in a change of E_C when the strain pulse propagates through the MC. This change of E_C appears even before the strain pulse reaches the QD layer and is of the order ~ 0.1 meV, much smaller than the shift of E_{QD}. The small shift of E_C is, however, large enough to have a noticable effect on $I(t)/I_0$, if the microlaser is operated in the highly non-linear excitation regime around the lasing threshold. In this case an emission increase is already observed around 50 ps, before the strain pulse reaches the QD layer, as can be seen in Fig. 6-2(b) and Fig. 6-4(b).

A quantitative description of the discussed effects is difficult for a number of reasons. First of all, solving the coupled set of non-linear differential equations for population and field intensity, introduced in chapter 3, is a non-trivial task of its own, even for a simple two-level system. On top of this, it was already mentioned in chapter 5 that for positive detuning it seems like not only the QD ground state emission is fed into the cavity mode, but higher states are involved, too.

To get at least a qualitative understanding of the observed effects, in the next section, results for a cavity detuning of $E_C - E_{QD,0} = -20$ meV will be shown. In that case, only QD ground state emission is involved. Calculations based on a simplified rate-equation approach will be presented to proof the qualitative explanation for the lasing regime given in this section.

6.3 Shaking at negative detuning

In this section, the shaking experiment, presented in section 6.2, will be repeated for a negative cavity mode detuning of $E_C - E_{QD,0} = -20\,\mathrm{meV}$ [Fig. 6-5(a)]. Unlike for positive detuning, only QD ground state emission is fed into the cavity mode in this case. This allows the application of a simplified rate-equation model. Comparison of calculations and experimental results will help to understand the mechanism that is responsible for the emission intensity modulation $I(t)/I_0$ in greater detail than it was possible in section 6.2.

The normalized emission intensity $I(t)/I_0$ under quasi-stationary excitation, at $P = 4.0P_{th}$, clearly in the lasing regime, is plotted in Fig. 6-5(b). The strain pulse was excited with an excitation energy density of $W = 13\,\mathrm{mJ/cm^2}$, the same as in the previous experiments in section 6.2. Again, one detects two emission intensity peaks, separated by 1.3 ns, which correspond to the incident and reflected strain pulse perturbation, respectively.

For the incident strain pulse, a decrease of emission intensity is observed, before the emission is increased by a factor of ~ 2. Comparing this behaviour with the previous experiments at positive detuning [Fig. 6-2(b)], increase and decrease of emission appear in opposite order. This is a result of the opposite detuning. For negative detuning, the compressive components at the leading edge of the strain pulse $\eta(t)$ shift the maximum of the QD distribution, at $E_{QD,0}$, away from the cavity mode E_C, resulting in an initial emission decrease.

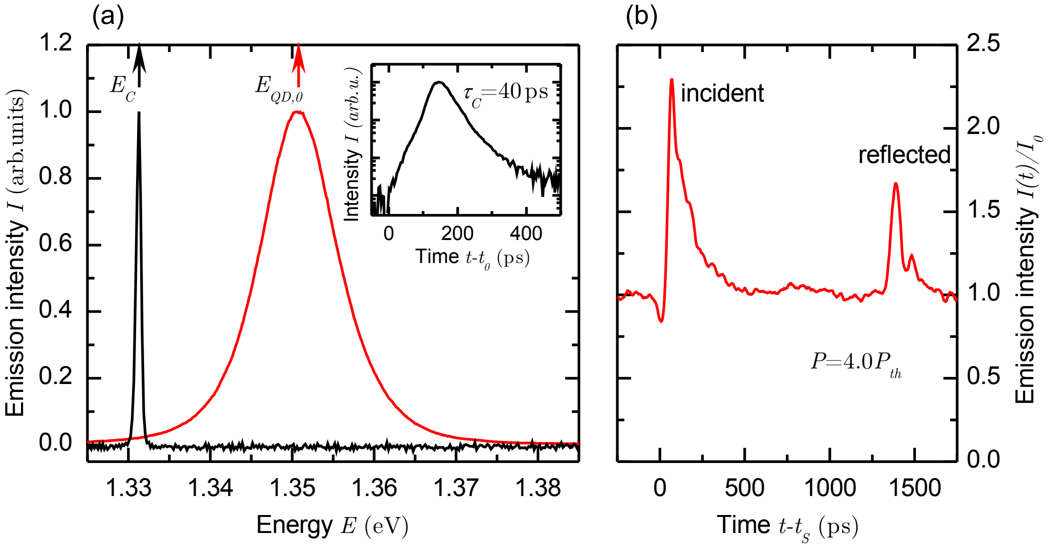

Figure 6-5: (a) Spectrum of the cavity mode emission at $E_C = 1.331\,\mathrm{eV}$ with a spectral width of $\Delta E_C = 1.0\,\mathrm{meV}$ [black]. Quantum dot emission at $E_{QD,0} = 1.351\,\mathrm{eV}$ central energy, with an inhomogeneous broadening of $\Delta E_{QD} = 11$ meV [red]. The cavity emssion in the lasing regime decays with a time constant of $\tau_C = 40\,\mathrm{ps}$ [inset]. (b) Cavity emission intensity change $I(t)/I_0$, due to the incident and reflected strain pulse, at $t - t_S = 0$ and $t - t_S = 1.3\,\mathrm{ns}$, respectively. The optical excitation was quasi-stationary with a power density of $P = 4.0P_{th}$.

The emission increase lasts over a time of ~ 100 ps, much longer than for positive detuning. Apart from the duration, the results are also less promising for applications, because the magnitude of the increase is smaller than for positive detuning. However, the results are still appealing, because the fact that only QD ground state emission is fed into the laser mode makes it possible to analyse them on a more quantitative level and one may draw general conclusions.

In the following, a new model is introduced, which is strongly simplified compared to the theory presented in chapter 3. It is assumed that the microlaser is operated in the lasing regime. Further, only the population probability $N(E,t)$ of the QD ground state is taken into acount. The pumping process is included by a phenomenologic generation rate $g(t)$, so that the time evolution of $N(E,t)$ is described by the differential equation

$$\frac{d}{dt}N(E,t) = -[\Gamma_C(E,t) + \tau_0^{-1}]N(E,t) + g(t). \tag{6.1}$$

Quantum dots with a ground state energy E_{QD} in the vicinity of the cavity mode E_C decay at an increased rate $\Gamma_C(E,t)$, due to stimulated emission:

$$\Gamma_C(E,t) = \frac{1}{\tau_C}\left[1 + \left(\frac{E(t) - E_C}{\Delta\Gamma_C}\right)^2\right]^{-1}. \tag{6.2}$$

The strain pulse $\eta(t)$ shifts the energy E_{QD} of the individual QDs, as described in chapter 4, resulting in a time dependent electronic transition energy

$$E(t) = E_{QD} + a_d \cdot \eta(t), \tag{6.3}$$

where a_d is the deformation potential [Eq. 4.4]. Combining Eqs. 6.2 and 6.3 into Eq. 6.1, the time dependence of the population probability $N(E,t)$ can be calculated. In the end, the time dependence of the emission intensity $I(t)$ is of interest. For a set energy E, it is given by the decay rate into the cavity mode times the population probability $N(E,t)$, weighted by the density of states $D(E_{QD})$. The total emission intensity $I(t)$ amounts to the integral over all energies

$$I(t) = \int_{-\infty}^{\infty} \Gamma_C(E,t) \cdot N(E,t) \cdot D(E_{QD}) dE_{QD}. \tag{6.4}$$

Finally, at each point in time, the calculated intensity $I(t)$ has to be averaged over a timerange of $\Delta t = 25$ ps, to take into account the experimental time resolution.

The temporal dependence of the strain pulse $\eta(t)$, used for the calculation, is plotted once again in Fig. 6-6(a). The black curve in Fig. 6-6(b) shows the calculated emission intensity $I(t)/I_0$, where the set of parameters was taken from the experiment[1].
Experimental results for quasi-stationary excitation at $P = 4P_{th}$, already shown in Fig. 6-5(b), are plotted into the same figure [red curve]. The calculated peak emission increase is about 2.5 times bigger than in the experiment, but still of the same order

---

[1] $\tau_0 = 1.5$ ns, $\tau_C = 40$ ps, $\Delta\Gamma_C = h/\tau_C = 0.1$ meV, $E_C = 1.331$ eV, and $a_d = -10$ eV. For the density of states $D(E_{QD})$, the measured spectrum, shown in Fig. 6-5(a) is used

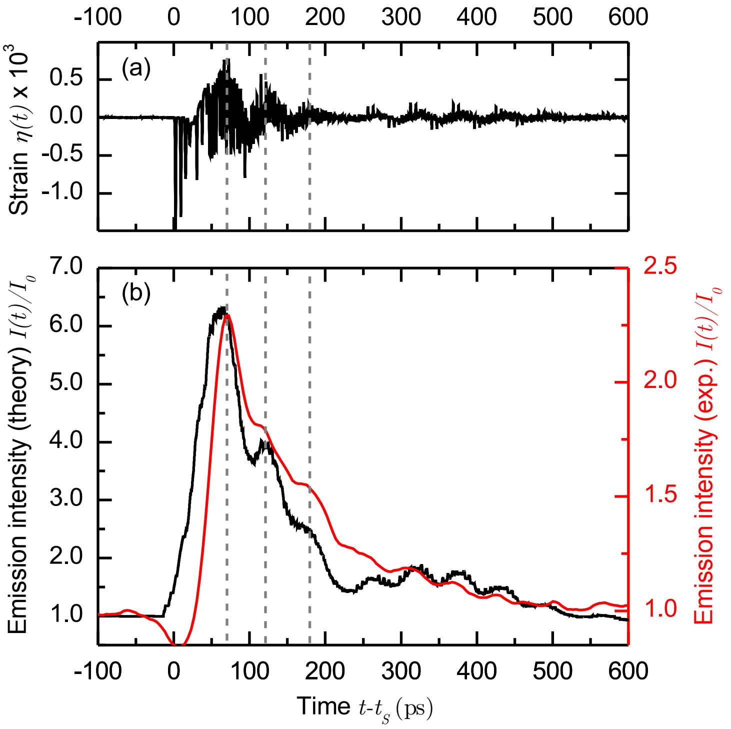

Figure 6-6: (a) Temporal dependence of the incident strain pulse $\eta(t)$ at the QD layer. (b) Emission intensity change $I(t)/I_0$ due to the perturbation of the incident strain pulse. The red curve shows the experimental result for quasi-stationary excitation at $P = 4.0P_{th}$. The black curve shows a calculation, based on the simplified rate equation model, introduced in this section [$\tau_0 = 1.5\,\text{ns}$, $\tau_C = 40$ ps, $\Delta\Gamma_C = h/\tau_C = 0.1$ meV, $E_C = 1.331$ eV, $a_d = -10$ eV, and $D(E_{QD})$ taken from the spectrum in Fig. 6-5(a)]. The dashed vertical lines are guides to the eye, highlighting some points in time with maximum tensile strain at the QD layer.

of magnitude. For better comparison, the plots for theory and experiment are scaled to the same amplitude [left y-axis: theory, right y-axis: experiment].

Despite the missing drop at the leading edge, the calculated temporal evolution of the cavity emission intensity $I(t)/I_0$ shows remarkable congruency with the experimental results, even in detail. In particular, local maxima of the intensity appear at the same points in time. For illustration, the first three local maxima have been highlighted by dashed vertical lines in Fig. 6-6. Comparing (a) and (b), these maxima correspond to points in time, where the strain $\eta(t)$ is dominantly tensile. This agrees well with the previous assumption that the emission intensity increases when the maximum $E_{QD,0}$ of the gain spectrum is shifted towards the cavity mode E_C [Eq. 6.3].

The good agreement between theory and experiment suggests to have a deeper look into the mechanism that is responsible for the emission intensity increase. Therefore, the population $N(E,t) \cdot D(E_{QD})$ for the unperturbed equilibrium at $t - t_S = -50$ ps [black] and at the time of the intensity maximum at $t - t_S = 70$ ps [red] are plotted in Fig. 6-7. The equilibrium population [$t - t_S = -50$ ps] shows a spectral hole at $E_C = 1.331$ eV, due to the increased decay rate Γ_C, associated with stimulated emission into the laser mode. The width ~ 1 meV of the spectral hole agrees well with the measured linewidth ΔE_C of the cavity mode in the emission spectrum, shown in Fig. 6-5(a).

To understand Fig. 6-7, it has to be stressed that, in the applied model, the energy modulation is applied to Γ_C. This equals a modulation of the cavity mode rather than the QD transition energies, so that $D(E_{QD})$ is fix. However, this is just a technical difference. At $t - t_S = 70$ ps, the dominantly tensile parts of the strain pulse have

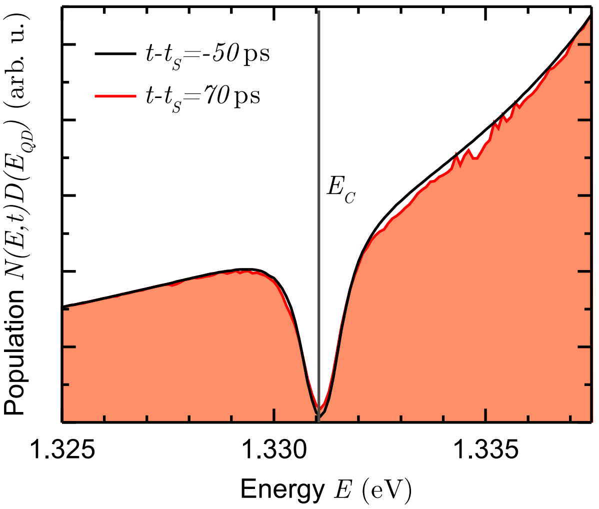

Figure 6-7: Calculated population $N(E,t)\cdot D(E_{QD})$ at two different times. $t-t_S=-50$ ps [black]: Equilibrium population, without strain pulse perturbation. $t-t_S=70$ ps [red]: Population at the time of maximum emission intensity $I(t)/I_0$. During shaking, the spectral hole of the equilibrium population is broadened over the energy modulation window of ~ 10 meV.

shaken the QDs, such that an energy window of ~ 10 meV, closer to the maximum of the distribution $D(E_{QD})$, was temporarily in resonance with the cavity mode. Figure 6-7 shows: the population within the energy modulation window has decreased, due to the contribution to laser emission with the rate of stimulated emission $\tau_c^{-1} \gg \tau_0^{-1}$. This supports the interpretation for the excitation regime (iii) $P > P_{th}$, in section 6.2, where it was assumed that the emission intensity increase is due to the fact that shaking broadens the spectral hole over the modulation range. The frequency components in the strain pulse, however, are even higher than τ_C^{-1}, up to several 100 GHz [Fig. 1-3], so that the dynamic coupling of quasi-resonant QDs is not efficient enough to burn a spectral hole as deep as the one at E_C in the equilibrium population.
After reflection, the solitons at the strain pulse front become tensile, due to a π-phase shift. Quantum dots shifted into resonance by them probably suffer from an even lower coupling efficiency, because solitons carry the highest frequency components within the pulse. This might be an explanation for the lower peak amplitude of $I(t)/I_0$ for the reflected strain pulse [Fig. 6-5(b)]. The argument is supported by the fact that the opposite behaviour is observed for positive detuning [Fig. 6-2], where the roles of compressive and tensile strain are switched. There, the maximum amplitude of $I(t)/I_C$ is observed for the reflected strain pulse.

6.4 Conclusion and perspective

In conclusion of this chapter, using picosecond acoustics, it has been demonstrated that, by shaking a quantum dot microcavity laser, where a large portion of quantum dots is originally out of resonance, it is possible to drastically increase the emission intensity. For a cavity detuning of 16 meV towards the high energy flank of the inhomogenious quantum dot ensemble, an emission intensity increase by a factor of 50 under stationary optical excitation, or even by two orders of magnitude in case of pulsed optical excitation has been observed. The responsible mechanism is the strain induced modulation of the electronic transition energies, to obtain resonance with the cavity mode, faster than the spontaneous emission dynamics.

Going a step further, the method may be used to dynamically achieve resonance between electronic transitions and an optical cavity mode, especially in systems, where such resonance conditions are challenging or even impossible to achieve by the manufacturing process itself. The self-evident application would be to create high-efficiency quantum dot lasers. Population inversion in such lasers may be achieved efficiently for off-resonance, e.g. by electrical pumping, and shaking is used to open the stimulated emission channel.
Another example would be single- or entangled-photon emission in single quantum dot microcavities. An originally off-resonant quantum dot could be dynamically pushed into resonance to trigger the emission of single photons on demand.

Especially appealing in the context of prospective applications, is the development of terahertz sasers[1], as a shaker which can be electronically controlled. First promising results have been reported recently [69], based on GaAs/AlAs superlattices, controlled by an applied electrical bias. Combined with a microlaser, such sasers could lead to the realisation of electrically controlled on-chip solutions of above mentioned devices.

In a more traditional approach, the technique may be used to modulate light sources at ~ 10GHz, comparable to the current limit for such modulation. The common way to achieve this in modern devices is by changing the cavity resonance or its quality factor Q [Eq. 3.20]. To apply such methods to microlasers with dimensions on the order of the emission wavelength, however, is a challenging task [70, 71], so that external modulators need to be used. Using picosecond acoustics to modulate the gain medium instead, is a prospective method to achieve even higher modulation frequencies.
One possible way to achieve higher modulation frequencies is to tailor the system specifications such that only short parts of the strain pulse have an effective influence. For example, the detuning could be chosen to be such that only those parts with the highest strain amplitude are able to create the resonance condition. The high-amplitude solitons at the strain pulse front have durations of only a few picoseconds, resulting in sub-terahertz modulation frequencies.
The more versatile method would be to modify the shape of the strain pulse, because it could be applied to any device. The active approach would be to replace the acousto-optic transducer, so that the excited strain pulse is shorter, or even monochromatic. The latter can be achieved, using superlattices as the transducer [72]. Pulse-shaping may also be done passively, e.g. using acoustic nanocavities [73, 74]. Such structures may either be used to filter certain frequencies of a broadband strain pulse, or even to enhance the field-amplitude of frequency components corresponding to the acoustic cavity mode.

The speed of sound contrast of GaAs and AlAs turns the optical DBR mirror itself into a phonon filter already. In the next section, it will be shown that the pulse shaping by the microcavity DBR structure allows for a harmonic GHz modulation of the microlaser output intensity.

---

[1] Sasers are the acoustical analogue of lasers.

7

Harmonic modulation of laser emission in a hybrid optical/acoustical microcavity

It happens that the refractive index n and the speed of sound v reciprocally have the same relative contrast in GaAs/AlAs heterostructures: $n_{AlAs}/n_{GaAs} \approx v_{GaAs}/v_{AlAs} \approx 0.84$ [75]. Consequently, the optical *Bragg* mirror of a planar microcavity, like the one introduced in chapter 5, at the same time corresponds to an acoustical mirror [76]. As a result, it acts as a filter for an incoming acoustic broadband pulse. Phonons with certain frequencies have an increased transit time through the structure. In this chapter it will be shown that after the initial strain pulse perturbance, such delayed phonons are able to modulate the laser emission intensity at a set frequency of 17 GHz. In the planar quantum dot microcavity laser under investigation, such modulation is the most effective for zero detuning, $E_C - E_{QD,0} = 0$.

7.1 Experimental conditions

The microlaser under study is the planar quantum dot (QD) microcavity (MC) introduced in chapter 5. The experimental conditions are identical to those described in section 6.1. A picosecond strain pulse $\eta(t)$ is excited on the backside of the sample, using the established technique of picosecond acoustics, introduced in chapter 1. The strain pulse shifts the electronic transition energies of an inhomogeneous QD ensemble and, thereby, perturbes the coupling to the cavity mode at E_C. The effect on the emission intensity $I(t)$ of the microlaser is investigated in the time domain.
This time, the cavity detuning with respect to the maximum of the QD energy distribution is zero, $E_C - E_{QD,0} = 0$. All experiments are performed at cryogenic temperatures [$T = 10\,\mathrm{K}$].

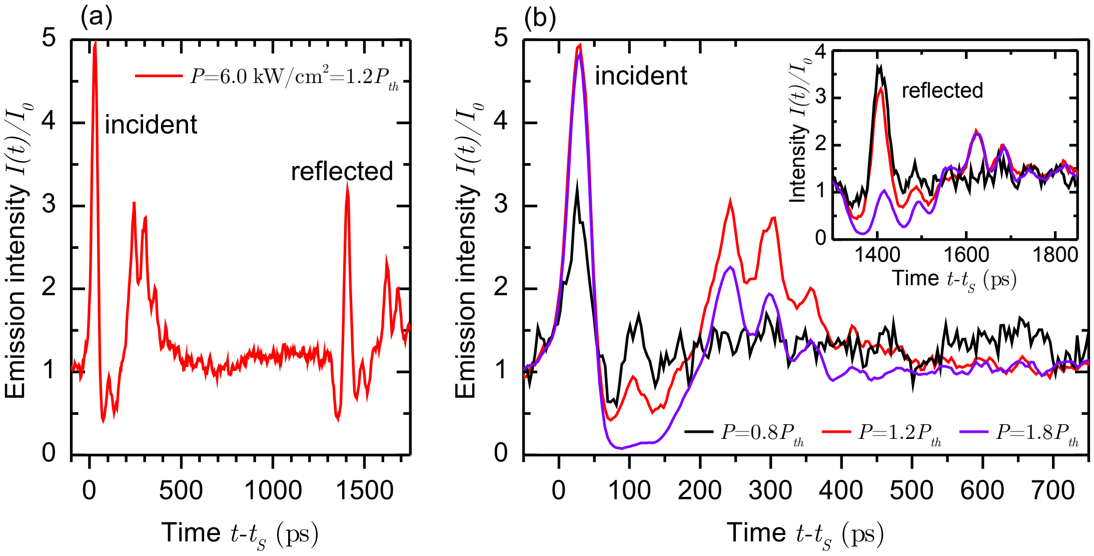

Figure 7-1: (a) Normalized change of cavity mode emission intensity $I(t)/I_0$ due to the incident and reflected strain pulses. Stationary optical excitation conditions at the lasing threshold [$P = P_{th} = 5.2\,\mathrm{kW/cm}^2$] for zero cavity detuning. (b) More detailed look at the emission change $I(t)/I_0$ due to the incident strain pulse [inset: reflected strain pulse], recorded for different optical excitation densities P, below and above the threshold P_{th}.

Figure 7-1(a) shows the emission intensity $I(t)/I_0$, recorded under quasi-stationary excitation, at $P = 1.2P_{th}$, just above the threshold power density of $P_{th} = 5.2\,\mathrm{kW/cm}^2$. The effect of the incident and reflected strain pulse is detected with a separation of 1.3 ns, as already noted in chapter 6, and in agreement with strain pulse calculations [Fig. 6-1(c),(d)]. A more detailed view is shown in Fig. 7-1(b), for different excitation power densities P.
The effect of the leading part of the strain pulse has already been subject of detailed discussion in chapter 6. Remarkable for the zero detuning conditions is the distinct harmonic modulation of $I(t)/I_0$ with a frequency of 17 GHz, following the initial perturbance, at times $t - t_S > 200$ ps. It is, however, superimposed on a slowly varying background. The strongest effect is achieved for an excitation power density just above the threshold, at $P = 1.2P_{th}$, where the 17 GHz oscillation has an amplitude of ~ 50 %. But even in the lasing regime the harmonic modulation is still very distinct. In the excitation regime below the lasing threshold, the modulation is undistinguishable from noise.

7.2 Harmonic intensity modulation by phonon filtering in acoustic superlattices

Before the observed experimental results are analyzed, it is necessary to understand a few things about phonon dynamics in an acoustic superlattice (SL), i.e. heterostructures with a periodic profile of the acoustic impedance Z. Elastic waves have to satisfy continuity conditions for the atomic displacement u and stress σ [section 1.2], in particular at the interface of two materials A and B. In a superlattice with a periodic impedance profile in the z-direction, the boundary conditions for an interface at $z = z_0$ read [76]:

$$\begin{aligned} u(z_0)|_A &= u(z_0)|_B\,, \\ C_A \frac{\partial u(z_0)}{\partial z}\bigg|_A &= C_B\,\frac{\partial u(z_0)}{\partial z}\bigg|_B\,, \end{aligned} \tag{7.1}$$

where C_j is the elastic force constant in material $j = A, B$. Analogous to solving *Maxwell*'s equations in multilayered structures, Eqs. 7.1 can be conveniently solved, using standard transfer-matrix methods [52, 73]. In particular, the acoustic reflectivity spectrum $R_a(\omega)$ can be calculated for the microcavity structure under investigation [Fig. 7-2(a)]. In the plotted frequency range, acoustic stop-bands with an acoustic reflectivity close to unity appear, extending from $\omega/2\pi = 16.6 - 19.0$ GHz and $\omega/2\pi = 52.3 - 54.7$ GHz, where ω is the phonon angular frequency.

The stop-bands correspond to bandgaps in the phonon dispersion. Introducing boundary conditions for the periodicity and using the *Bloch* theorem, it is possible to derive an equation that relates the effective phonon wavevector q of a superlattice with period $D = d_A + d_B$ to the wavevectors $q_j = \omega/v_j$ in the individual layers [76]:

$$\cos(qD) = \cos\left(\frac{\omega d_A}{v_A}\right)\cos\left(\frac{\omega d_B}{v_B}\right) - \frac{1 + (Z_A/Z_B)^2}{2(Z_A/Z_B)}\sin\left(\frac{\omega d_A}{v_A}\right)\sin\left(\frac{\omega d_B}{v_B}\right). \tag{7.2}$$

Here, d_j and v_j are the layer thickness and sound velocity of material j, respectively. The modulus of the left-hand side is ≤ 1, while the modulus of the right-hand site has

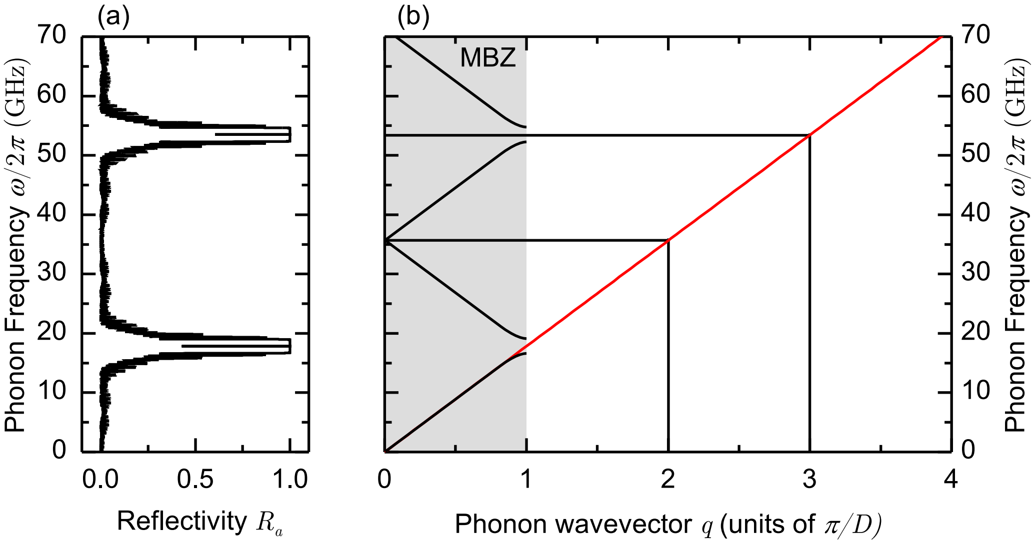

Figure 7-2: (a) Calculated reflectivity spectrum $R_a(\omega)$ of the microcavity structure, introduced in chapter 5. (b) Sketches of the bulk dispersion [red] and the effective dispersion $q(\omega)$ [black] of the the same multilayer structure as in (a), folded into the mini *Brillouin* zone (MBZ). The acoustic stop-bands correspond to bandgaps of $q(\omega)$ at the MBZ edge.

values > 1 for some frequencies ω. This leads to bandgaps in the dispersion relation $q(\omega)$ at the extrema of the left-hand side, in agreement with the *Bragg* condition: $q = m\pi/D$ [m: integer]. In Fig. 7-2(b), a sketch of the bulk dispersion is plotted together with the effective dispersion $q(\omega)$ of the DBR superlattice in the folded mini *Brillouin* zone (MBZ), $-\pi/D < q < \pi D$. There is no bandgap for even integers m, because in the studied structure $d_A/v_A = d_B/v_B$.

The meaning of the group velocity is only well defined, if the dispersion of the medium is not too large [77]. Its definition has been debated for highly dispersive media [78], but it has been demonstrated that it remains physically meaningful for coherent wave propagation even in strongly scattering media [79]. In particular, the dispersion $q(\omega)$ can be used to calculate the group transit time $t_g(\omega) \sim (d\omega/dq)^{-1}$ for high frequency coherent phonons in superlattices [80].

As illustrated in Fig. 7-2(b), $q(\omega)$ has a small gradient for phonon frequencies ω close to the stop-band edge. For a broadband strain pulse $\eta(t)$ propagating through the microcavity structure under investigation, this means that such frequency components close to the acoustic stop-band edge arrive at the QD layer with a delay, following the main part of the pulse.

The calculated temporal profile of the strain pulse, when it initially arrives at the QD layer, is shown in Fig. 7-3(a). After $t - t_S = 200$ ps the main part has passed the QD layer and is followed by a ringing. A fast *Fourier* transform of $\eta(t)$, showing the spectral intensity in the time window $t - t_S = 200 - 1200$ ps, is plotted in Fig. 7-3(b). Two distinct peaks are observed at $\omega_{s,1}/2\pi = 16.4$ GHz and $\omega_{s,2}/2\pi = 19.2$ GHz, which, within the resolution of 1 GHz, fit very well with the frequencies of the first stop-band edges.

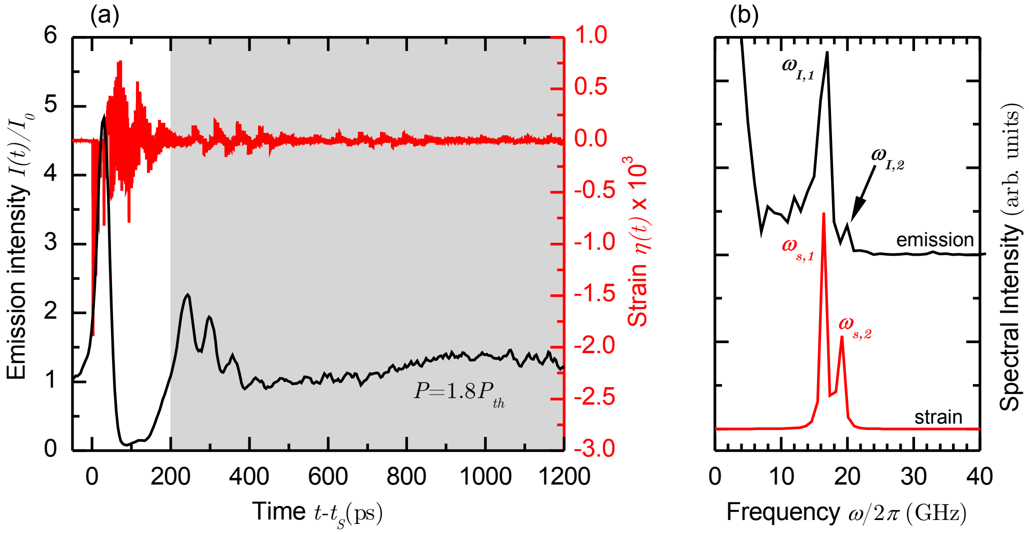

Figure 7-3: (a) Temporal dependence of the incident strain pulse $\eta(t)$ [red] and the corresponding emission intensity modulation $I(t)/I_0$ [black] for quasi-stationary excitation at $P = 1.5P_{th}$ and zero cavity detuning. (b) Spectral intensity of $\eta(t)$ [red] and $I(t)/I_0$ [black] over the timerange $t - t_S = 200 - 1200$ ps, obtained by a fast *Fourier* transform. The plots are offset for clarity.

For better comparison with the temporal profile of $\eta(t)$, the emission intensity $I(t)/I_0$ for an excitation power density $P = 1.5P_{th}$ is plotted into the same graph in Fig. 7-3(a). The reason why $I(t)/I_0$ for $P = 1.5P_{th}$ was chosen over the strongest signal at $P = 1.2P_{th}$ is simply that it is less affected by noise, due to the higher total intensity I_0 and the sensivity of the detection scheme.
From the comparison it is obvious that the harmonic modulation of $I(t)/I_0$ starts at $t - t_S = 200\,\text{ps}$, after the main part of the strain pulse has moved through the QD layer. The fast *Fourier* transform (FFT), showing the intensity of the spectral components of $I(t)/I_0$ over the timerange $t - t_S = 200 - 1200\,\text{ps}$, is plotted into Fig. 7-3(b). Apart from a low frequency background, a distinct peak appears at $\omega_{I,1}/2\pi = 17.0$ GHz and another weak one at $\omega_{I,2}/2\pi = 19.9$ GHz, which is hardly distinguishable from the noise. Both are in remarkable agreement with $\omega_{s,1}/2\pi, \omega_{s,2}/2\pi$ from the FFT of $\eta(t)$, over the same timerange, and also in agreement with the frequencies of the first acoustic stop-band edges [Fig. 7-2(a)].
The spectral analysis of $I(t)/I_0$ and $\eta(t)$, in both cases shows a weaker contribution of the higher frequency edge of the acoustic stop-band. A possible explanation might be that this *Fourier* component is weaker in the spectrum of the injected strain pulse.

The remarkable consistency, when comparing the modulation spectrum with calculations of the acoustic stop-bands, strongly supports the assumption that the harmonic modulation of $I(t)/I_0$, at times $t - t_S > 200$ ps, is due to delayed coherent phonons with frequencies at the edges of the first acoustic stop-band of the DBR superlattice.

At this point, however, it needs to be mentioned that one would expect a modulation of $I(t)/I_0$ at twice the frequency of such phonons. This is because for $E_C - E_{QD,0} = 0$, the distribution of QDs with ground state energy E_{QD} is symmetric around E_C. Consequently, a positive energy shift [compressive strain] should have the same effect as a negative energy shift [tensile strain]. This means, both half-periods of a strain oscillation should have the same effect, hypothetically leading to a modulation of $I(t)/I_0$ at twice the frequency of such an oscillation.
In reality, the modulation doesn't seem to be symmetric with regard to the direction of the energy shift, resulting in a modulation at $\omega_I = \omega_s$, instead of $2\omega_s$. The observed modulation of $I(t)/I_0$, by the main part of the strain pulse, is in agreement with this assumption. Here, the compressive leading edge results in an intensity increase [$t - t_S = 0 - 50$ ps], while the dominantly tensile parts result in an intensity decrease [$t - t_S = 50 - 200$ ps]. This has already been observed in chapter 6.2 for positive cavity detuning, in particular for excitation in the lasing regime, $P > P_{th}$. The results, presented in section 6.2 for $E_C - E_{QD,0} = 16$ meV, shall be reviewed in the following. When exciting above the lasing threshold, at $P = 3.0P_{th}$, a harmonic modulation at times $t - t_S > 200$ ps is observed also for this detuning. The amplitude is comparable to the one obtained for zero detuning [compare Fig. 7-4 and Fig. 7-1]. The *Fourier* analysis also yields the same frequencies, $\omega_{I,1} = 17.0$ GHz and $\omega_{I,1} = 19.9$ GHz. However, for an excitation power density just below the threshold, at $P = 0.9P_{th}$, where the largest peak intensity increase has been achieved, no harmonic modulation and no quenching of $I(t)/I_0$ is observed.

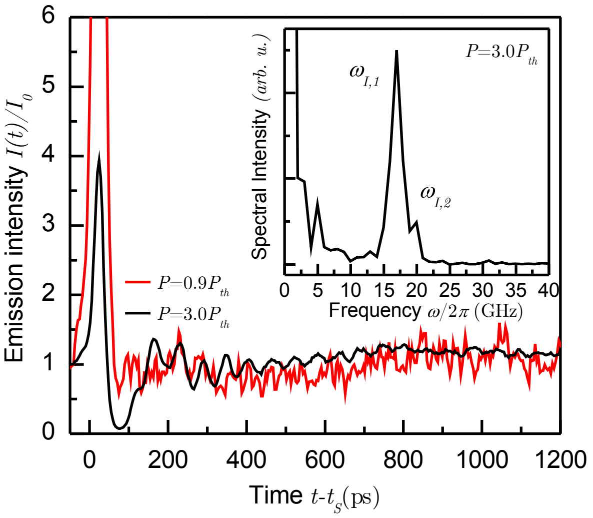

Figure 7-4: Temporal dependence of the emission intensity modulation $I(t)/I_0$ for quasi-stationary excitation and a cavity detuning of $E_C - E_{QD,0} = 16$ meV, at $P = 0.9P_{th}$ [red] and $P = 3.0P_{th}$ [black]. Inset: Spectral intensity of $I(t)/I_0$, at $P = 3.0P_{th}$, obtained by a fast *Fourier* transform over the timerange $t - t_S = 200 - 1200$ ps.

The physical mechanism responsible for the harmonic modulation of $I(t)/I_0$, therefore, seems to be different than the one responsible for the peak intensity increase. As discussed in chapter 6, the peak increase is due to a shaking induced, dynamic increase of the number of quasi-resonant QDs, to feed the laser mode. The increase is maximal, when the cavity mode is originally off-resonant [$E_C > E_{QD,0}$] and shaking leads to a dynamic crossing of the lasing threshold [optical excitation at $P \leq P_{th}$].
If the same mechanism would be responsible for the harmonic modulation, one would expect the effect to be maximal under identical conditions. The harmonic modulation, however, is the most distinct when exciting in the lasing regime. Moreover, the oscillations seem to be most visible when the cavity mode E_C is originally in resonance with the maximum of the QD energy distribution $E_{QD,0}$, unlike for the peak intensity increase [compare Fig. 7-1(b) and Fig. 6-2(b) for $P \leq P_{th}$]. And last but not least, for zero detuning, the oscillations would be expected at a frequency of $2\omega_s$, but appear at $\omega_I = \omega_s$ in the experiment.
On the other hand, the favourable conditions for the harmonic modulation and the quenching of $I(t)/I_0$ seem to be identical, which hints towards the same origin. For the above mentioned conditions, the quenching appears at tensile strain, which results in a negative shift of the electronic transition energies. As a consequence, the cavity mode E_C is quasi-resonant with the high energy flank of the QD distribution, where higher energy states may be involved in the emission dynamics [chapter 5]. For negative detuning, where only ground state emission is involved, a harmonic intensity modulation at $t - t_S > 200$ ps, is much less pronounced [Fig. 6-5(b)] and the simplified rate equation model is not able to reproduce any quenching of $I(t)/I_0$ either. It is, therefore, difficult to give an unambiguous explanation for the responsible mechanism because it is, for example, hard to estimate the influence of excited QD states.

7.3 Conclusion and perspective

In conclusion, it has been demonstrated that the laser output of a quantum dot microcavity can be harmonically modulated at about 17 GHz, using the microcavity *Bragg* reflector as a phonon filter for an incoming broadband strain pulse.
Coherent phonons with frequency at the edges of an acoustic stop-band have a longer transient time through the structure, which makes it possible to separate them from a broadband coherent phonon wavepackage. Such phonons arrive at the cavity center with a delay, when the main part of the broadband pulse has already passed. They modulate the microlaser emission intensity at their particular frequency, by shifting the electronic transition energies of the quantum dot ensemble. The modulation is the most distinct when the microlaser is operated in the lasing regime and the cavity detuning is zero. An unambiguous explanation why these are the favourable conditions cannot be given, yet. The modulation frequency of 17GHz is comparable to the current limit for such modulation.

The wavelength of the filtered phonons and, thereby, their frequency is given by the period of the superlattice. Even higher modulation frequencies may be reached, using superlattices with a shorter period. Such superlattices may be sandwiched between the microlaser and the substrate, to filter the broadband wavepackage before it enters the laser structure. Alternatively, individual layers of the optical microcavity structure itself may be substituted by acoustic superlattices with a short period [$\sim$ 10 nm]. The confined optical field merely is effected by this via an effective refractive index in such a layer, because the photon wavelength is much bigger.

Instead of just passive filtering, one may even use acoustic superlattices to build a phonon nanocavity and substitute it into the center cavity layer of the optical microcavity. Similar structures, but without a gain medium inside the resonator, have been extensively studied in recent years [e.g. [73, 74, 80, 81]]. The confinement and enhancement of phonons with frequency corresponding to the acoustic cavity mode has already been utilized, for example, to enhance *Raman* signals by many orders of magnitude [81].
Adding an active medium at the antinode of the acoustic and optic cavity field may lead to microlasers with an increased interaction between the electronic transition energies of the active medium and the confined phonon field, enabling enhanced harmonic modulation.
Ideally , the structure is designed in such a way that the laser photon field is driving the phonon cavity mode, leading to even stronger modulation amplitudes. In such a device, the coupling between photon and phonon cavity mode may by itself already result in a harmonic modulation of the laser output intensity, making the application of external broadband strain pulses unnecessary.

Part III

Acousto-plasmonics

For the realization of photonic circuits based on plasmonic nanostructures elements, which allow active control over plasmons and their interaction with light are required [10]. Several concepts, targeting the energy and propagation of plasmons, have been reported including control by temperature [82], optical excitation [83, 84, 85], electric- [86] and magnetic fields [87, 88, 89]. In order to explore the properties of plasmons in plasmonic nanostructures, it is necessary to realize nondestructive control on timescales far below 1 ns. Ultrafast control in plasmonic nanostructures has been demonstrated in several works, using femtosecond optical excitation to manipulate the dielectric function of the material [e.g. [90, 91]]. These methods, however, suffer from a number of undesireable side effects, such as thermal heating or excitation of high-energy electronic state.

Instead of modulating the dielectric function, control of plasmonic states may also be achieved by modulating the geometrical parameters of the structure. In the static case, this can be realized by the application of uniaxial stress [92, 93]. In the dynamic case, acoustic waves may be used. Acoustic control of plasmons at frequencies $\sim$ 1 THz has already been demonstrated for metallic nanoparticles [94, 95]. The concept was also applied to periodic nanostructures [96, 97, 98], but until now only modulation frequencies of up to 10 GHz have been realized.

In this work, the hybrid photonic/phononic nature of a periodic gold grating has been exploited. It is demonstrated that diffracted coherent phonons are able to modulate a surface plasmon polariton resonance in the gold grating, at frequencies of more than 100 GHz.

In addition to such applications of coherent phonons, which target the electromagnetic near-field in periodic nanostructures, they may also be used to study the far-field inside the sample below the structure. Picosecond acoustic interferometry is shown to be usuful for such investigations, where standard optical techniques are unfeasable.

The structure of this part III is as follows: In chapter 8 a review of surface plasmon polaritons and their coupling to free space photons is given. Chapter 9 features the results of SPP modulation at sub-THz frequencies by diffracted coherent phonons. Finally, in chapter 10, it will be shown that coherent phonons are suitable to study the in-sample far-field of a gold grating.

8

Surface plasmon polaritons

Surface-plasmon-polaritons (SPPs) are coupled oscillations of electrons and light, bound to the interface of a metal and a dielectric. At the same optical frequency, their momentum is larger than that of free space photons. In this chapter, the physics of SPPs will be reviewed to build a foundation for the analysis in later chapters. In section 8.1 the dielectric function of metals will be derived using *Maxwell*'s equations. The basic properties of SSPs, such as their dispersion, will be discussed in section 8.2. Finally, in section 8.3, grating coupling will be introduced as a method to bridge the momentum gap between SPPs and free space photons.

8.1 The dielectric permittivity of metals

The interaction of a metal and an electromagnetic wave may be treated classically by *Maxwell*'s equations, even for structures with a patterning of just a few nm. This is because of the high density of free carriers in the electron sea, which results in an energy spacing much smaller than k_bT [99, 12]. The optical response of metals has a strong frequency dependence, which may be described by a complex, frequency dependent dielectric permittivity $\varepsilon(\omega)$. $\varepsilon(\omega)$ shall be derived, using the macroscopic *Maxwell* equations, which link the fields $\boldsymbol{D} = \varepsilon_0\varepsilon(\omega)\boldsymbol{E}$ and $\boldsymbol{B} = \mu_0\mu\boldsymbol{H}$.

$$\begin{aligned}
\nabla \cdot \boldsymbol{D} &= \rho_{ext} \\
\nabla \cdot \boldsymbol{B} &= 0 \\
\nabla \times \boldsymbol{E} &= -\frac{\partial \boldsymbol{B}}{\partial t} \\
\nabla \times \boldsymbol{H} &= \boldsymbol{J}_{exp} + \frac{\partial \boldsymbol{D}}{\partial t}
\end{aligned} \tag{8.1}$$

Here, the total charge ρ and current densities $\boldsymbol{J}$ have been separated into internal and external densities $[\rho_{ext}, \boldsymbol{J}_{ext}]$. The metal is approximated by a sea of free electrons with number density n_e, moving against a fixed background of positive ion cores. This is a valid approximation for optical frequencies, for which interband transitions can be neglected [99]. The advantage of this phenomenological approach is that microscopic interactions of charged carriers and their rapidly varying fields are averaged and only enter the treatment via an effective electron mass m_e [77].

The equation of motion for a single electron in the electron sea takes the form

$$m_e \frac{\partial^2}{\partial t^2}\boldsymbol{x}(t) + m_e\gamma\frac{\partial}{\partial t}\boldsymbol{x}(t) = -e\boldsymbol{E}, \tag{8.2}$$

where the damping is due to collisions at a rate γ. The driving field $\boldsymbol{E} = \boldsymbol{E}_0 \cdot \exp[-i\omega t]$ shall have a harmonic time dependence. Using the result of Eq. 8.2, one gets the macroscopic polarization $\boldsymbol{P} = n_e e\boldsymbol{x}(t)$, which is linked to the electric field via $\boldsymbol{D} = \varepsilon_0\boldsymbol{E} + \boldsymbol{P}$. Combining these results yields the dielectric constant as

$$\varepsilon(\omega) = 1 - \frac{\omega_p^2}{\omega^2 + i\gamma\omega} \qquad \omega_p = \frac{n_e e^2}{\varepsilon_0 m_e} \tag{8.3}$$

Here, ω_p is the bulk plasma frequency, which marks the lower frequency boundary of the transparency regime, where transverse electromagnetic wave propagation in the metal is allowed [99]. It is also the frequency of collective longitudinal electron oscillations, called volume plasmons. For noble metals, the filled d-band close to the fermi surface results in a strongly polarized ion background. The background polarization is taken into acount by a constant offset of the permittivity in Eq. 8.3 [99], leading to

$$\varepsilon(\omega) = \varepsilon_\infty - \frac{\omega_p^2}{\omega^2 + i\gamma\omega}. \tag{8.4}$$

Equation 8.4 is used to describe the optical response of metals.

8.2 Surface plasmon polariton dispersion

Electrons at the boundary of a metal/dielectric interface can perform coherent charge fluctuations, accompanied by an electromagnetic wave in the dielectric, bound to the same interface [100]. Such a coupled state of charge oscillation and electromagnetic wave is called surface plasmon polariton (SPP).

In the following, SPPs are characterized in terms of their dispersion and spatial properties, using *Maxwell*'s equations 8.1 in form of the wave equation in non-magnetic materials [neglecting external charge and current densities, $\mu = 1$]. For a harmonic time dependence $\sim \exp[-i\omega t]$, the wave equation reduces to the *Helmholtz* equation:

$$\nabla^2\boldsymbol{E} + k_0^2\varepsilon(\omega)\boldsymbol{E} = 0 \qquad k_0 = \omega/c, \tag{8.5}$$

and analogous for $\boldsymbol{H}$. The interface is assumed to be perpendicular to the z-direction, at $z = 0$, and the wavevector k_{SPP} of the charge oscillation shall lie in the x-direction

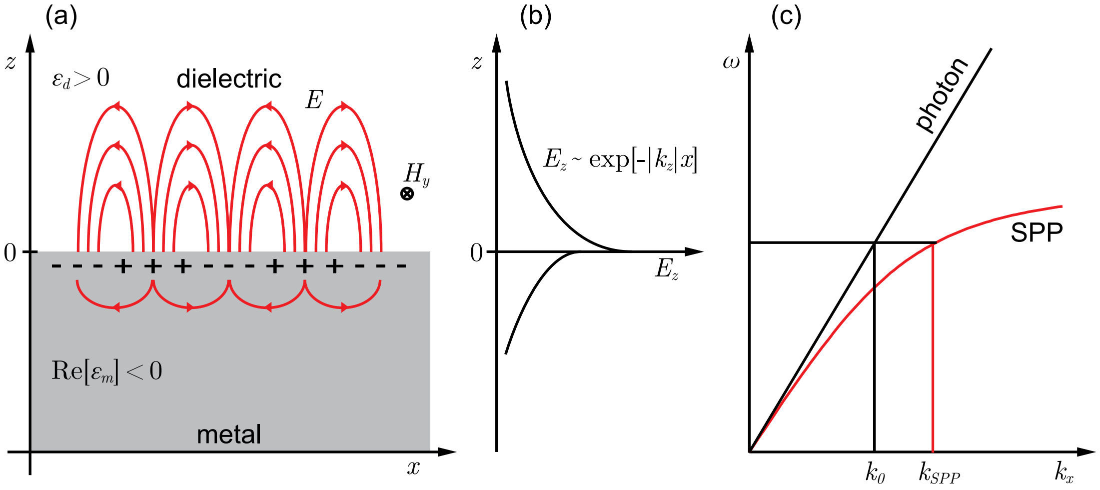

Figure 8-1: (a) Schematic of the field and charge distribution of a surface plasmon polariton (SSP), bound at a metal/dielectric interface. (b) The electric field component perpendicular to the interface is evanescent and decays exponentially within a depth of $|k_z|^{-1}$ in the respective material. (c) The dispersion curves of a free space photon [black] and a SPP [red] show that the SPP has a bigger momentum, $k_{SPP} > k_0$, than the photon, prohibiting a direct coupling. [Schematically taken out of Ref. [101]]

[Fig. 8-1(a)]. For the electric field this means: $\boldsymbol{E} = \boldsymbol{E}(z)\exp[ik_{SPP}x]$. $\boldsymbol{E}$ and $\boldsymbol{H}$ are related to each other by the curl equations in 8.1. Due to the geometrical considerations, there is only one set of self-consistent solutions, which gives non-zero components for $\boldsymbol{E}$ and $\boldsymbol{H}$ [99]. For this set of solutions, only $E_x, E_z, H_y \neq 0$, which is why it is called transverse magnetic (p-polarization). Taking into acount the continuity conditions for E_z at $z = 0$ yields

$$\begin{aligned} \boldsymbol{E}_d &= \boldsymbol{E}_{d,0}\exp\left[+zk_{d,z} + i(xk_{SPP} - \omega t)\right] \\ \boldsymbol{E}_m &= \boldsymbol{E}_{m,0}\exp\left[-zk_{m,z} + i(xk_{SPP} - \omega t)\right] \end{aligned} \tag{8.6}$$

and further

$$\frac{k_{d,z}}{k_{m,z}} = -\frac{\varepsilon_d}{\varepsilon_m(\omega)}. \tag{8.7}$$

Here, the index m and d indicate the $z < 0$ and $z > 0$ half-space, respectively. It follows from Eqs. 8.6 and 8.7 that for a confinement perpendicular to the interface of two materials m and d, the real part of their respective dielectric permittivities needs to have opposite sign. Given that material d is a dielectric with a real permittivity $\varepsilon_d > 0$, the other material has to satisfy $\mathrm{Re}[\varepsilon_m] < 0$, like metals do for $\omega < \omega_p$ [Eq. 8.4]. In this case, the z-component of E_z is evanescent and decays within a length of $|k_{m,z}|^{-1}$, $|k_{d,z}|^{-1}$ in the respective material [Fig. 8-1(b)].

Combining Eqs. 8.5,8.6 and 8.7 yields the dispersion relation of SPPs [100]

$$k_{SPP} = k_0\sqrt{\frac{\varepsilon_d\varepsilon_m(\omega)}{\varepsilon_d + \varepsilon_m(\omega)}}. \tag{8.8}$$

In Fig. 8-1(c), its real part is plotted together with the dispersion of free space photons, $k_0 = \omega/c$. As can be seen, for a fixed frqeuency ω, the momentum of SPPs is always larger than that of free space photons. Therefore, the SPP cannot transform into light, or vice versa, SPPs cannot simply be excited using incident light.
In the next section, grating coupling is introduced as a way to bridge the momentum gap and, thereby, optically excite SPPs.

8.3 Grating coupling of surface plasmon polaritons

As was pointed out in the previous section, the momentum of SPPs is always larger than the relevant component $k_x = k_0 \sin[\theta]$, parallel to k_{SPP}, of a light beam incident under the oblique angle θ. Only $k - \omega$ points to the left of the light-line $\omega = k_0 c$ are accessible using different incident angles θ [grey shaded area in Fig. 8-2].

There are several techniques available to bridge the momentum gap of SPPs and free space photons. Among others, there is evanescent prism coupling [102, 103], or the coupling via a patterning of the metal surface with a grating structure [104]. In the following, the latter is discussed, because it is the method of choice in the work presented here.

Grating coupling of free space photons to SPPs is based on the same principle that was already applied to periodic superstructures in the previous chapters. The periodic structuring gives access to multiples of the reziprocal lattice vector and, thereby, results in a backfolding of the dispersion into a mini *Brillouin* zone, as shown in Fig. 8-2(a).

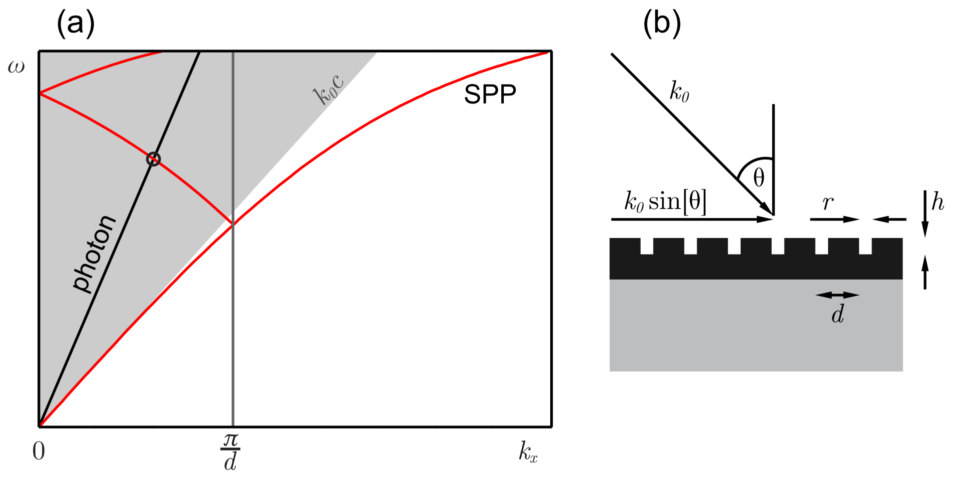

Figure 8-2: (a) Optically accessible $k - \omega$ points, $k = k_0 \sin[\theta]$ [grey shaded area]. The SPP momentum [dashed red] is unaccessible by free space photons. Patterning the metal surface with a d-perdiodic grating structure (b) results in a backfolding of the SPP dispersion [solid red] into the mini Brillouin zone with $k_x \leq \pi/d$ [dashed grey], inside the optically accessible region.

If the metal surface is patterned with a period d, the coupling condition is

$$k_{SPP} \pm \nu \frac{2\pi}{d} = k_0 \sin[\theta], \tag{8.9}$$

with k_{SPP} given by Eq. 8.8 and ν being an integer. Due to the backfolding, the $k - \omega$ points of the SPP dispersion are now accessible by free space photons. It is possible to excite SPPs with incident light, if the E-field has a component parallel to the grating wavevector, and Eq. 8.9 is fulfilled [100].
On the other hand, the opposite process is also possible. Surface plasmon polaritons may be converted into light, which, next to the inherent absorption inside the metal, gives rise to another decay channel. When illuminating the grating structure with broadband light, the SPP excitation is detected as a minimum in the reflected intensity spectrum [100].

The coupling condition given by Eq. 8.9, however, is only valid for very shallow grating structures, where the SPP perturbation is small. For deeper structures, higher order corrections need to be taken into account and, in particular, band gaps appear at the mini *Brillouin* zone borders. This is because for SPPs with wavevector π/d, standing wave solutions exist with two different charge configurations, differing in energy [105]. Since the energy stored in the electromagnetic field and the charge distribution depends on the grating region they are concentrated in, the SPP modes depend strongly on the structure parameters, such as grating height h and ridge width r [Fig. 8-2] [105, 106, 101].
The dependence of, e.g. , the reflectivity spectrum on the structure parameters can be calculated numerically, using a rigorous coupled wave analysis [107, 108].

It should, thereby, be possible to modulate a SPP resonance by changing these structure parameters. In the next chapter, it is demonstrated that acoustic pulses are a suitable tool to achieve such modulation at sub-terahertz frequencies.

9

Modulation of a surface plasmon polariton resonance by sub-terahertz diffracted coherent phonons

The main obstacle when trying to modulate plasmons in grating structures at frequencies higher than a few GHz using coherent phonons is that the wavelengths $\Lambda \sim 10\,\mathrm{nm}$ of high frequency phonons are usually smaller than the geometrical parameters of the structure $\sim 100\,\mathrm{nm}$. Here, it is demonstrated that efficient sub-THz modulation of surface plasmon polaritons in a metal grating can be achieved using diffracted coherent phonons. In this context, the gold grating plays a hybrid role. On the one hand it enables the coupling between SPPs and free space photons, as described in section 8.3. On the other hand, the periodic impedance structuring turns it into a diffraction grating for an incoming coherent phonon wavepackage. The sub-THz SPP modulation is governed by coherent, near-surface, longitudinal acoustic phonon modes due to high-order diffraction.

9.1 Experimental conditions

A scheme of the experiment is shown in Fig. 9-1. The plasmonic grating with a period of $d = 400\,\mathrm{nm}$ is made out of gold stripes with a height of $h = 80\,\mathrm{nm}$ and a gap between the individual gold stripes of $r = 50\,\mathrm{nm}$. The lattice vector lies in the x-direction. The gold grating has been fabricated on a 500 µm thick, dielectric ,[111] oriented gadolinium gallium garnet (GGG) substrate by the following process: After polishing and cleaning, a gold layer has been deposited on the substrate, by thermal evaporation, and PMMA 950 e-resist has been spin-coated on top. Subsequently, the

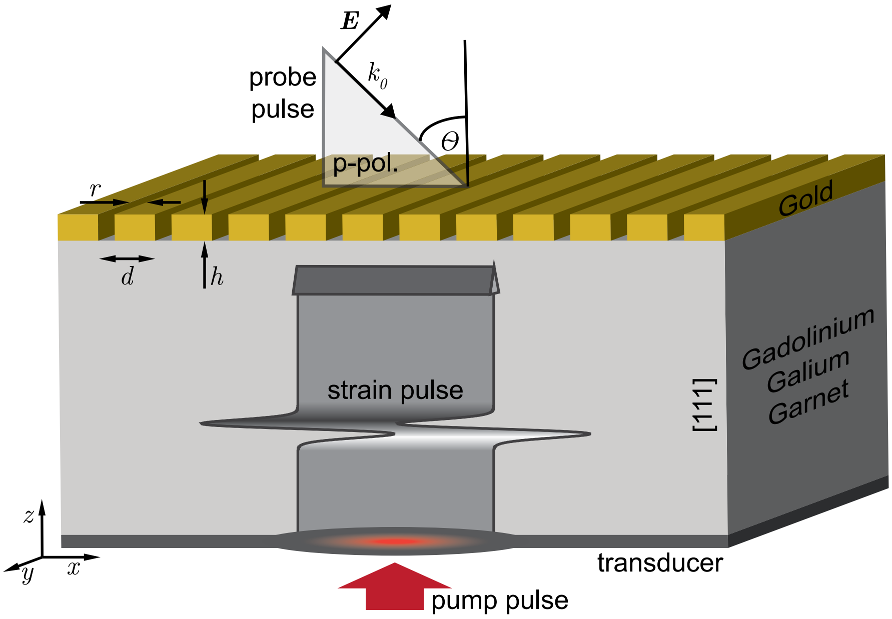

Figure 9-1: (a) Scheme of the acousto-plasmonic experiment. A gold grating on top of GGG substrate provides the coupling of SPPs to the photons of p-polarized probe pulses, incident under an angle θ. A strain pulse, excited by picosecond acoustics, is incident from the substrate side and perturbes the SPP-photon coupling when it hits the grating. Variable delay between strain- and probe pulse allows to resolve the dynamics.

grating lines have been drawn on the gold film by electron-beam lithography, using the fixed beam moving stage technique. After development, the grating pattern has been etched into the gold layer by reactive ion etching. An atomic force microscope image of the structure is plotted in Fig. 9-2(a).

Specularly reflected light, incident under an oblique angle θ, shows distinct dips in the intensity spectrum, if the electronic field lies in the incidence plane (p-polarization). The reflected intensity spectra $R_0(\lambda)$ for p-polarized light, reflected under several incidence angles θ, ranging from $2^\circ - 10^\circ$, are plotted in Fig. 9-2(b). If the $\boldsymbol{E}$ field is perpendicular to the lattice vector (s-polarization), no features are observed in the reflected intensity at any incidence angle, as exemplarily shown for $\theta = 5^\circ$ in the inset of Fig. 9-2(b). This is in agreement with the boundary conditions, as shown in section 8.2. The dips, observed in the visible range of $R_0(\lambda)$ for p-polarized light, can be associated with the SPP resonance at the GGG/gold interface, in agreement with Eq. 8.9 for ν=1.

All spectra in Fig. 9-2(b) are recorded at room temperature, but they do not change significantly at cryogenic temperatures.

A strain pulse is excited on the backside of the substrate in an aluminum transducer film, using picosecond acoustics [see chapter 1]. Such a strain pulse corresponds to a coherent phonon wavepackage propagating at the speed of longitudinal sound in GGG, $v_{GGG} = 6400\,\mathrm{m/s}$ [109]. It perturbes the SPP-photon coupling when it hits the grating structure. The dynamics of the perturbance is monitored by variably delayed

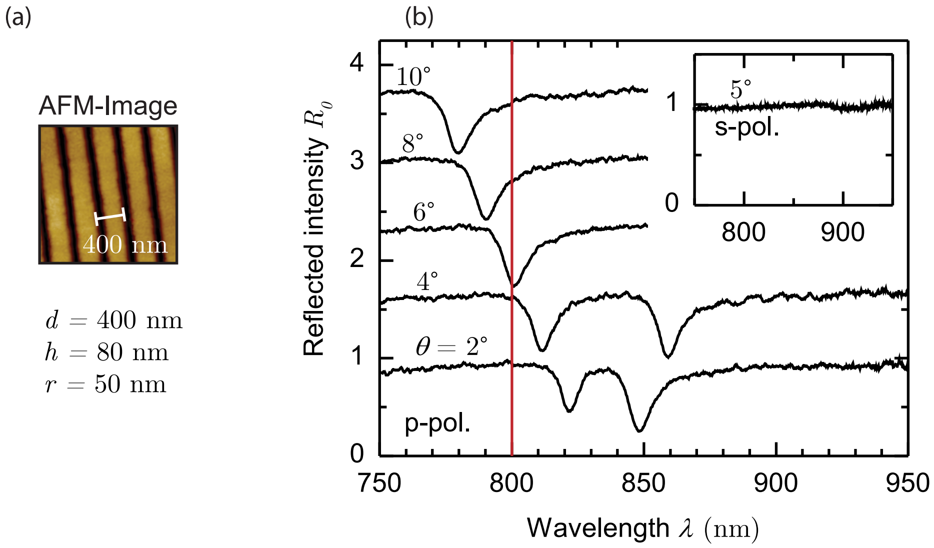

Figure 9-2: (a) Atomic force microscope image and structure parameters of the investigated grating structure. (b) Angle resolved intensity spectra $R_0(\lambda)$ of specularly reflected light with the electric field vector lieing in the incidence plain (p-pol.). The spectra are offset for clarity. The probe wavelength of $\lambda = 800$ nm [dashed red line] is positioned on the low wavelength wing of a SPP dip for an incidence angle of $\theta = 5^\circ$. No SPP features in $R_0(\lambda)$ are observed for s-polarized light [inset].

probe pulses incident under an angle of $\theta = 5^\circ$. Under these conditions, the central wavelength $\lambda = 800$ nm of the probe pulse is positioned on the low wavelength wing of the SPP resonance feature in $R_0(\lambda)$ [Fig. 9-1]. More technical details about the experimental setup are provided in section 2.2.

Experiments have been performed at cryogenic temperatures [$T = 10$ K] and also at room temperature. The difference between these two conditions lies in the damping of high frequency phonons. At room temperature, phonons with frequencies higher than a few 10 GHz are damped during the propagation due to thermal phonon scattering.

In the following, the results at cryogenic temperatures will be presented and discussed in section 9.2 and the room temperature results will be discussed in section 9.3.

9.2 Modulation by sub-terahertz diffracted coherent phonons

Experiments have been performed for a number of different excitation energy densities W on the aluminum transducer, resulting in different initial strain amplitudes. Depending on the initial strain amplitudes, non-linearities during the propagation process become important [see section 1.4]. At cryogenic temperatures, damping is negligible for the propagation distance through the substrate [110]. Consequently, the bandwidth of the coherent phonon wavepackage, when it hits the grating at the time t_s, depends on W [compare Fig. 1-3 for GaAs].

In Fig. 9-3(a) the temporal dependence of the differential reflected intensity $\Delta I(t)/I_0 = [I(t) - I_0]/I_0$ is plotted for three values of W [I_0: reflected intensity without strain]. They have been recorded with p-polarized, $\lambda = 800$ nm probe pulses, incident under the oblique angle $\theta = 5\,^\circ$, at $T = 10\,\mathrm{K}$. The spectral width of the probe pulse was $\Delta\lambda = 15$ nm.
The signal appears earlier for higher W, in agreement with non-linear propagation dynamics for $W > 1\,\mathrm{mJ/cm}^2$. Furthermore, the changes in $\Delta I(t)/I_0$ show complex temporal behaviour, different for all three values of W. Modulation amplitudes of up to 2×10^{-4}, for $W = 13\,\mathrm{mJ/cm}^2$, are observed, which is in the same range as comparable works [10^{-6} [97] to 10^{-3}[111]].
For s-polarized probe pulses, where no SPPs are excited, no changes in $\Delta I(t)/I_0$ are

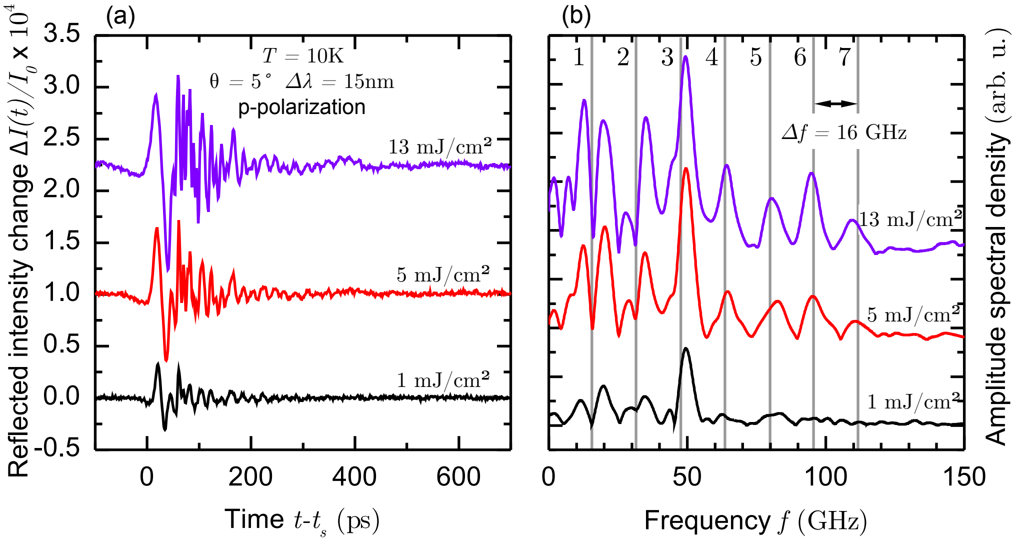

Figure 9-3: (a) Temporal dependence of the differential reflected intensity $\Delta I(t)/I_0$, probed with p-polarized optical pulses, incident under the angle $\theta = 5\,^\circ$, for three different strain excitation energy densities. (b) Amplitude spectral density, obtained by a fast *Fourier* transform of the corresponding temporal trace shown in (a). The frequencies of high-order coherent diffracted phonons are marked by vertical dashed lines. $T = 10\,\mathrm{K}$. The traces in (a) and (b) are offset for clarity.

observed. The same counts for p-polarized probe pulses, incident under the angle $\theta = 2\,^\circ$, where the probe pulse spectrum is detuned from any SPP resonance in $R_0(\lambda)$, as shown in Fig. 9-2(b).
The fact that no changes are observed, when the probe pulse does not excite SPPs, proofs that the observed changes in $\Delta I(t)/I_0$ are indeed due to a strain pulse induced modulation of the SPP-photon coupling.

The temporal traces $\Delta I(t)/I_0$, shown in Fig. 9-3(a), are analysed in the spectral domain by a fast *Fourier* transform. The amplitude spectral density of the corresponding $\Delta I(t)/I_0$ is plotted in Fig. 9-3(b). For frequencies $f > 30$ GHz, spectral features with an equal frequency spacing are observed, up to $f = 110\,\mathrm{GHz}$, for $W = 13\,\mathrm{mJ/cm^2}$. The frequency of these features does not depend on W, although the spectral density of higher frequency features is lower for smaller W. This is in agreement with the fact that the incident coherent phonon wavepackage has higher frequency components after non-linear propagation, the higher the excitation density W. The spectrum of the coherent phonon wavepackage has a maximum around $20 - 80$ GHz [16], which is most likely the reason for the intensity excess of the feature at 49 GHz.

To obtain the origin of the equally spaced high frequency features in the modulation spectrum, the possible excitations of acoustic modes at the gold grating have to be discussed. In previous works, it has already been shown that broadband strain pulses are able to excite surface acoustic waves in the grating structure [112, 98, 113]. The incident bulk waves are able to couple to the zone center waves of the periodic grating, which in the structure under study are estimated to have frequencies in the range of $5.0 - 7.5$ GHz. Therefore, this type of waves cannot be responsible for the spectral features which appear at up to 110 GHz.
On the other hand, the gold grating acts as a diffraction grating for the incident coherent phonon wavepackage. The *Bragg* condition for constructive interference between the diffracted phonons is:

$$d \sin\left[\alpha\right] = j\Lambda, \tag{9.1}$$

where α is the diffraction angle, j is the diffraction order and Λ is the phonon wavelength. For a diffraction angle of $\alpha = \pm 90\,^\circ$, counter-propagating waves result in standing near-surface acoustic waves. Even though these waves are localized very close to the GGG/grating interface, they have a bulk nature, so that Λ may be expressed in terms of the phonon frequency and speed of sound in the GGG. Finally, using Eq. 9.1, the frequency of the diffracted coherent phonons, corresponding to standing near-surface acoustic waves, is given by

$$f_j = j\frac{v_{GGG}}{d} = j \cdot \Delta f. \tag{9.2}$$

A least square fit of the peak positions in Fig. 9-3(b) with $f > 30$ GHz yields $\Delta f = 15.95 \pm 0.10\,\mathrm{GHz}$, corresponding to $v_{GGG} = 6380 \pm 40\,\mathrm{m/s}$, which within the error margin fits very well with the longitudinal sound velocity in GGG. Spectral components in $\Delta I(t)/I_0$ due to transverse acoustic (TA) phonons are not observed experimentally. Such features would be easily distinguishable from those originating from longitudinal acoustic (LA) phonons, because of their different sound velocity. The absense of

TA features is attributed to the mechanical boundary conditions, responsible for the conversion of the incident LA phonon wavepackage into diffracted TA waves. The conversion of bulk into surface acoustic waves has already been demonstrated in the low frequency case [114, 115].
The spectral width δf of the peaks in Fig. 9-3(b) does not depend on the diffraction order j. Comparing with optical diffraction gratings, this behaviour is indeed expected. The width of a spectral line does not depend on the diffraction order, but it depends only on the number N of coherently interfering grating periods [52].

$$\delta f = \frac{v}{Nd|\sin[\alpha] - \sin[\alpha_0]|}. \tag{9.3}$$

Here, v is the phase velocity in the medium, into which the wave is diffracted and α_0 is the incidence angle. The spectral width of about $\delta f = 7\,\text{GHz}$ in our experiment leads to $N \approx 2$ [$v = v_{GGG} = 6400\,\text{m/s}$, $d = 400\,\text{nm}$, $\alpha_0 = 0\,°$, $\alpha = 90\,°$], corresponding to a mean free path of $\sim 1\mu m$ for the diffracted coherent phonons. A possible reason for such a low value of N may be that near-surface acoustic waves are diffracted by the gold grating again, in the same way as the incident phonon wavepackage.
The fact that the frequencies of the spectral features in $\Delta I(t)/I_0$ can be well described by Eq. 9.1 and the independence of the spectral width δf on j are strong hints that the spectral features for $f > 30\,\text{GHz}$ and, therefore, the perturbance of the SPP-photon coupling are indeed caused by diffracted coherent phonons. The exact mechanism of this perturbance is discussed in the following.

To illustrate the interaction of near-surface acoustic waves with the gold grating, the lateral dependence of the corresponding displacement field $u_x(x)$ in the x-direction is exemplarily sketched together with the grating in Fig. 9-4, for $j = 1$. From the elastic boundary conditions it follows that the displacement profile $u_x(x)$ is an odd

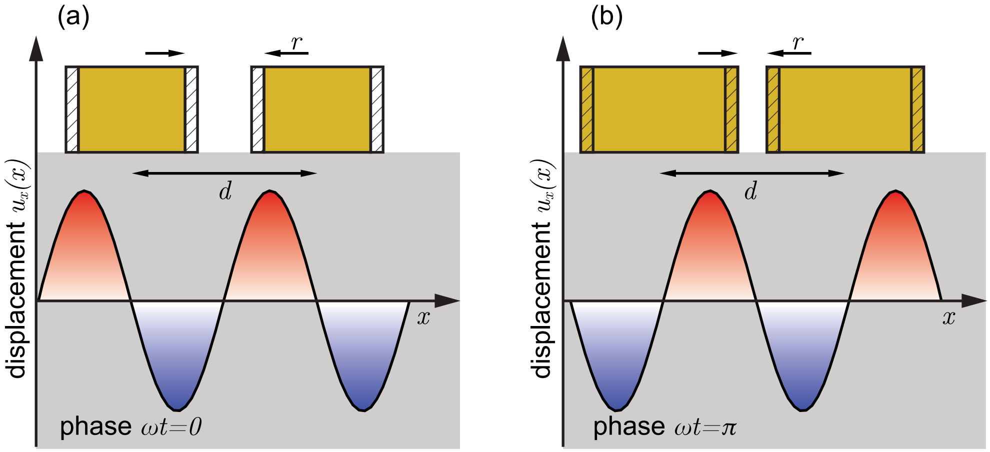

Figure 9-4: Sketch of the displacement profile $u_x(x)$ of the first order ($j = 1$) near-surface acoustic waves and their interaction with the gold grating. The temporal phase is either $\omega t = 0$ (a) or $\omega t = \pi$ (b). In any case, the grating period d remains the same, but the slit width r is either increased (a) or decreased (b). The dashed area marks the change from the equilibrium position.

function with respect to the middle of the grating stripes, if the grating profile is an even function of x [116]. As a consequence, the displacement by diffracted coherent phonons does not change the periodicity d of the grating, but it affects the slit width r. In Fig. 9-4 (a) and (b), the phase ωt of the temporal oscillation is 0 (a) and π (b), resulting in either tension or compression of r, respectively.

The effect of the slit width change Δr is twofold. On the one hand, it affects the coupling between SPPs, associated with the gold/air and gold/GGG interface. On the other hand, the coupling of SPPs to free space photons is perturbed. As mentioned in section 8.3, the consequence of any geometrical change on the reflection spectrum $R_0(\lambda)$ can be calculated numerically, using a rigorous coupled wave analysis (RCWA)[107, 108]. The calculated spectrum of the reflected intensity $R_0(\lambda)$ is plotted in the upper panel of Fig. 9-5(a), for an incidence angle of $\theta = 5^\circ$ [1]. In the lower panel, the spectral dependence of the differential reflectivity change $\Delta R(\lambda)/R_0 = [R(\lambda) - R_0]/R_0$ due to a slit width variation of $\Delta r = 0.01$ nm is plotted. The change of r mainly leads to a spectral shift of the SPP resonance, resulting in the bipolar profile of $\Delta R(\lambda)/R_0$. Since the reflected intensity I is an integral of $\Delta R(\lambda)/R_0$ over the spectral width $\Delta\lambda$ of the probe pulse, the signal amplitude $\Delta I/I_0$ depends not only on λ, but also on $\Delta\lambda$. The spectrum of the optical probe pulse [dashed red], used for the measurements presented in Fig. 9-3, is plotted next to the reflected intensity spectrum

---

[1] All RCWA calculations have been performed by V. I. Belotelov, Lomonosov Moscow State University, 119991 Moscow, Russia

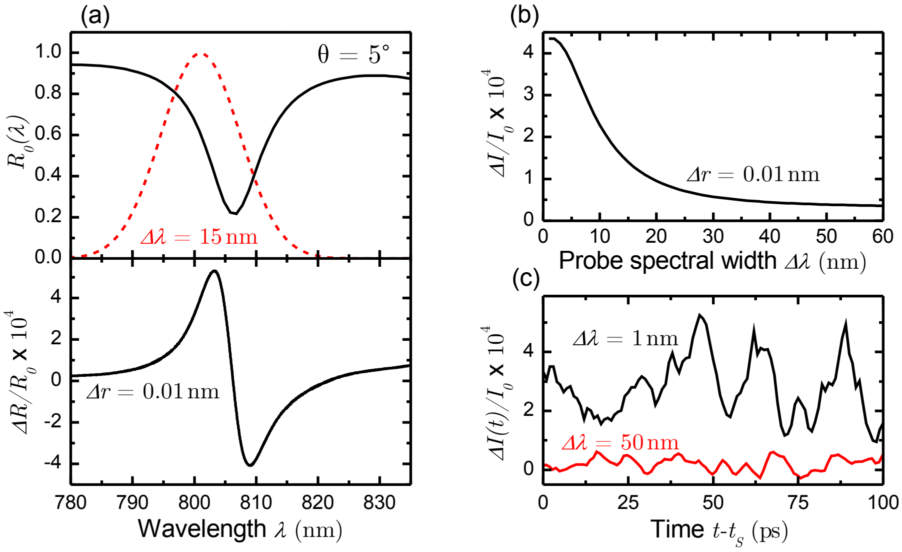

Figure 9-5: (a) Top panel: Calculated reflectivity spectrum $R_0(\lambda)$ for light incident under an angle of $\theta = 5^\circ$ [black] and the spectrum of a probe pulse with $\Delta\lambda = 15$ nm spectral width [dashed red]. Bottom panel: Differential change $\Delta R(\lambda)/R_0$ of the spectrum shown in the top panel, for a slit width variation of $\Delta r = 0.01$ nm. (b) Dependence of the integrated reflected intensity amplitude $\Delta I/I_0$ on $\Delta\lambda$, for probe pulses centered at $\lambda = 800$ nm. (c) Experimental results of $\Delta I(t)/I_0$ for probe pulses with different spectral widths $\Delta\lambda = 1$ nm [red] and $\Delta\lambda = 50$ nm [black].

in the top panel of Fig. 9-5(a). The wavelength $\lambda = 800\,\mathrm{nm}$ is positioned on the short wavelength wing of the SPP resonance and the spectral width $\Delta\lambda = 15$ nm overlaps dominantly with the positive part of $\Delta R(\lambda)/R_0$. The reflected intensity amplitude $\Delta I/I_0 = 10^{-4}$ for $\Delta\lambda = 15$ nm and $\Delta r = 0.01$ nm fits very well with the results presented in Fig. 9-3(a). The depdence of $\Delta I/I_0$ on the spectral width $\Delta\lambda$ of the probe pulse for $\Delta r = 0.01\,\mathrm{nm}$ is plotted in Fig. 9-5(b). The biggest amplitude appears for a spectrally narrow pulse, which overlaps with just one wing of the bipolar profile. On the contrary, for a large probe bandwidth, the contributions of both parts of the bipolar profile $\Delta R(\lambda)/R_0$ cancel each other, resulting in a small amplitude $\Delta I/I_0$.
To proof this dependence, identical experiments with $\Delta\lambda = 1$ nm and 50 nm have been performed, plotted in Fig. 9-5(c). The high frequency features have amplitudes of about $4 \cdot 10^{-4}$ and $0.5 \cdot 10^{-4}$, respectively, in good agreement with theory, which predicts about one order of magnitude difference.
The conformity between theory and experiment for the reflectivity spectra and the predicted $\Delta\lambda$ dependence of the spectrally integrated signals $\Delta I(t)/I_0$ confirms the proposed modulation mechanism, which is based on the grating slit width variation Δr due to diffracted coherent phonons.

9.3 Modulation by surface acoustic modes

Turning to the lower frequency part [$f < 30$ GHz] of the spectra shown in Fig. 9-3(b), the features cannot be described by Eq. 9.2 anymore. In particular, at $f = 16$ GHz, where a peak by the first order near-surface acoustic waves would be expected, a dip in the spectral density is observed. In the frequency range $f < 30\,\mathrm{GHz}$, several surface acoustic modes may be excited [112, 98, 113]. The effect on the measured signal depends

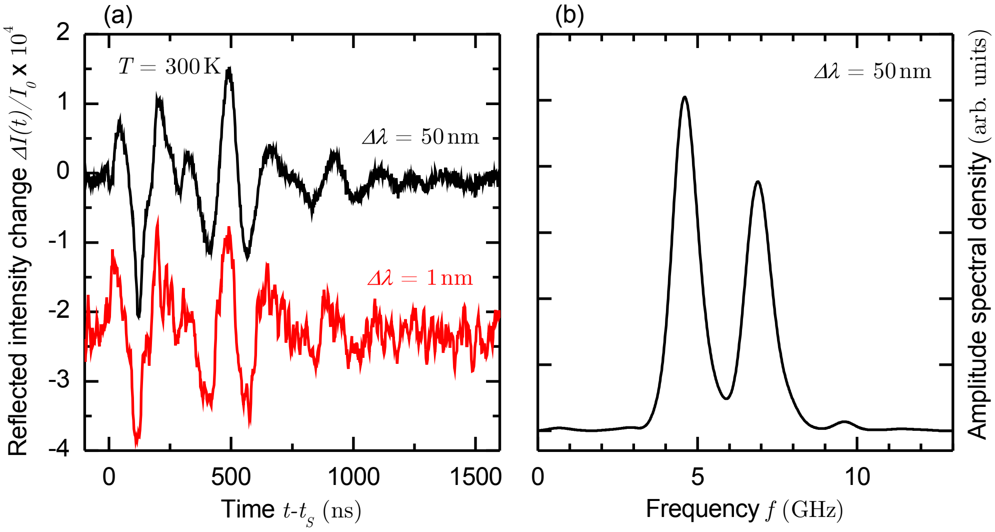

Figure 9-6: (a) The time evolution of the reflected intensity $\Delta I(t)/I_0$ after strain pulse impact, for two different probe spectral widths $\Delta\lambda = 1$ nm [red] and 50 nm [black]. (b) Amplitude spectral density of the time evolution in (a), for $\Delta\lambda = 50\,\mathrm{nm}$.

on their interaction with bulk modes in GGG. The dip at $f = 16$ GHz, for example, may be explained by a Fano resonance due to the interaction of a surface acoustic wave with the near-surface acoustic bulk wave. To investigate the effect of surface acoustic modes and their interaction with SPPs without the influence of diffracted coherent phonons, identical measurements as before have been performed, but at room temperature $T = 300$ K. At room temperature, higher frequency components in the incident strain pulse are damped completely during the propagation through the 500 µm thick substrate due to scattering at thermal phonons [110].

The time evolution of the reflected intensity $\Delta I(t)/I_0$ after strain pulse impact is plotted in Fig. 9-6(a), for two different probe spectral widths $\Delta\lambda = 1$ nm and 50 nm. Despite a higher noise level for $\Delta\lambda = 1$ nm, the time evolution is identical for both $\Delta\lambda$. The fast *Fourier* transform of the signal, shows at least two spectral components at $f = 4.6$ GHz and 6.9 GHz associated with surface acoustic modes. Their interaction with SPPs is fundamentally different from that of diffracted coherent phonons, proofed by the fact that $\Delta I(t)/I_0$ is independent of $\delta\lambda$. A comprehensive discussion of these modes is beyond the scope of this work.

9.4 Conclusion and perspective

In conclusion, it has been demonstrated that diffracted coherent phonons are able to efficiently modulate the intensity of an optical probe pulse, at sub-terahertz frequencies, which has been specularly reflected by a gold grating, if the probe spectrum is narrow and overlaps with the wing of a SPP resonance. In this context, the gold grating plays a hybrid role, because it provides the coupling of SPPs to free space photons and at the same time acts as a diffraction grating for an incoming broadband coherent phonon wavepackage. The mechanism responsible for the intensity modulation is a variation of the grating slit width, resulting in a shift of the SPP resonance in the reflectivity spectrum. The method has potential for applications in high-frequency plasmonics and nanophotonics.

The need for cryogenic temperatures in the experiments presented here was due to damping of higher frequency phonons in the incident wavepackage by scattering at thermal phonons, during the propagation through the substrate. The influence of damping can be minimized, by using thinner substrates with thicknesses ~ 10 nm, potentially allowing room temperature operation.

A further tailoring of modulation frequencies can be achieved by similar strain pulse shaping techniques proposed in previous chapters. In particular, phonon filtering by acoustic superlattices [80] should allow to harmonically modulate the SPP by selectively exciting diffracted coherent phonons of a single diffraction order. Alternatively, superlattices may be used as the acoustic transducer to create monochromatic strain waves [72].

In the experiments presented in this chapter, acoustic waves were used to perturb the plasmonic structure in the near-field region, where the electric field of SPPs is localized. In the next chapter, it will be demonstrated that coherent phonon wavepackages are also suitable to probe the electromagnetic field in the far-field region inside the structure, which is difficult to access by optical techniques.

10

Studying periodic nanostructures by probing the in-sample optical far-field using coherent phonons

Periodic optical nanostructures are interesting for various applications, as mentioned, for example, in previous chapters. Coherent phonons in the GHz and THz range have already been utilized to study these structures. In particular, the interaction of excited vibrational modes with light has been studied by picosecond acoustics techniques in photonic-phononic crystals [117, 118], hole arrays [86], metallic gratings [112, 113, 119] and complex periodic plasmonic nanostructures [120]. All these experiments, however, are targeting the near-field region in the vicinity of less than one optical wavelength away from the nanostructure. The far-field region, where the electromagnetic field has a well defined wavevector and a corresponding propagation direction [98], has received less attention.

In the following, in section 10.1, picosecond acoustic interferometry will be reviewed as a method to study the elastical, optical and elasto-optical properties of solids. In section 10.2, it will be shown that it is a particularly useful method to probe the in-sample optical far-field inside media with periodic optical nanostructurers on top, which is challenging with all-optical techniques. It will be shown that strong spectral components, associated with diffracted beams, are detected in the picosecond acoustic inteferometry signal. A theoretical analysis underlines the observations and provides a tool for the design of nanostructures, where the interaction of light with coherent phonons can be deliberately exploited.

10.1 Picosecond acoustic interferometry

When an electromagnetic wave with vacuum wavevector k is normally incident on the surface of a transparent medium with refractive index n, a part of it is reflected due to the refractive index contrast. For this to happen, a momentum transfer of $2nk\hbar$ has to occur. If the momentum is provided by elastic collision with an acoustic phonon, the frequency of the reflected electromagnetic wave is shifted by $\omega_0 = 2nvk$, where v is the sound velocity inside the medium. *Brillouin* scattering measurements of the reflected spectrum to determine ω_0, the *Brillouin* frequency, have been widely used to study the velocity and attenuation of acoustic waves in solids [e.g. [121]].

In an advanced approach, the electromagnetic wave is reflected at a coherent phonon wavepackage [e.g. a picosecond strain pulse $\eta(z,t)$]. Based on this principle, picosecond acoustic interferometry is an established technique to study optical, elastic and elasto-optical properties in crystalline and amorphous bulk materials and thin films [122, 123, 124, 125, 126, 127, 128, 129]. The principle of this technique is sketched in Fig. 10-1(a). A strain pulse $\eta(z,t)$, excited by picosecond acoustics [chapter 1], is propagating at the speed of sound towards the surface of a sample, locally changing the optical constants of the medium. From the opposite side of the interface, an optical probe pulse is incident under the oblique angle θ. A part of the probe pulse is reflected at the interface and another one at the strain pulse. The reflected pulses interfere either constructively or destructively, depending on the position z of the strain pulse.

The reflection at the strain pulse occures because it changes the dielectric permittivity $\varepsilon = (n + i\kappa)^2$. If a transparent medium is considered [$\kappa = 0$], the change of ε is [16]

$$\Delta\varepsilon(z,t) = 2n\frac{\partial n}{\partial \eta}\eta(z,t). \tag{10.1}$$

Let the surface be located at $z = 0$. In this case the complex amplitude reflection coefficient of the two interfering beams is

$$\begin{aligned} r(t) &= r_0 + \frac{ik}{2}t_0^{(+)}t_0^{(-)}\int_0^\infty \Delta\varepsilon(z,t)\exp\left[2ikn\cos[\theta]z\right]\,dz \\ &= r_0 + \Delta r(t). \end{aligned} \tag{10.2}$$

Here, r_0 is the reflection coefficient for the incident beam at the sample surface and $t_0^{(+)}, t_0^{(-)}$ are the transmission coefficients of light at the same interface, incident from $z > 0$ and $z < 0$, respectively. It is straight forward to show that for a strain pulse travelling at the speed of sound v, the phase of $\Delta r(t)$ changes with the *Brillouin* frequency [127]

$$\omega_0 = \frac{4\pi v}{\lambda}\sqrt{\varepsilon - \sin^2[\theta]}, \tag{10.3}$$

where λ is the center wavelength of the optical probe pulse in vacuum. In picosecond acoustic interferometry experiments, the probe pulse is variably delayed with respect

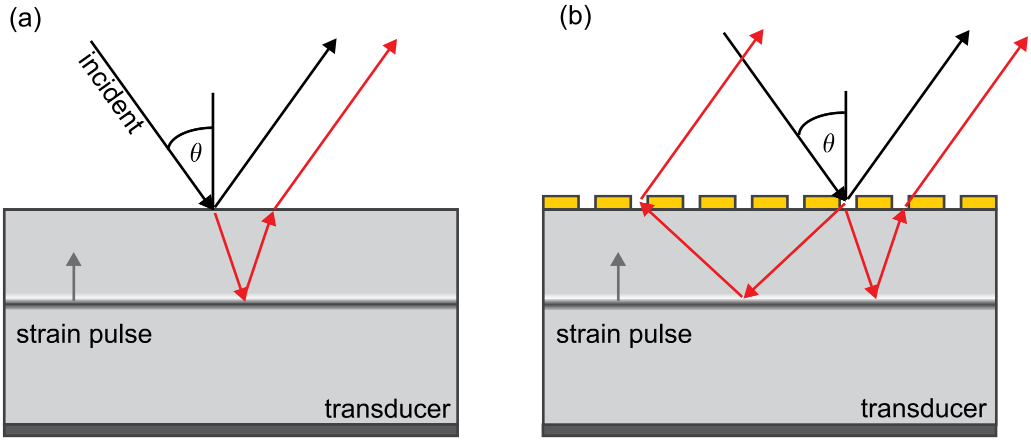

Figure 10-1: (a) Classic picosecond acoustic interferometry scheme. Parts of a probe pulse, incident under the angle θ, are reflected at the surface of a transparent medium [black] and at a strain pulse propagating towards the surface [red]. The interference of both parts is analysed depending on the position of the strain pulse. (b) Picosecond acoustic interferometry with a periodic nanostructure on top. Additional components appear[dashed red], due to the diffraction of light.

to the strain pulse and oscillations with frequency ω_0 are detected in the differential reflectivity signal [16]

$$\Delta R(t) = |r_0 + \Delta r(t)|^2 - |r_0|^2. \tag{10.4}$$

These features are usually called *Brillouin* oscillations.

10.2 Probing the in-sample optical far-field of periodic nanostructures

If the sample surface is not a flat interface, but with a periodic optical nanostructure positioned on top, the electromagnetic wave inside the sample may no longer be a simple plain wave, as sketched in Fig. 10-1(b). The periodicity leads to diffraction of light incident on the sample surface under an angle θ, leading to additional contributions to the picosecond acoustic interferometry signal. For example, in a diffraction grating with period d, the first negative diffraction order results in a *Brillouin* oscillation frequency of

$$\omega_{-1} = \frac{4\pi v}{\lambda}\sqrt{\varepsilon - (\lambda/d - \sin[\theta])^2}. \tag{10.5}$$

Coherent phonon wavepackages are, thus, a promising tool to study the in-sample optical far-field.

The structure under study is a short-period diffraction grating made of gold, fabricated on top of the (111) plane of a 500 µm thick gadolinium gallium garnet (GGG) substrate with an intermediate layer of bismuth-substituted rare-earth iron garnet (BIG)

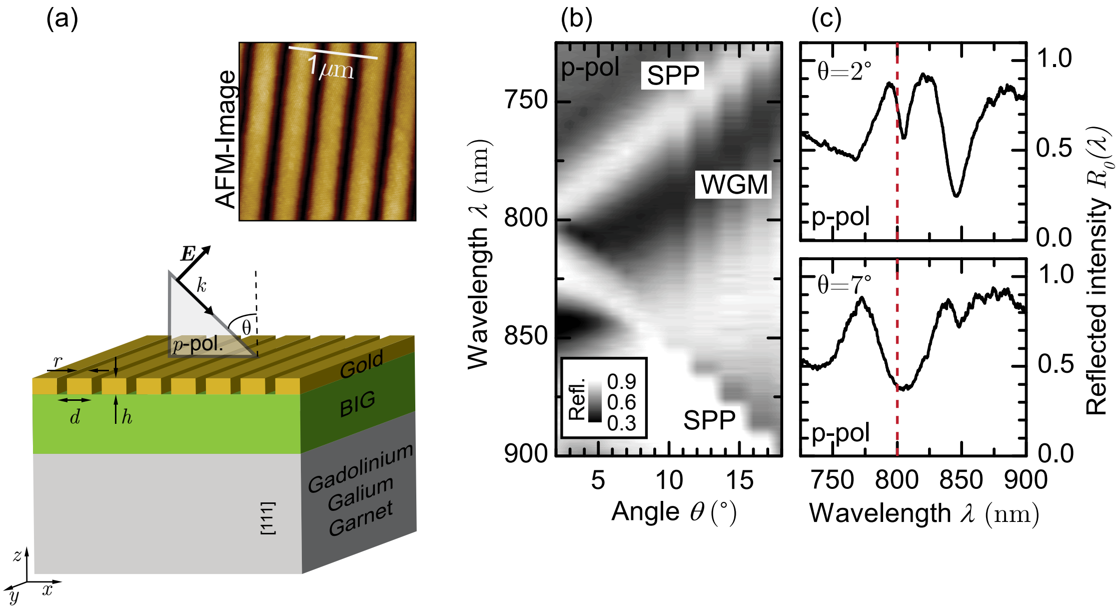

Figure 10-2: (a) Structure and detection geometry of the studied sample, together with an atomic force microscope image of the gold grating. (b) Angle dependence of the reflected intensity spectra $R_0(\lambda)$ in a grayscale plot for p-polarized white light. (b) $R_0(\lambda)$ for $\theta = 2^\circ$ and 7°. The dashed vertical red line marks the probe pulse wavelength for the interferometry experiments.

of 355 nm thickness [Fig. 10-2(a)]. The geometrical parameters of the gold grating [period d = 400 nm, height h = 80 nm, slit width r = 115 nm] were optimized to have distinct dips in the spectrum of the reflected intensity $R_0(\lambda)$ over a wide spectral range for p-polarized light [Fig. 10-2(b)]. The spectra for the incidence angles $\theta = 2^\circ$ and 7° are highlighted in Fig. 10-2(c). The features visible in these spectra are due to *Wood* anomalies which are governed by SPP resonances of the gold grating and a waveguiding mode (WGM) in the BIG layer [89, 91].
The experimental scheme for the picosecond acoustic interferometry measurements is identical to the one presented in Fig. 9-1 of chapter 9 and the details of the setup are given in section 2.2. A strain pulse is excited in a 50 nm thick aluminum transducer, using picosecond acoustics. It travels through the GGG substrate at the speed of longitudinal sound, v_{GGG} = 6400 m/s, within a time of ∼ 80 ns. A probe pulse, originating from the same femtosecond laser, is incident from the sample front to measure the differential reflected intensity $\Delta I(t)/I_0$. The time resolution is achieved by a variable delay between probe pulse and strain pulse excitation. All experiments have been performed at room temperature and the strain pulse excitation density is $W = 10\,\mathrm{mJ/cm^2}$.

The interferometry signals $\Delta I_s(t)$ and $\Delta I_p(t)$ measured for probe pulses incident under $\theta = 7^\circ$ with s- and p-polarization, respectively, are plotted at the top of Fig. 10-3(a). For these conditions, the reflected intensity spectrum, shown in Fig. 10-2(c), has a distinct dip at the probe center wavelength of $\lambda = 800$ nm. The signal at $t - t_S > 0$ has already been discussed in chapter 9 and earlier works [86, 112, 113, 119] and is

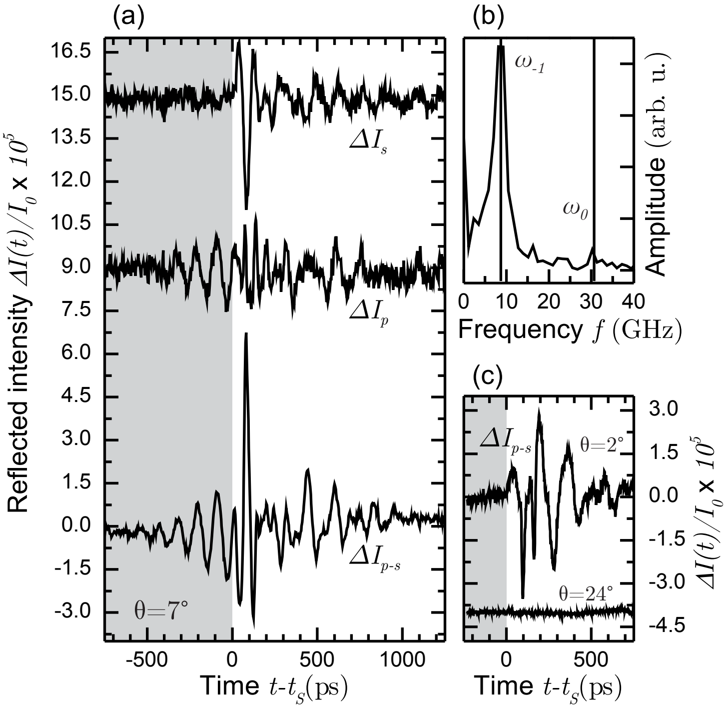

Figure 10-3: (a)Interferometry signals $\Delta I(t)/I_0$ obtained for probe pulses at $\lambda = 800$ nm, incident under $\theta = 7^\circ$. The index indicates the polarization [$p-s$: balanced detection $\Delta I_p - \Delta I_s$]. (b) FFT of ΔI_{p-s} over the time interval $t - t_S = -850$ ps to 0 ps [gray shaded area in (a)]. The solid and dashed line mark the expected frequencies ω_0 and ω_{-1}, respectively. (c) ΔI_{p-s} for $\theta = 2^\circ$ and 24°.

related to the acoustic perturbance of the electromagnetic near-field [t_S: time when the strain pulse hits the gold grating]. The main subject of interest here is the non-zero signal at $t - t_S < 0$ [gray shaded area], when the strain pulse did not yet reach the grating. It is only observed for p-polarization, which allows to achieve a better signal to noise ratio, by measuring the difference signal $\Delta I_{p-s}(t) = \Delta I_p(t) - \Delta I_s(t)$, using incident probe pulses with s- and p-components of equal intensity in combination with a balanced detector. The difference signal is plotted at the bottom of Fig. 10-3(a). $\Delta I_{p-s}(t) = \Delta I_p(t)$ for $t - t_S < 0$, because for these times $\Delta I_s(t) = 0$.
Oscillatory behaviour is observed already at $t - t_S < -400$ ps. This part of the signal $\Delta I_{p-s}(t)$ is analysed in the spectral domain by taking a fast *Fourier* transform (FFT) for the time interval from $t - t_S = -850$ ps to 0 ps, shown in Fig. 10-3(b). The amplitude spectrum shows a dominant peak, centered at $f = 8.5$ GHz with a width of 2.5 GHz.
In Fig. 10-3(c), the difference signal $\Delta I_{p-s}(t)$ is plotted for the incidence angles $\theta = 2^\circ$ and 24°. In both cases, no signal at $t - t_S < 0$ is observed, for $\theta = 24^\circ$ no signal is observed even at $t - t_s > 0$.

In the following, $\Delta I_{p-s}(t)$ for $\theta = 7^\circ$ and $t - t_S < 0$ shall be analyzed. In particular, the origin of the spectral components, shown in Fig. 10-3(b), is of interest. The strain pulse reaches the BIG/GGG interface at $t - t_S \approx 50$ ps, so that the major part of the interferometry signal is due to *Brillouin* scattering in GGG and the analysis can be restricted to GGG only. The fundamental *Brillouin* frequency $f_0 = \omega_0/2\pi$ can be calculated using Eq. 10.3 and literature values for the parameters ε and v in GGG [ε_{GGG}=3.8 [130], $v_{GGG} = 6400$ m/s [109]]. It amounts to $f_0 = 31.1$ GHz, illustrated by the solid vertical line in Fig. 10-3(b). The *Brillouin* frequency $f_{-1} = \omega_{-1}/2\pi$ [Eq. 10.5], associated with the first negative diffraction order, yields $f_{-1} = 8.3$ GHz [dashed vertical line in Fig. 10-3(b)], close to the dominant feature in the FFT spectrum of $\Delta I_{p-s}(t)$ at 8.5 GHz. It, therefore, seems likely that the signal for $t - t_S < 0$ is dominated by the interference of the two reflected components, sketched as black and dashed red curves in Fig.10-1(b). One is the part of the probe pulse that is specularly reflected at the sample surface, the other part is associated with diffracted light of the first negative diffraction order, which is subsequently reflected by the strain pulse and diffracted back into free space.

In order to underline this assumption and to understand why the component with frequency f_0 is so weak compared to f_{-1} in the experimentally measured spectrum, a further theoretical analysis of the relative intensities in the interferometry signal $\Delta R/R_0$ is performed.
As pointed out in section 10.1, the strain pulse $\eta(z,t)$ perturbes the dielectric permittivity tensor ε. More precisely, the strain pulse with $\eta(z,t) = \eta_{zz}(z,t)$ changes only the diagonal components of ε

$$\begin{aligned}\Delta\varepsilon_{xx} &= \Delta\varepsilon_{xx} = -\varepsilon^2 p_{12}\eta(z,t)\\ \Delta\varepsilon_{zz} &= -\varepsilon^2 p_{11}\eta(z,t),\end{aligned} \tag{10.6}$$

where p_{12} and p_{11} are photo-elastic constants. Using a similar approach as in section 10.1 together with perturbative solutions of the *Maxwell* equations, the expression of $\Delta R/R_0$ for the present experimental conditions can be derived [1][details in the supplementary material of Ref. [131]]. For $\theta = 7\,^\circ$, $\lambda = 800$ nm and the geometrical parameters of the structure, only light of the diffraction orders 0 and -1 can propagate inside GGG, leading to

$$\begin{aligned}\frac{\Delta R}{R_0} = v\varepsilon\sqrt{2\pi}\ \mathrm{Re}\Bigg[&\frac{t^{(-)}_{00}t^{(+)}_{00}}{ik_0 r^{(+)}_{00}}\eta_{\omega_0}(p_{11}k_{||}^2 - p_{12}k_0^2)\exp[-i\omega_0 t]\\ &+ \frac{t^{(-)}_{-10}t^{(+)}_{0-1}}{ik_{-1} r^{(+)}_{00}}\eta_{\omega_{-1}}\left(p_{11}\left(k_{||} - \frac{2\pi}{d}\right)^2 - p_{12}k_{-1}^2\right)\exp[-i\omega_{-1}t]\Bigg].\end{aligned} \tag{10.7}$$

Here, $k_{||} = k\sin[\theta], k_0 = \sqrt{k^2\varepsilon - k_{||}^2}$, $k_{-1} = \sqrt{k^2\varepsilon - \left(k_{||} - 2\pi/d\right)^2}$, and k is the wavevector in vacuum. $r^{(+)}_{00}$ ($t^{(+,-)}_{mn}$) are the complex coefficients of the reflection (transmission) amplitudes for the magnetic field component of light in the periodic structure without strain, respectively. The upper index in $t^{(+,-)}_{mn}$ indicates light incident from the air (+) or GGG (-) side. The lower indices in $t^{(+,-)}_{mn}$ indicate the diffraction order of the incident (m) and transmitted (n) light. The first term in Eq. 10.7 describes *Brillouin* oscillations with frequency ω_0 due to non-diffracted light scattered by coherent phonons ($m = n = 0$). The second term in Eq. 10.7 describes oscillations with frequency ω_{-1} due to the scattering of diffracted light of the first negative order. Moreover, it is assumed that during the time interval of the interferometry signal, the strain pulse doesn't change its shape, e.g., due to anharmonicity [section 1.4]. In this case, $\eta(z,t) = \eta(t - z/v)$ with the *Fourier* components $\eta_\omega = \frac{1}{\sqrt{2\pi}}\int_{-\infty}^{\infty}\eta(\tau)\exp[i\omega t]d\tau$.

---

[1] The epression for $\Delta R/R_0$ in Eq. 10.7 was derived by B. A. Glavin, Lashkaryov Institute of Semiconductor Physics, 03028 Kyiv, Ukraine

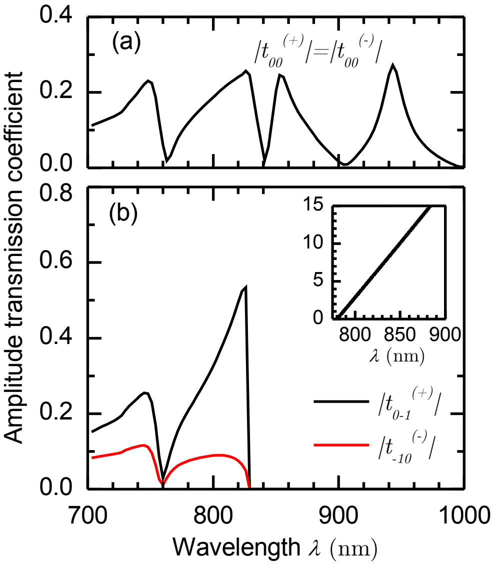

Figure 10-4: Modulus of the complex coefficients $t_{mn}^{(+-)}$ for the transmission of a probe pulse with λ = 800 nm, incident under the angle $\theta = 7^\circ$, into the 0th order (a) and first negative order (b)[black] of diffraction inside GGG, and back from GGG into air (b)[red]. The inset shows the wavelength depence of the cut-off angle θ_C, below which light cannot propagate inside GGG.

From Eq. 10.7 it is obvious that a significant contribution to the interferometry signal at the frequency ω_0 $[\omega_{-1}]$ is only expected, if the factors $t_{00}^{(-)}t_{00}^{(+)}/r_{00}^{(+)}$ $\left[t_{-10}^{(-)}t_{0-1}^{(+)}/r_{00}^{(+)}\right]$ are non-negligible. This can already explain the fact that no signal is observed for probe light incident under $\theta = 24^\circ$ [Fig. 10-3(c)], because for this angle $\lambda = 800$ nm is far from any optical resonance and thus $t_{00}^{(-)}t_{00}^{(+)}/r_{00}^{(+)} = t_{-10}^{(-)}t_{0-1}^{(+)}/r_{00}^{(+)} \approx 0$.

The transmission and reflection coefficients are calculated by a rigorous coupled wave analysis (RCWA) [107, 108]. In Fig. 10-4, the calculated transmission coefficients $t_{mm}^{(+,-)}$ are plotted in dependence of the probe pulse wavelength λ [1]. The maxima of the transmission spectra for the fundamental mode $|t(+)_{00}| = |t(-)_{00}|$, shown in (a), correspond well to measured dips in reflection [Fig. 10-2(c)]. For the first negative diffraction order, however, there is a cut-off wavelength above which light cannot propagate inside GGG. For a fixed wavelength this translates into a cut-off angle θ_C. For non-negligible transmission coefficients $t_{0-1}^{(+)}$ and $t_{-10}^{(-)}$, the probe pulse angle of incidence has to fullfill $\theta > \theta_C$. The dependence of θ_C on the probe wavelength λ is plotted in the inset of Fig. 10-4. For $\lambda = 800$ nm the cut-off angle is $\theta_C = 3^\circ$, which explains why there is no signal measured for $t - t_S < 0$ and $\theta = 2^\circ$, as seen in Fig. 10-3(c).

For $\theta = 7^\circ$, the transmission coefficients for both considered diffraction orders are non-negligible and Eq. 10.7 can be used to estimate the relative amplitudes of their contribution to the interferometry signal $\Delta I_{p-s}(t)$. Taking typical strain pulse parameters [16] and phonon attenuation in GGG [110], it is estimated that the *Fourier* components η_{ω_0} and $\eta_{\omega_{-1}}$ have a comparable magnitude. Furthermore, the ratio of the photoelastic constants is $p_{11}/p_{12} \approx 3$ [109], so that, finally, the amplitude of the spectral component at ω_{-1} is estimated to be 12 times larger than the one at ω_0.

This contrast may be even larger, if one considers the efficiency of the acousto optical coupling. For $\theta = 7^\circ$, the diffracted light component inside GGG is incident on the strain pulse under a large oblique angle of 76°. Therefore, the length of the path

---

[1] All RCWA calculations have been performed by V. I. Belotelev, Lomonosov Moscow State University, 119991 Moscow, Russia

through the area with coherent phonons is increased compared to the non-diffracted beam, which is almost normally incident. This may potentially lead to a stronger coupling efficiency.
For the above mentioned reasons, it is reasonable to assume that the spectrum of the interferometry signal $\Delta I_{p-s}(t)$ in Fig. 10-3(b) is dominated by the component of the diffracted beam at the frequency ω_{-1}.
It should be mentioned that the BIG layer, which is responsible for the WGM, expands the spectral region for which light transission into GGG and back into air has non-negligible values. This may be the main reason why the interferometry signal at $t - t_S < 0$ has not been observed for the sample without a wave guiding layer, presented in chapter 9.

The oscillations of $\Delta I_{p-s}(t)$ at $t - t_S < 0$ decay with increasing negative delay [Fig. 10-3(a)]. This decay can not stem from the absorption of light, because GGG is transparent for light with $\lambda = 800$ nm, but it is rather due to dephasing. The finite spectral width of the optical probe pulse results in slightly different oscillation frequencies for each spectral component. The time τ, after which these individual oscillations run out of phase can be estimated by [132]

$$\tau = c_0 t_{op} \left(\frac{d\omega_{-1}}{dk} \right)^{-1}, \tag{10.8}$$

where c_0 is the vacuum speed of light and t_{op} is the duration of the optical probe pulse. For $t_{op} = 150$ fs and the experimental parameters, Eq. 10.8 yields a dephasing time of $\tau = 455$ ps, which agrees well with the experimental observation.

10.3 Conclusion and perspective

In conclusion, *Brillouin* oscillations have been detected in the picosecond acoustic interferometry signal in a sample with a periodic gold grating on top. The frequency of the oscillation could be associated with light of the first negative diffraction order, interacting with GHz coherent phonons of a propagating strain pulse. In a theoretical analysis, the relative amplitudes of the contributions associated with diffracted and non-diffracted light in the spectrum of the interferometry signal have been compared, in agreement with experimental observations.

It has, therefore, been demonstrated that coherent phonons are a promising tool to probe the electromagnetic far-field inside samples with periodic structures on top. Standard optical techniques that are established to probe the far-field outside the sample, cannot easily be applied for in-sample probing. The interferometric signal can be analyzed in terms of the *Brillouin* frequencies, which are governed by the angle distribution of electromagnetic waves inside the medium and, thereby, reflect the interaction of light excitations in the periodic structure. The theoretical framework provides a tool for the design of structures, where the interaction of light with coherent phonons can be deliberately exploited.

The results obtained for the one dimensional planar structure investigated here show the potential of this method for acoustic nanoscopy [133]. In the future, it may be applied to more complex structures, such as two-dimensional photonic crystals.

Bibliography

[1] C. K. Kao and G. A. Hockham, *Proceedings IEE* **113**, 1151 (1966). 2

[2] N. N. Ledentsov, *Semicond. Sci. Tech.* **26**, 014001 (2011). 2

[3] H. Liu, C. Lam, and C. Johnson, Scaling Optical Interconnects in Datacenter Networks Opportunities and Challenges for WDM, in *High Performance Interconnects (HOTI), 2010 IEEE 18th Annual Symposium*, pp. 113–116, (2010). 2

[4] R. Rodes, J. Estaran, B. Li, M. Muller, J. Jensen, T. Gruendl, M. Ortsiefer, C. Neumeyr, J. Rosskopf, K. Larsen, M. C. Amann, and I. Monroy, 100 Gb/s single VCSEL data transmission link, in *Optical Fiber Communication Conference and Exposition (OFC/NFOEC), 2012 and the National Fiber Optic Engineers Conference*, pp. 1–3, (2012). 2

[5] R. Dingle and C. H. Henry, Quantum effects in heterostructure lasers, (1976), US Patent No 3982207. 2

[6] J. A. Conway, S. Sahni, and T. Szkopek, *Opt. Express* **15**, 4474 (2007). 2

[7] E. Ozbay, *Science* **311**, 189 (2006). 2

[8] J. Takahara, S. Yamagishi, H. Taki, A. Morimoto, and T. Kobayashi, *Opt. Lett.* **22**, 475 (1997). 2

[9] K. Nerkararyan, *Phys. Lett. A* **237**, 103 (1997). 2

[10] D. K. Gramotnev and S. I. Bozhevolnyi, *Nat. Photonics* **4**, 83 (2010), and references therein. 2, 60

[11] G. Czycholl, *Theoretische Festkörperphysik*, Springer, Berlin, (2007). 5, 6, 7, 8, 9, 33

[12] N. W. Ashcroft and N. D. Mermin, *Festkörperphysik*, Oldenbourg Wissenschaftsverlag, München, (2005). 5, 7, 61

[13] G. L. Bir and G. E. Pikus, *Soviet Phys. - Solid State* **2**, 2039 (1961). 5, 33, 34

[14] L. Landau and E. Lifschitz, *Theory of elasticity*, Pergamon Press, Oxford, 2nd edition, (1970). 8, 9

[15] M. Sadd, *Elasticity: Theory, Applications, and Numerics*, Elsevier Science, Oxford, (2010). 9

[16] C. Thomsen, H. T. Grahn, H. J. Maris, and J. Tauc, *Phys. Rev. B* **34**, 4129 (1986). 9, 10, 11, 24, 71, 78, 79, 83

[17] O. B. Wright, *Phys. Rev. B* **49**, 9985 (1994). 11

[18] G. Tas and H. J. Maris, *Phys. Rev. B* **49**, 15046 (1994). 11

[19] T. Saito, O. Matsuda, and O. B. Wright, *Phys. Rev. B* **67**, 205421 (2003). 11

[20] A. V. Akimov, A. V. Scherbakov, P. J. S. van Capel, J. I. Dijkhuis, T. Berstermann, D. R. Yakovlev, and M. Bayer, *J. Phys. Conf. Ser.* **92**, 012002 (2007). 11, 12

[21] H.-Y. Hao and H. J. Maris, *Phys. Rev. B* **64**, 064302 (2001). 11, 12, 13, 41

[22] D. J. Korteweg and G. de Vries, *Philos. Mag.* **39**, 422 (1895). 13

[23] N. J. Zabusky and M. D. Kruskal, *Phys. Rev. Lett.* **15**, 240 (1965). 13

[24] O. L. Muskens, A. V. Akimov, and J. I. Dijkhuis, *Phys. Rev. Lett.* **92**, 035503 (2004). 13

[25] O. L. Muskens and J. I. Dijkhuis, *Phys. Rev. B* **71**, 104304 (2005). 13

[26] A. V. Akimov, A. V. Scherbakov, D. R. Yakovlev, C. T. Foxon, and M. Bayer, *Phys. Rev. Lett.* **97**, 037401 (2006). 13, 34, 39

[27] A. V. Scherbakov, P. J. S. van Capel, A. V. Akimov, J. I. Dijkhuis, D. R. Yakovlev, T. Berstermann, and M. Bayer, *Phys. Rev. Lett.* **99** (2007). 13, 24, 34, 39, 40

[28] T. Berstermann, A. V. Scherbakov, A. V. Akimov, D. R. Yakovlev, N. A. Gippius, B. A. Glavin, I. Sagnes, J. Bloch, and M. Bayer, *Phys. Rev. B* **80**, 075301 (2009). 13, 34, 39

[29] K. J. Vahala, *Nature* **424**, 839 (2003). 24, 36

[30] J. M. Gerard, B. Sermage, B. Gayral, B. Legrand, E. Costard, and V. Thierry-Mieg, *Phys. Rev. Lett.* **81**, 1110 (1998). 24

[31] C. Weisbuch, M. Nishioka, A. Ishikawa, and Y. Arakawa, *Phys. Rev. Lett.* **69**, 3314 (1992). 24

[32] J. P. Reithmaier, G. Sek, A. Loffler, C. Hofmann, S. Kuhn, S. Reitzenstein, L. V. Keldysh, V. D. Kulakovskii, T. L. Reinecke, and A. Forchel, *Nature* **432**, 197 (2004). 24

[33] T. Yoshie, A. Scherer, J. Hendrickson, G. Khitrova, H. M. Gibbs, G. Rupper, C. Ell, O. B. Shchekin, and D. G. Deppe, *Nature* **432**, 200 (2004). 24

[34] P. Michler, A. Kiraz, C. Becher, W. V. Schoenfeld, P. M. Petroff, L. D. Zhang, E. Hu, and A. Imamoglu, *Science* **290**, 2282 (2000). 24

[35] R. J. Young, R. M. Stevenson, P. Atkinson, K. Cooper, D. A. Ritchie, and A. J. Shields, *New J. Phys.* **8** (2006). 24

[36] N. Akopian, N. H. Lindner, E. Poem, Y. Berlatzky, J. Avron, D. Gershoni, B. D. Gerardot, and P. M. Petroff, *Phys. Rev. Lett.* **96** (2006). 24

[37] A. Dousse, J. Suffczynski, A. Beveratos, O. Krebs, A. Lemaitre, I. Sagnes, J. Bloch, P. Voisin, and P. Senellart, *Nature* **466**, 217 (2010). 24

[38] J. Kasprzak, M. Richard, S. Kundermann, A. Baas, P. Jeambrun, J. M. J. Keeling, F. M. Marchetti, M. H. Szymanska, R. Andre, J. L. Staehli, V. Savona, P. B. Littlewood, B. Deveaud, and L. S. Dang, *Nature* **443**, 409 (2006). 24

[39] H. Deng, G. Weihs, C. Santori, J. Bloch, and Y. Yamamoto, *Science* **298**, 199 (2002). 24

[40] R. Balili, V. Hartwell, D. Snoke, L. Pfeiffer, and K. West, *Science* **316**, 1007 (2007). 24

[41] A. Amo, D. Sanvitto, F. P. Laussy, D. Ballarini, E. del Valle, M. D. Martin, A. Lemaitre, J. Bloch, D. N. Krizhanovskii, M. S. Skolnick, C. Tejedor, and L. Vina, *Nature* **457**, 291 (2009). 24

[42] C. Kistner, T. Heindel, C. Schneider, A. Rahimi-Iman, S. Reitzenstein, S. Hoefling, and A. Forchel, *Opt. Express* **16**, 15006 (2008). 24

[43] S. Reitzenstein, S. Muench, P. Franeck, A. Rahimi-Iman, A. Loeffler, S. Hoefling, L. Worschech, and A. Forchel, *Phys. Rev. Lett.* **103** (2009). 24

[44] P. Milonni and J. Eberly, *Laser Physics*, John Wiley & Sons, New Jersey, (2010). 25, 37

[45] H. Yokoyama and S. D. Brorson, *J. Appl. Phys.* **66**, 4801 (1989). 29, 37

[46] P. R. Rice and H. J. Carmichael, *Phys. Rev. A* **50**, 4318 (1994). 29, 37

[47] C. Klingshirn, *Semiconductor Optics*, Springer, Berlin, (2005). 30

[48] C. Weisbuch and B. Vinter, *Quantum Semiconductor Structures: Fundamentals and Applications*, Academic Press, London, (1991). 30

[49] L. Bányai and S. Koch, *Semiconductor Quatum Dots*, World Scientific, Singapore, (1993). 30, 37

[50] D. Bimberg, N. Kirstaedter, N. Ledentsov, Z. Alferov, P. Kop'ev, and V. Ustinov, *IEEE J. Sel. Top. Qant.* **3**, 196 (1997). 30

[51] A. Kavokin, J. Baumberg, G. Malpuech, and F. Laussy, *Microcavities*, Oxford University Press, Oxford, (2007). 31, 32, 35

[52] M. Born and E. Wolf, *Principles of Optics: Electromagnetic Theory of Propagation, Interference and Diffraction of Light*, Cambridge University Press, Cambridge, 7th edition, (1999). 32, 53, 72

[53] J. M. Luttinger and W. Kohn, *Phys. Rev.* **97**, 869 (1955). 34

[54] F. H. Pollak and M. Cardona, *Phys. Rev.* **172**, 816 (1968). 34

[55] P. Yu, *Fundamentals of Semiconductors*, Springer, Berlin, (2010). 34

[56] A. V. Scherbakov, T. Berstermann, A. V. Akimov, D. R. Yakovlev, G. Beaudoin, D. Bajoni, I. Sagnes, J. Bloch, and M. Bayer, *Phys. Rev. B* **78**, 241302 (2008). 34, 39

[57] A. Pawlis, T. Berstermann, C. Brüggemann, M. Bombeck, D. Dunker, D. R. Yakovlev, N. A. Gippius, K. Lischka, and M. Bayer, *Phys. Rev. B* **83**, 115302 (2011). 34, 39

[58] T. Berstermann, C. Brüggemann, A. V. Akimov, M. Bombeck, D. R. Yakovlev, N. A. Gippius, A. V. Scherbakov, I. Sagnes, J. Bloch, and M. Bayer, *Phys. Rev. B* **86**, 195306 (2012). 34, 39

[59] I. N. Stranski and L. Von Krastanov, *Akad. Wiss. Lett. Mainz Math. Natur. K1 IIb* **146**, 797 (1939). 35

[60] V. Savona, L. Andreani, P. Schwendimann, and A. Quattropani, *Solid State Commun.* **93**, 733 (1995). 35

[61] M. Kaniber, A. Laucht, T. Huerlimann, M. Bichler, R. Meyer, M.-C. Amann, and J. J. Finley, *Phys. Rev. B* **77** (2008). 36

[62] S. Ates, S. M. Ulrich, A. Ulhaq, S. Reitzenstein, A. Loeffler, S. Hoefling, A. Forchel, and P. Michler, *Nat. Photonics* **3**, 724 (2009). 36

[63] D. Press, S. Goetzinger, S. Reitzenstein, C. Hofmann, A. Loeffler, M. Kamp, A. Forchel, and Y. Yamamoto, *Phys. Rev. Lett.* **98** (2007). 36

[64] K. Hennessy, A. Badolato, M. Winger, D. Gerace, M. Atatuere, S. Gulde, S. Faelt, E. L. Hu, and A. Imamoglu, *Nature* **445**, 896 (2007). 36

[65] M. Winger, T. Volz, G. Tarel, S. Portolan, A. Badolato, K. J. Hennessy, E. L. Hu, A. Beveratos, J. Finley, V. Savona, and A. Imamoglu, *Phys. Rev. Lett.* **103**, 207403 (2009). 36

[66] E. M. Purcell, *Phys. Rev.* **69**, 674 (1946). 36

[67] Y. Ota, S. Iwamoto, N. Kumagai, and Y. Arakawa, *Phys. Rev. Lett.* **107**, 233602 (2011). 38

[68] T. Berstermann, C. Brüggemann, M. Bombeck, A. V. Akimov, D. R. Yakovlev, C. Kruse, D. Hommel, and M. Bayer, *Phys. Rev. B* **81**, 085316 (2010). 44

[69] R. P. Beardsley, A. V. Akimov, M. Henini, and A. J. Kent, *Phys. Rev. Lett.* **104**, 085501 (2010). 49

[70] B. Maune, J. Witzens, T. B. Jones, M. Kolodrubetz, H. Atwater, A. Scherer, R. Hagen, and Y. M. Qiu, *Opt. Express* **13**, 4699 (2005). 49

[71] T. Tanabe, E. Kuramochi, H. Taniyama, and M. Notomi, *Opt. Lett.* **35**, 3895 (2010). 49

[72] A. Huynh, B. Perrin, N. D. Lanzillotti-Kimura, B. Jusserand, A. Fainstein, and A. Lemaître, *Phys. Rev. B* **78**, 233302 (2008). 49, 75

[73] N. D. Lanzillotti-Kimura, A. Fainstein, C. A. Balseiro, and B. Jusserand, *Phys. Rev. B* **75**, 024301 (2007). 49, 53, 57

[74] N. D. Lanzillotti-Kimura, A. Fainstein, A. Lemaitre, B. Jusserand, and B. Perrin, *Phys. Rev. B* **84**, 115453 (2011). 49, 57

[75] S. Adachi, *J. Appl. Phys.* **58**, R1 (1985). 51

[76] S. Tamura, D. C. Hurley, and J. P. Wolfe, *Phys. Rev. B* **38**, 1427 (1988). 51, 53

[77] J. D. Jackson, *Classical electrodynamics*, Wiley, New York, (1975). 54, 62

[78] L. Brillouin, *Wave propagation and group velocity*, Academic Press, New York, (1960). 54

[79] J. H. Page, P. Sheng, H. P. Schriemer, I. Jones, X. Jing, and D. A. Weitz, *Science* **271**, 634 (1996). 54

[80] A. Huynh, N. D. Lanzillotti-Kimura, B. Jusserand, B. Perrin, A. Fainstein, M. F. Pascual-Winter, E. Peronne, and A. Lemaître, *Phys. Rev. Lett.* **97**, 115502 (2006). 54, 57, 75

[81] M. Trigo, A. Bruchhausen, A. Fainstein, B. Jusserand, and V. Thierry-Mieg, *Phys. Rev. Lett.* **89**, 227402 (2002). 57

[82] A. L. Lereu, A. Passian, J.-P. Goudonnet, T. Thundat, and T. L. Ferrell, *Appl. Phys. Lett.* **86**, 154101 (2005). 60

[83] J. N. Caspers, N. Rotenberg, and H. M. van Driel, *Opt. Express* **18**, 19761 (2010). 60

[84] H. Baida, P. Billaud, S. Marhaba, D. Christofilos, E. Cottancin, A. Crut, J. Lermé, P. Maioli, M. Pellarin, M. Broyer, N. Del Fatti, F. Valleé, A. Sánchez-Iglesias, I. Pastoriza-Santos, and L. M. Liz-Marzán, *Nano Lett.* **9**, 3463 (2009). 60

[85] J. Dintinger, I. Robel, P. V. Kamat, C. Genet, and T. W. Ebbesen, *Adv. Mater.* **18**, 1645 (2006). 60

[86] L. L. Guyader, A. Kirilyuk, T. Rasing, G. A. Wurtz, A. V. Zayats, P. F. A. Alkemade, and I. I. Smolyaninov, *J. Phys. D: Appl. Phys.* **41**, 195102 (2008). 60, 77, 80

[87] N. M. Hassan, V. V. Mkhitaryan, and E. G. Mishchenko, *Phys. Rev. B* **85**, 125411 (2012). 60

[88] V. V. Temnov, G. Armelles, U. Woggon, D. Guzatov, A. Cebollada, A. Garcia-Martin, J. M. Garcia-Martin, T. Thomay, A. Leitenstorfer, and R. Bratschitsch, *Nat. Photonics* **4**, 107 (2010). 60

[89] V. I. Belotelov, I. A. Akimov, M. Pohl, V. A. Kotov, S. Kasture, A. S. Vengurlekar, A. V. Gopal, D. R. Yakovlev, A. K. Zvezdin, and M. Bayer, *Nat. Nanotechnol.* **6**, 370 (2011). 60, 80

[90] N. Rotenberg, J. N. Caspers, and H. M. van Driel, *Phys. Rev. B* **80**, 245420 (2009). 60

[91] M. Pohl, V. I. Belotelov, I. A. Akimov, S. Kasture, A. S. Vengurlekar, A. V. Gopal, A. K. Zvezdin, D. R. Yakovlev, and M. Bayer, *Phys. Rev. B* **85**, 081401 (2012). 60, 80

[92] Y.-L. Chiang, C.-W. Chen, C.-H. Wang, C.-Y. Hsieh, Y.-T. Chen, H.-Y. Shih, and Y.-F. Chen, *Appl. Phys. Lett.* **96**, 041904 (2010). 60

[93] D. Christofilos, S. Assimopoulos, N. Del Fatti, C. Voisin, F. Vallée, G. A. Kourouklis, and S. Ves, *High Pressure Res.* **23**, 23 (2003). 60

[94] N. Del Fatti, C. Voisin, F. Chevy, F. Vallée, and C. Flytzanis, *J. Chem. Phys.* **110**, 11484 (1999). 60

[95] J. H. Hodak, A. Henglein, and G. V. Hartland, *J. Chem. Phys.* **111**, 8613 (1999). 60

[96] J. S. Im and G. P. Wiederrecht, Low-damping picosecond coherent vibration of lithographically fabricated silver nanostructures, in *Conference on Lasers and Electro-Optics/International Quantum Electronics Conference and Photonic Applications Systems Technologies*, p. ITuB1, (2004). 60

[97] C. Ruppert, J. Neumann, J. B. Kinzel, H. J. Krenner, A. Wixforth, and M. Betz, *Phys. Rev. B* **82**, 081416 (2010). 60, 70

[98] H.-P. Chen, Y.-C. Wen, Y.-H. Chen, C.-H. Tsai, K.-L. Lee, P.-K. Wei, J.-K. Sheu, and C.-K. Sun, *Appl. Phys. Lett.* **97**, 201102 (2010). 60, 71, 74, 77

[99] S. Maier, *Plasmonics: Fundamentals and Applications*, Springer, New York, (2007). 61, 62, 63

[100] H. Raether, *Surface plasmons on smooth and rough surfaces and on gratings*, Springer, Berlin, (1988). 62, 63, 65

[101] W. L. Barnes, A. Dereux, and T. W. Ebbesen, *Nature* **424**, 824 (2003). 63, 65

[102] A. Otto, *Z. Phys.* **216**, 398 (1968). 64

[103] E. Kretschmann and H. Raether, *Z. Naturforsch. A* (1968). 64

[104] R. H. Ritchie, E. T. Arakawa, J. J. Cowan, and R. N. Hamm, *Phys. Rev. Lett.* **21**, 1530 (1968). 64

[105] W. L. Barnes, T. W. Preist, S. C. Kitson, and J. R. Sambles, *Phys. Rev. B* **54**, 6227 (1996). 65

[106] I. R. Hooper and J. R. Sambles, *Phys. Rev. B* **66**, 205408 (2002). 65

[107] M. G. Moharam, D. A. Pommet, E. B. Grann, and T. K. Gaylord, *J. Opt. Soc. Am. A* **12**, 1077 (1995). 65, 73, 83

[108] L. Li, *J. Opt. A: Pure Appl. Opt.* **5**, 345 (2003). 65, 73, 83

[109] V. F. Kitaeva, E. V. Zharikov, and I. L. Chistyi, *Phys. Stat. Sol. A* **92**, 475 (1985). 68, 81, 83

[110] M. Krzesińska and T. Szuta Buchacz, *Phys. Stat. Sol. A* **82**, 421 (1984). 70, 75, 83

[111] L. Le Guyader, A. Kirilyuk, T. Rasing, G. A. Wurtz, A. V. Zayats, P. F. A. Alkemade, and I. I. Smolyaninov, *J. Phys. D: Appl. Phys.* **41**, 195102 (2008). 70

[112] G. A. Antonelli, H. J. Maris, S. G. Malhotra, and J. M. E. Harper, *J. Appl. Phys.* **91**, 3261 (2002). 71, 74, 77, 80

[113] S.-C. Yang, H.-P. Chen, H.-H. Hsiao, P.-K. Wei, H.-C. Chang, and C.-K. Sun, *Opt. Express* **20**, 16186 (2012). 71, 74, 77, 80

[114] R. F. Humphryes and E. A. Ash, *Electron. Lett.* **5**, 175 (1969). 72

[115] M. Yamanishi, M. Ameda, T. Kawamura, N. Mikoshiba, and K. Tsubouchi, *Electron. Lett.* **12**, 317 (1976). 72

[116] N. E. Glass, R. Loudon, and A. A. Maradudin, *Phys. Rev. B* **24**, 6843 (1981). 73

[117] A. V. Akimov, Y. Tanaka, A. B. Pevtsov, S. F. Kaplan, V. G. Golubev, S. Tamura, D. R. Yakovlev, and M. Bayer, *Phys. Rev. Lett.* **101**, 033902 (2008). 77

[118] A. S. Salasyuk, A. V. Scherbakov, D. R. Yakovlev, A. V. Akimov, A. A. Kaplyanskii, S. F. Kaplan, S. A. Grudinkin, A. V. Nashchekin, A. B. Pevtsov, V. G. Golubev, T. Berstermann, C. Brüggemann, M. Bombeck, and M. Bayer, *Nano Lett.* **10**, 1319 (2010). 77

[119] C. Brüggemann, A. V. Akimov, B. A. Glavin, V. I. Belotelov, I. A. Akimov, J. Jäger, S. Kasture, A. V. Gopal, A. S. Vengurlekar, D. R. Yakovlev, A. J. Kent, and M. Bayer, *Phys. Rev. B* **86**, 121401 (2012). 77, 80

[120] P.-A. Mante, H.-Y. Chen, M.-H. Lin, Y.-C. Wen, S. Gwo, and C.-K. Sun, *Appl. Phys. Lett.* **101**, 101903 (2012). 77

[121] J. R. Sandercock, *Phys. Rev. Lett.* **28**, 237 (1972). 78

[122] H. N. Lin, R. J. Stoner, H. J. Maris, and J. Tauc, *J. Appl. Phys.* **69**, 3816 (1991). 78

[123] O. B. Wright, *J. Appl. Phys.* **71**, 1617 (1992). 78

[124] R. Cote and A. Devos, *Rev. Sci. Instrum.* **76**, 053906 (2005). 78

[125] O. B. Wright, B. Perrin, O. Matsuda, and V. E. Gusev, *Phys. Rev. B* **64**, 081202 (2001). 78

[126] P. Babilotte, P. Ruello, D. Mounier, T. Pezeril, G. Vaudel, M. Edely, J.-M. Breteau, V. Gusev, and K. Blary, *Phys. Rev. B* **81**, 245207 (2010). 78

[127] F. Yang, T. J. Grimsley, S. Che, G. A. Antonelli, H. J. Maris, and A. V. Nurmikko, *J. Appl. Phys.* **107**, 103537 (2010). 78

[128] E. Pontecorvo, M. Ortolani, D. Polli, M. Ferretti, G. Ruocco, G. Cerullo, and T. Scopigno, *Appl. Phys. Lett.* **98**, 011901 (2011). 78

[129] R. Liu, G. D. Sanders, C. J. Stanton, C. S. Kim, J. S. Yahng, Y. D. Jho, K. J. Yee, E. Oh, and D. S. Kim, *Phys. Rev. B* **72**, 195335 (2005). 78

[130] D. Palik, *Handbook of optical constants of solids*, Edward Academic Press, (1985). 81

[131] C. Brüggemann, J. Jäger, B. A. Glavin, V. I. Belotelov, I. A. Akimov, S. Kasture, A. V. Gopal, A. S. Vengurlekar, D. R. Yakovlev, A. V. Akimov, and M. Bayer, *Appl. Phys. Lett.* **101**, 243117 (2012). 82

[132] C. Thomsen, H. Grahn, H. Maris, and J. Tauc, *Opt. Commun.* **60**, 55 (1986). 84

[133] K.-H. Lin, C.-M. Lai, C.-C. Pan, J.-I. Chyi, J.-W. Shi, S.-Z. Sun, C.-F. Chang, and C.-K. Sun, *Nat. Nanotechnol.* **2**, 201102 (2007). 85

List of acronyms

BBO	beta barium borate
BIG	bismuth substituded rare-earth iron garnet
BR	balanced photoreceiver
BS	beam splitter
BF	blue filter
CCD	charge-coupled device
CW	continuous wave
DBR	distributed bragg reflector
FFT	fast Fourier transform
GF	gradient greyfilter
GGG	gadolinium gallium garnet
GTP	Glan-Thompson prism
LA	longitudinal acoustic
LO	longitudinal optic
LP	long pass
MBZ	mini Brillouin zone
MC	microcavity
MO	microscope objective
QD	quantum dot
RCWA	rigorous coupled wave analysis
S	sample
SC	semiconductor
SSP	surface plasmon polariton
SL	superlattice
TA	transverse acoustic
VCSEL	vertical cavity surface emitting laser
VTI	variable temperature insert
WGM	waveguiding mode
$\lambda/2$	waveplate

Publications

"Studying periodic nanostructures by probing the in-sample optical far-field using coherent phonons",
C. Brüggemann, J. Jäger, B. A. Glavin, V. I. Belotelov, I. A. Akimov, S. Kasture, A. V. Gopal, A. S. Vengurlekar, D. R. Yakovlev, A. V. Akimov, and M. Bayer *Appl. Phys. Lett.* **101**, 243117 (2012)

"Modulation of a surface plasmon-polariton resonance by subterahertz diffracted coherent phonons",
C. Brüggemann, A. V. Akimov, B. A. Glavin, V. I. Belotelov, I. A. Akimov, J. Jäger, S. Kasture, A. V. Gopal, A. S. Vengurlekar, D. R. Yakovlev, A. J. Kent, and M. Bayer, *Phys. Rev. B* **86**, 121401(R) (2012)

"Destruction and recurrence of excitons by acoustic shock waves on picosecond time scales",
T. Berstermann, **C. Brüggemann**, A. V. Akimov, M. Bombeck, D. R. Yakovlev, N. A. Gippius, A. V. Scherbakov, I. Sagnes, J. Bloch, and M. Bayer, *Phys. Rev. B* **86**, 195306 (2012)

"Hybrid structures of magnetic semiconductors and plasmonic crystals: a novel concept for magneto-optical devices",
I. A. Akimov, V. I. Belotelov, A. V. Scherbakov, M. Pohl, A. N. Kalish, A. S. Salasyuk, M. Bombeck, **C. Brüggemann**, A. V. Akimov, R. I. Dzhioev, V. L. Korenev, Y. G. Kusrayev, V. F. Sapega, V. A. Kotov, D. R. Yakovlev, A. K. Zvezdin, and M. Bayer, *J. Opt. Soc. Am. B* **29**, A103 (2012)

"Laser mode feeding by shaking quantum dots in a planar microcavity",
C. Brüggemann, A. V. Akimov, A. V. Scherbakov, M. Bombeck, C. Schneider, S. Höfling, A. Forchel, D. R. Yakovlev, and M. Bayer, *Nat. Photonics* **6**, 30 (2011)

"Exciton states in shallow ZnSe/(Zn,Mg)Se quantum wells: Interaction of confined and continuum electron and hole states",
A. Pawlis, T. Berstermann, **C. Brüggemann**, M. Bombeck, D. Dunker, D. R. Yakovlev, N. A. Gippius, K. Lischka, and M. Bayer, *Phys. Rev. B* **83**, 115302 (2011)

"Coherent Magnetization Precession in Ferromagnetic (Ga,Mn)As Induced by Picosecond Acoustic Pulses",
A. V. Scherbakov, A. S. Salasyuk, A. V. Akimov, X. Liu, M. Bombeck, **C. Brüggemann**, D. R. Yakovlev, V. F. Sapega, J. K. Furdyna, and M. Bayer, *Phys. Rev. Lett.* **105**, 117204 (2010)

"Filtering of Elastic Waves by Opal-Based Hypersonic Crystal",
A. S. Salasyuk, A. V. Scherbakov, D. R. Yakovlev, A. V. Akimov, A. A. Kaplyanskii, S. F. Kaplan, S. A. Grudinkin, A. V. Nashchekin, A. B. Pevtsov, V. G. Golubev, T. Berstermann, **C. Brüggemann**, M. Bombeck, and M. Bayer, *Nano Lett.* **10**, 1319 (2010)

"Optical bandpass switching by modulating a microcavity using ultrafast acoustics",
T. Berstermann, **C. Brüggemann**, M. Bombeck, A. V. Akimov, D. R. Yakovlev, C. Kruse, D. Hommel, and M. Bayer, *Phys. Rev. B* **81**, 085316 (2010)

Acknowledgements

There are many people without whom this work would never have been possible. Hereby, i want to thank all of them for their great support!

I especially want to thank Prof. Dr. Manfred Bayer and Prof. Dr. Andrey V. Akimov for the opportunity to perform these studies, their outstanding guidance and help. Klaus Wiegers, Michaela Wäscher and Lars Wischolek provided excellent administrative and technical assistance. I have to thank Dr. Alexey V. Scherbakov, Dr. Alexey S. Salasyuk, Michael Bombeck and Tillmann Godde for incomparable times in and outside the lab and for fruitful discussions about numerous topics during the last 4 years. Michael Bombeck receives a special mentioning for his awesome catering service. Not to forget the newer members of our picosecond acoustics group, Jasmin Jäger and Thomas Czerniuk, who have both added a lot to the quality time in the office.

I want to thank Jasmin Jäger, Thomas Czerniuk, Martin Pohl, Matthias Bachmann, Dr. Jean-Sebastian Tempel and Dr. Jörg Debus, who kindly devoted their time to proofread some chapters of this thesis.

A big thank you to all members of the chair Experimentelle Physik 2. The atmosphere has been phenomenal, making everyday work a lot easier.

Last but not least, i have to thank my supportive family and especially my mother Gaby, my father Walter, my brother Michael, Hans and Maria. I want to convey my deepest gratefulness! They have been the foundation of this work.